VALIDATION OF
MAGNETOSPHERIC MAGNETOHYDRODYNAMIC MODELS

by

Brian Curtis
A Dissertation
Submitted to the
Graduate Faculty
of
George Mason University
In Partial Fulfillment of
The Requirements for the Degree
of
Doctor of Philosophy
Computational Science and Informatics

Committee:

______________________ Dr. Robert Weigel, Dissertation Director

______________________ Dr. Jie Zhang, Committee Member

______________________ Dr. Arthur Poland, Committee Member

______________________ Dr. Ruixin Yang, Committee Member

______________________ Dr. Chi Yang, Director, School of Physics, Astronomy and Computational Sciences

______________________ Dr. Donna M. Fox, Associate Dean, Office of Student Affairs & Special Programs, College of Science

______________________ Dr. Peggy Agouris, Dean, College of Science

Date: ____________________ Spring Semester 2014
George Mason University
Fairfax, VA

Validation of Magnetospheric Magnetohydrodynamic Models

A dissertation submitted in partial fulfillment of the requirements for the degree of Doctor of Philosophy at George Mason University

By

Brian Curtis
Master of Science
George Mason University, 2010
Bachelor of Science
State University of New York at Oswego, 2007

Director: Dr. Robert Weigel
School of Physics, Astronomy, and Computational Sciences

Spring Semester 2014
George Mason University
Fairfax, VA

Dedication

I dedicate this dissertation to my friends and family who have helped push me along this journey and made it worthwhile. Specifically my wife, Tamarah, who has dealt with my hectic work life and loved and supported me so much, making sure that home was truly a comforting and restoring place for my mind and body. Also, my parents Robert and Deborah Curtis and brother Jeff Curtis, who have supported me throughout all my years in education and shown me the importance every little detail makes in the big picture. Finally, my expected daughter, Aurora, who gives me inspiration to become as great of a human being as I can, to guarantee she has the best role model anyone could ask for.

Acknowledgments

I would like to thank my dissertation committee: Dr. Robert Weigel, Dr. Art Poland, Dr. Jie Zhang, and Dr. Ruixin Yang for agreeing to give me their time and effort. Special thanks to Dr. Robert Weigel who has made this whole graduate experience possible, whose guidance and insight has prepared me well for scientific pursuit and what to expect after graduation.

Table of Contents

List of Tables

List of Figures

Abstract

VALIDATION OF MAGNETOSPHERIC MAGNETOHYDRODYNAMIC MODELS
Brian Curtis, PhD
George Mason University, 2014
Dissertation Director: Dr. Robert Weigel

Magnetospheric magnetohydrodynamic (MHD) models are commonly used for both prediction and modeling of Earth's magnetosphere. To date, very little validation has been performed to determine their limits, uncertainties, and differences. In this work, we performed a comprehensive analysis using several commonly used validation techniques in the atmospheric sciences to MHD-based models of Earth's magnetosphere for the first time. The validation techniques of parameter variability/sensitivity analysis and comparison to other models were used on the OpenGGCM, BATS-R-US, and SWMF magnetospheric MHD models to answer several questions about how these models compare. The questions include: (1) the difference between the model's predictions prior to and following to a reversal of B_z in the upstream interplanetary field (IMF) from positive to negative, (2) the influence of the preconditioning duration, and (3) the differences between models under extreme solar wind conditions. A differencing visualization tool was developed and used to address these three questions.

We find: (1) For a reversal in B_z^{IMF} from positive to negative, the OpenGGCM magnetopause is closest to Earth as it has the weakest magnetic pressure near-Earth. The differences in magnetopause positions between BATS-R-US and SWMF are explained by the influence of the ring current, which is included in SWMF. Densities are highest for SWMF and lowest for OpenGGCM. The OpenGGCM tail currents differ significantly from BATS-R-US and SWMF; (2) A longer preconditioning time allowed the magnetosphere to relax more, giving different positions for the magnetopause with all three models before the B_z^{IMF} reversal. There were differences greater than 100% for all three models before the B_z^{IMF} reversal. The differences in the current sheet region for the OpenGGCM were small after the B_z^{IMF} reversal. The BATS-R-US and SWMF differences decreased after the B_z^{IMF} reversal to near zero; (3) For extreme conditions in the solar wind, the OpenGGCM has a large region of Earthward flow velocity (U_x) in the current sheet region that grows as time progresses in a compressed environment. BATS-R-US B_z, ρ and U_x stabilize to a near constant value approximately one hour into the run under high compression conditions. Under high compression, the SWMF parameters begin to oscillate approximately 100 minutes into the run. All three models have similar magnetopause positions under low pressure conditions. The OpenGGCM current sheet velocities along the Sun-Earth line are largest under low pressure conditions.

The results of this analysis indicate the need for accounting for model uncertainties and differences when comparing model predictions with data, provide error bars on model prediction in various magnetospheric regions, and show that the magnetotail is sensitive to the preconditioning time.

Chapter 1: Introduction

1.1 Space Weather

1.1.1 Definition and Impacts

Space weather is a term used to describe the state of the space environment and involves the influence of plasma traveling outward from the Sun and its interaction with the heliosphere, magnetosphere, ionosphere and thermosphere (*Thompson*, 2000). The five regions that are of primary interest of current research include the Sun, heliosphere, magnetosphere, ionosphere and thermosphere. In recent years, there has been interest in space weather impacts on the outer planets as more spacecraft missions explore these regions. At the same time, space technology is improving, and near-Earth space travel is becoming a greater possibility. Terrestrial objects are impacted by space weather radiation. Energetic particles can be absorbed in the metal shell of a satellite and disrupt the function of electrical components. Terrestrial objects affected include satellites and the space station. Earth's surface can also be impacted by space weather; during strong geomagnetic storms, induced ground currents can cause electrical grids to overload and large pipeline systems may degrade faster.

1.1.2 Space Weather Regions

Figure 1.1 shows a sketch of four space weather regions. The starting point of all space weather is the Sun. The region that extends from the solar surface to approximately 80-100 AU is called the heliosphere (the middle region in Figure 1.1 shows out to 1 AU) (*Mewaldt and Liewer*, 1995). Inside the heliosphere are the planets, most of which have internally generated magnetic fields that create a magnetic region known as a magnetosphere. Earth's magnetosphere is shown on the right in Figure 1.1, its outer boundary is defined at the

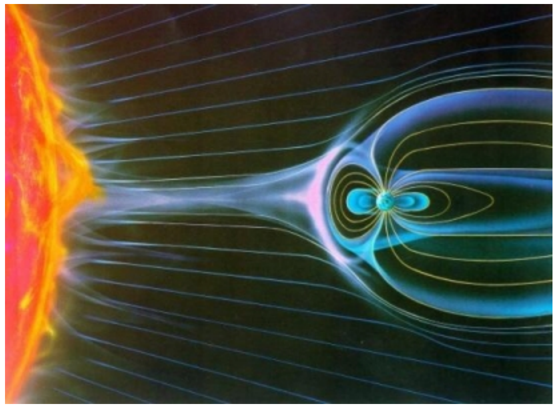

Figure 1.1: The Sun, heliosphere, and magnetosphere (from NASA, 2014a).

location where the magnetic pressure of Earth's magnetic field balances with the kinetic pressure of the plasma in the solar wind, and the inner boundary is defined as the region where the exterior of Earth's atmosphere interacts with the particles inside the magnetosphere, which is called the ionosphere.

1.1.3 Solar

The 11-year variation in the measured solar magnetic flux and number of sunspots defines the solar cycle (*Kallenrode*, 2004). All space weather originates at the Sun, which consists mostly of fully ionized hydrogen and has a very strong magnetic field. The plasma near the surface and the equator rotates faster than near the poles. The moving plasma in the Sun causes its strong magnetic field (*Kulsrud*, 2005).

The solar dynamo, responsible for creating the Sun's magnetic field, is due to the differential velocities of plasma near its surface (*Kulsrud*, 2005). Differential rotation causes the magnetic field to twist and stretch, which is defined as dynamo action. This twisting and stretching causes increasing tensions in the solar magnetic field. These associated poloidal and toroidal tensions cause regions of increased surface magnetic field that appear on the solar surface as sunspots.

The twisting and stretching of the magnetic field causes the Sun to have a very unique

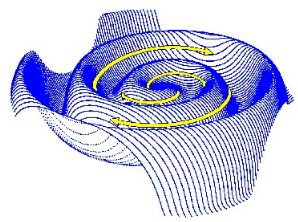

Figure 1.2: The Parker spiral (from NASA, 2014).

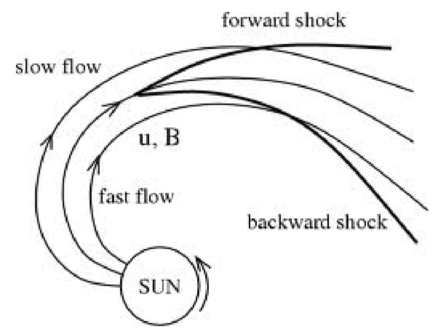

Figure 1.3: A co-rotating interaction region, (from *Volk and Zirakashvili*, 2004).

magnetic structure at times. Without a magnetic field, there would be a constant flow of plasma radially outward. The presence of a magnetic field causes changes in the location at which plasma escapes. There are different speeds of escaping plasma, and when viewed in a cut plane of radial flow velocities in the heliosphere, a spiral structure is expected as depicted in Figure 1.2. *Parker* (1958) first proposed the existence of this structure, now referred to as the Parker spiral. When different speeds of plasma flow outward from the Sun at different latitudes, there are regions where fast moving plasma impacts slower moving plasma (Figure 1.3) and results in a region of high density. These regions of high density plasma are called co-rotating Interaction Regions (CIRs).

The most concern in space weather forecasting comes from events that are associated with sunspots. Sunspots are regions of stronger magnetic field strength on the solar surface. These regions have unique magnetic field configurations that are believed to be related to the cause of solar flares and Coronal Mass Ejections (CME) (*Kallenrode*, 2004). Sunspots have a darker appearance as shown in Figure 1.4. These regions have a stronger magnetic

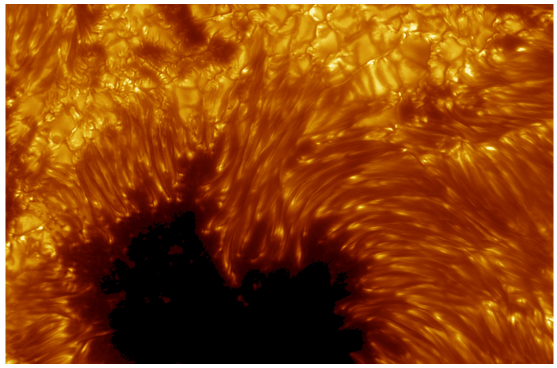

Figure 1.4: A Sunspot (from NASA, 2014b).

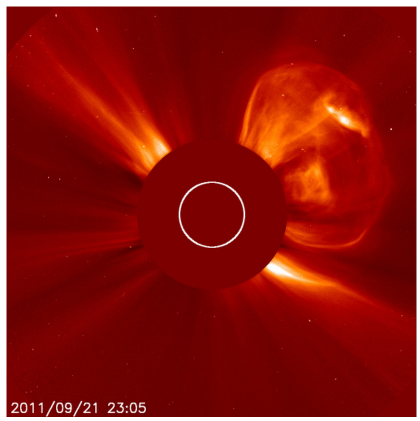

Figure 1.5: A coronal mass ejection (in the upper right corner of the image) taken from satellite imagery. The other two bright regions are called streamers (from NASA, 2014).

field strength, giving them the darker appearance.

Solar flares are rapid bursts of energy released from the Sun. They are typically observed as bright flashes in the visible H_α wavelengths. Solar flares emit high-velocity ionized particles that can be very close to the speed of light and are used as warning signs that a CME may have occurred and could eventually be measured by satellites near Earth (depending on their direction of propagation).

The name CME comes from satellite images showing large masses of plasma being ejected away from the solar corona into the heliosphere, as shown in Figure 1.5. The process that creates and drives CME s is complex; this process is the least understood space weather

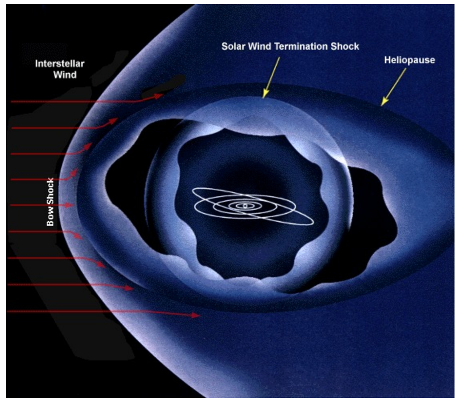

Figure 1.6: The heliosphere (from NASA, 2014).

related phenomena. The plasma associated with a CME has a shape similar to that of a light bulb and the magnetic fields they carry are typically unorganized, complex, and difficult to predict. Their cause is a subject of active research, but the generally accepted explanation is that they are initiated as a result of reconnection occurring near the sunspots (*Priest and Forbes*, 2000).

1.1.4 Heliosphere

The region exterior to the Sun and extending well beyond the orbit of Pluto is called the heliosphere. Its exact shape is unknown, but an approximate tear drop shape is depicted in Figure 1.6. The magnetic field it contains decreases in strength with distance. Although the exact location of the heliosphere boundary is unknown, it extends out well beyond the solar system, and spacecraft have measured what is believed to be a heliopause at approximately 120 AU (*Krimigis et al.*, 2009). The spacecraft measurements included a pause, sheath and shock region. These boundaries and region are explained in detail in section 2.1.

1.1.5 Ionosphere/Thermosphere

The ionosphere and thermosphere are contained within Earth's magnetosphere. The ionosphere and thermosphere are overlapping layers that are considered to be part of Earth's

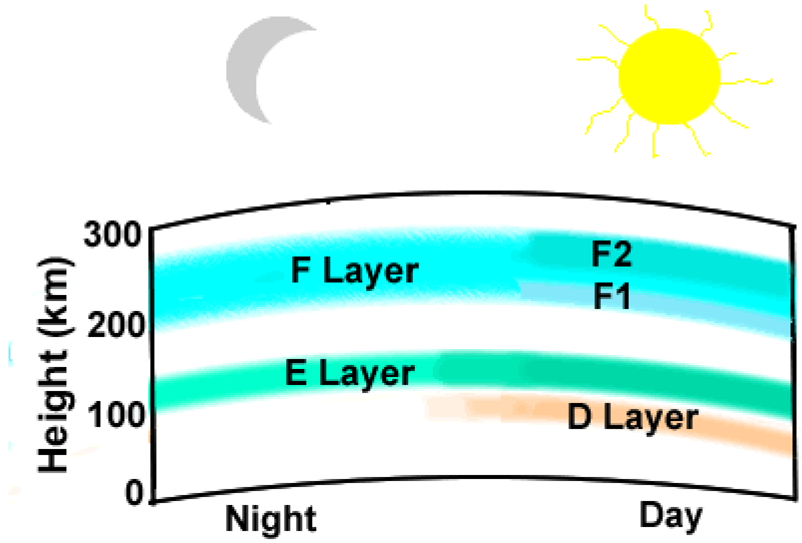

Figure 1.7: The layers of Earth's ionosphere during the night time and the day time (from Naval Postgraduate School, 2014).

upper atmosphere, as shown in Figure 1.7. The lower thermosphere boundary, which is located within the D and E regions of the ionosphere, is defined by a rapid change in temperature, which is caused by the absorption of ultraviolet (UV) and extreme UV (EUV) light. EUV radiation is responsible for the creation of plasma on the sunlit side of the layer. The ionosphere has two different profiles that are dependent on the time of day. The layers in each are labeled as D, E, and F. The layers are defined by the density of the plasma. The F region has the highest plasma density and is between 150-500 *km*. It is observed more frequently in the summer time, and can separate when radiation from the sun is highest. The E region is between 90-150 km and the D region is below 90 km (*Kelley*, 2009). One importance of the ionosphere is that high plasma densities can cause satellite drag. Satellite drag requires use of costly internal power resources, if available, to maintain altitude.

1.1.6 Importance of Space Weather Research

The Sun, heliosphere, magnetosphere, ionosphere, thermosphere, and all of their phenomena are interconnected. Understanding the thermosphere/ionosphere requires an understanding of the magnetosphere. Understanding the magnetosphere requires an understanding of the heliosphere. Understanding the heliosphere requires an understanding of the Sun. As we learn more about one region, better analysis can be made in all interconnected regions. The motivation for the pursuit of a better understanding of space weather is due to the potential implications that adverse conditions pose on terrestrial and space-based technology and operations. These implications include increases in ground currents which can damage electric power grids. HF and UHF communications can be disrupted, both of which are vital to the air travel industry and the military. Earth-orbiting satellites can be damaged from high energy particles. The global positioning system (GPS) is linked to these satellites, and satellite damage could cause a loss of GPS signals. Airplanes rely heavily on GPS. There are radiation exposure limits on astronauts as well as humans on polar flights (*Pirjola et al.*, 2005). The ability to predict these adverse effects can help maintain the safety of humans in space and ensure continual operation of space based technologies.

Terrestrial Weather

Meteorological observations in the United States have been recorded back as far as the 17th century and were most often made along the east coast (*Fiebrich*, 2009). Since then, significant improvements have been made. RADAR technology used in World War 2 (*Page*, 1962) was eventually used by the National Weather Service (NWS). Automated Surface Observing Systems (ASOS) have been placed throughout the country that record many meteorological conditions (*Ahrens*, 1994). Today, meteorological forecasts are made and disseminated by many sources including, but not limited to, radio stations, local television stations, the private sector, and the government. These forecasts are made using the guidance of forecast models. Meteorologists use the guidance of models to help make their forecasts as accurate and precise as possible. The ability to understand all meteorological models today would require a specific understanding of each model. The abundance of forecasting models in the meteorology community would make understanding each model a difficult task. With the increasing number of space weather models, this gives motivation for improved methods for understanding forecasting models.

Space Weather

The ability to measure space weather became possible with satellite technology. The first satellites were launched in the late 1950s and early 1960s (*Kallenrode*, 2004). In contrast to terrestrial weather, space weather forecasts must use data that are sparse. For example, meteorology has data from ASOS to use as input data into models, which allow for the use hundreds of input data points (ASOS, 2013). The sparsity of space weather data forces forecasters to rely on numerical approximations of space weather conditions that are not often corrected or modified by observations.

Influence

In meteorology, companies that fly airplanes or rescue teams, for example, make decisions based on daily forecasts, and each decision has varying costs and benefits (*Ahrens*, 1994). The same applies to space weather forecasts. The companies that own and operate GPS satellites have great interest in space weather forecasts. For example, the airline industry is interested in knowing whether to protect airplane passengers by re-routing polar flights, which has varying costs and benefits (*Lanzerotti*, 2001); (*J.B.L. Jones*, 2005). Finally, ground induced currents from geomagnetic storms can effect electrical systems (GMDTF, 2014).

Chapter 2: The Earth's Magnetosphere, Magnetohydrodynamics, and Magnetospheric Models

2.1 Earth's Magnetosphere

2.1.1 Discovery

Research into the understanding of what would eventually be called the magnetosphere started in the early 1600's when experiments were performed to determine if garlic caused magnets to demagnetize. A similarity was found between compass readings from a spherically shaped magnet and the direction of mariners' compass readings. An inference was made that Earth was also a magnet. Between the 1600's and mid-1900's there were many scientific advances in the understanding of space weather. An important result from S. Chapman and V. C. A. Ferraro in the early 1930's showed that solar streams were not traveling along a direct path into Earth's upper atmosphere; they were being deflected. Chapman and Ferraro estimated the deflection occurred at an upstream boundary, which is known today as the Chapman-Ferraro boundary (*Chapman and Ferraro*, 1930). In the 1950's, D. F. Martyn estimated the size of a "geomagnetic hollow" that Chapman and Ferraro predicted. This "geomagnetic hollow" would eventually be named the magnetosphere by Thomas Gold in 1959. Martyn estimated the distance to the boundary to be where the magnetic pressure from magnetic field originating in Earth's core balanced the kinetic pressure from a solar stream. In 1953, L. R. O. Storey researched whistlers caused from lightning. Storey estimated that there must be plasma in the "geomagnetic hollow" due to the way that Very Low Frequency (VLF) waves traveled between Earth's hemispheres along field lines that passed through the magnetosphere. When the U.S. and U.S.S.R. launched spacecraft to measure space weather parameters, they found that plasma was trapped between Earth and the Chapman-Ferraro

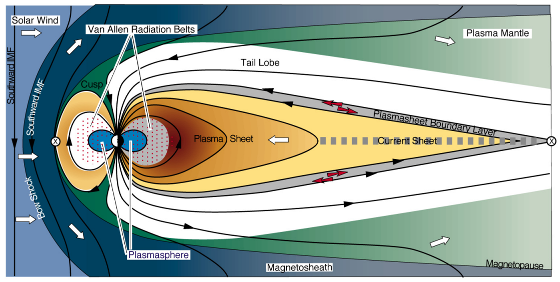

Figure 2.1: The regions of Earth's magnetosphere (from Rice University, 2014).

boundary, which was not a part of the Chapman and Ferraro model of the magnetosphere (*Kennel*, 1995).

2.1.2 Shape

Based on the Chapman-Ferraro model, a calculation of the magnetopause location could be made based on the balance between the kinetic pressure of the solar wind and the magnetic pressure due to Earth's magnetic field. The prediction of this model is a magnetopause at approximately 10 Earth radii (R_E), an overall teardrop shape, and a tail position between 50 and $100R_E$. The processes that cause the bell shape in the magnetosphere are (1) viscosity and reconnection and (2) change in solar wind density at the magnetopause.

2.1.3 Reconnection

Reconnection is a change in the topology of a magnetic field such that the connectivity of field lines are changed in such a way that allows rapid conversion of magnetic energy into kinetic energy. Reconnection is accepted to be the source of the massive energy release associated with solar flares. Modern issues with reconnection involve questions about how such a large amount of energy can be released in a very short amount of time. Solar flares can release energy in the solar corona in approximately 100 seconds. Ideal magnetohydrodynamics (MHD) can account for the time scale of energy release but not for the amount of energy released. Non-ideal MHD accounts for the release of a larger amount of energy but cannot match the short time scales (Scholarpedia, 2014). Two approaches were made to describe how non-ideal MHD could have faster reconnection. One used a high plasma resistivity, and the other used small dissipation scales. Sweet and Parker were the first to develop a MHD model which had fast reconnection (by adding anomalous resistivity.) Another model was devised by Petschek in 1964 in which the current sheet was thinner than that of Sweet and Parker. This accounted for the small time scales and is accepted today as the explanation for observations of fast reconnection (*Priest and Forbes*, 2000).

2.1.4 Reconnection in the Magnetosphere

After the discovery that the solar wind was magnetized, *Dungey* (1961) proposed a new model of the magnetosphere that was significantly different from the Chapman-Ferraro model. In the Dungey model, field lines from the magnetosphere connect back into the solar wind, as shown in Figure 2.1. The Chapman-Ferraro model maps the fields lines between two hemispheres. Dungey's model is considered open while the Chapman-Ferraro model is closed. Dungey's model has two null points (shown as a white circles with an x in Figure 2.1), which are regions where there is zero magnetic field (and reconnection) due to the cancellation of opposing magnetic fields. Dayside reconnection is primarily influenced by the orientation of the interplanetary magnetic field (IMF). The magnetic field of Earth has a northward orientation at the magnetopause. If the IMF is in the southward direction, reconnection can occur. If the IMF direction is northward, minimal or no reconnection occurs (*Priest and Forbes*, 2000).

The Reconnecting Magnetosphere

The following section describes a long-supported view of the magnetosphere (*Kennel*, 1995).

As shown in Figure 2.2 when passing through the bow shock (in the Earthward direction), there is a velocity decrease, a B increase at both the bow shock and magnetopause, density increase at the bow shock, and density decrease at the magnetopause.

During a magnetotail crossing, as shown in *Runov et al.* (2006) and *Hwang et al.* (2013),

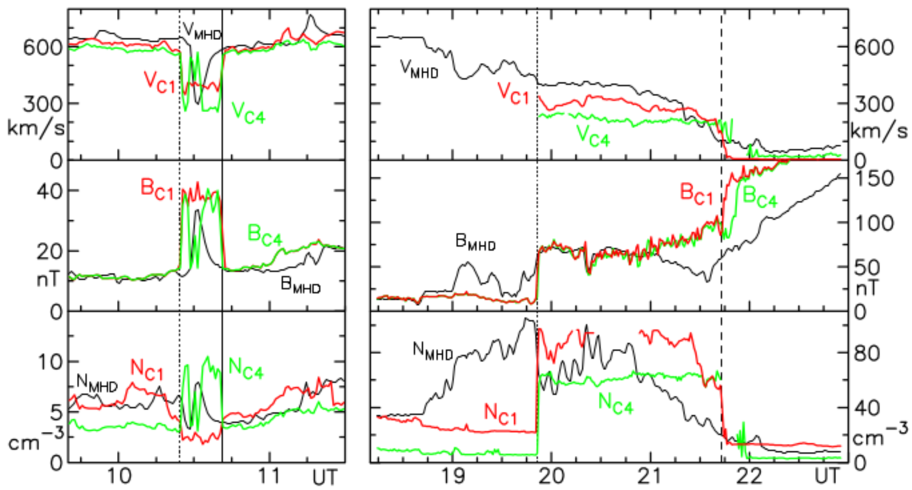

Figure 2.2: Satellite measurements of velocity, magnetic field strength, and number density taken from Cluster 1 and Cluster 4 instruments as they cross through Earth's bow shock and magnetopause (from *Tatrallyay et al.*, 2012).

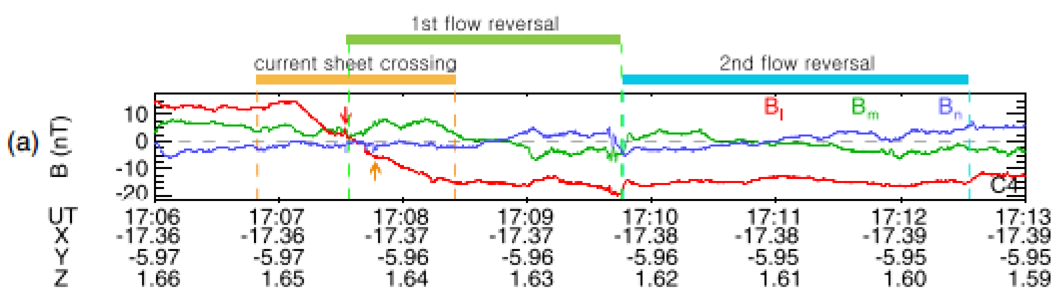

Figure 2.3: Cluster 4 measurements of magnetic field strength as it crosses the current sheet in the magnetotail with time on the x axis; l, m, n represent current-sheet coordinates (from *Hwang et al.*, 2013).

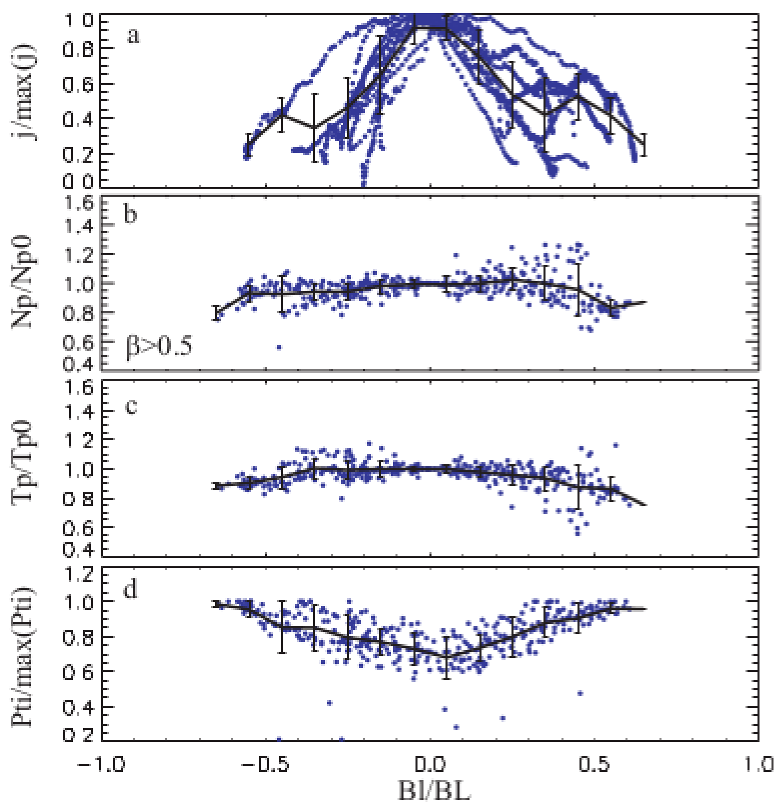

Figure 2.4: Profiles of the (a) normalized current density, (b) normalized proton number density, (c) normalized proton temperature, (d) the sum of magnetic and ion pressures, versus normalized main magnetic field (from *Runov et al.*, 2006).

there is a velocity increase as the distance from the current sheet decreases. The magnetic field decreases and reverses direction as the current sheet is crossed, as shown in Figure 2.3. The number density increases as the distance to the current sheet decreases, as shown in Figure 2.4 (*Kennel*, 1995).

Based on many measurements similar to that described above for magnetopause and magnetotail crossings, our general understanding of the reconnecting magnetosphere is as follows and will be used for comparison to MHD model output in the experiments performed:

- B_z
  - When the B_z^{IMF} is in the same direction of Earth's dipole, there is a larger magnetic field strength and thus an increase in magnetic pressure.
  - A negative B_z^{IMF} and Earth's dipole oppose each other and decrease the magnetic pressure at the magnetopause. During these conditions field lines reconnect with the IMF and travel tailward.
  - When the magnetic pressure at the magnetopause decreases, the balance between the magnetic and kinetic pressures will change causing the magnetopause location to move Earthward.
  - Due to the stretching of the magnetic field tailward of Earth, oppositely directed magnetic field lines are moved closer causing the magnetic field in the current sheet region to approach zero.
- ρ
  - As plasma travels Earthward from the Sun and encounters the magnetic field of Earth, it slows down. The plasma will eventually cross from supersonic to subsonic, creating a shock ahead of the magnetopause that is called the bow shock. Between the bow shock and magnetopause, plasma is compressed leading to higher densities.
  - The stretching of magnetic field in the magnetotail causes oppositely directed magnetic field lines to become close enough to one another for reconnection to

occur. This occurs in a plane called the current sheet and it separates the two opposing magnetic field directions. When reconnection occurs in the current sheet, a flow of new plasma replaces the plasma loss leading to an increase of densities.

- U_x
  - The velocity of the plasma in the solar wind is supersonic. Inside the magnetosphere there is minimal solar wind velocity. As the solar wind is slows, there is a point at which it switches from supersonic to subsonic. This region is known as the bow shock.
  - With the reconnection in the magnetotail occurring in the plasma sheet, there is a flow of plasma both towards and away from Earth on each side of the reconnection line. This movement is the reason that increases in velocities are observed as distance from the plasma sheet neutral line decreases.

2.1.5 Substorms

The magnetosphere is constantly influenced by changes in the solar wind. The direction of the IMF has the most influence. Energy from reconnection on the dayside magnetopause from a southward IMF transfers to the magnetotail and causes a stretching of field lines as they are dragged tailward by the solar wind. The stretching of the field lines brings magnetic field lines of opposing direction close to one another. Two opposing magnetic fields very close in proximity cause a sheet of current to form. Reconnection causes a large amount of the stored energy in the magnetotail to travel at high velocities towards Earth. The amount of stored energy in each reconnection event is different, and so are the effects measured at Earth. These events, as measured at Earth, are associated with substorms. On the dayside, during times of southward IMF, the magnetopause position varies. Many satellites have crossed the magnetopause boundary. In 1968, the OGO 5 satellite traveled towards Earth from the solar wind. The satellite recorded approximately 10 magnetopause crossings. The first crossing was made when the solar wind magnetic field was northward; shortly after this crossing, the magnetic field turned southward and the satellite crossed the magnetopause once again, giving the first measurement of the effects of southward IMF on the dayside magnetopause. On the nightside, as the magnetopause shifts Earthward, the polar cusps move towards the equator, and the thickness of the magnetotail increases (*Kennel*, 1995).

2.2 Magnetohydrodynamics

Magnetohydrodynamics describe the physics of magnetized fluid flow. Computational models solve the MHD equations for a large number of points in a specified domain.

2.2.1 Single Species

In 1872, Boltzmann derived equations that are used today to describe the dynamics of a system that is not in thermodynamic equilibrium. This is the starting point for the derivation of the ideal MHD equations.

Boltzman Equation

The derivation of the single species MHD equations begins with the Boltzmann equation for the probability distribution function $f_s(\mathbf{x}, \mathbf{v}, t)$ of species s :

$$\frac{\partial f_s}{\partial t} + \mathbf{v} \cdot \nabla f_s + \mathbf{a} \cdot \nabla_v f_s = \left.\frac{\partial f_s}{\partial t}\right|_{coll} \tag{2.1}$$

Where $(\mathbf{x}, \mathbf{v}, t)$ represents position, velocity, and time, respectively and $\mathbf{a}$ represents acceleration. Multiplying equation 2.1 by a function of velocity $\chi(\mathbf{v})$ and integrating over velocity gives:

$$\int \chi \frac{\partial f_s}{\partial t} d^3\mathbf{v} + \int \chi \mathbf{v} \cdot \nabla f_s d^3\mathbf{v} + \int \chi \mathbf{a} \cdot \nabla_v f_s d^3\mathbf{v} = \int \chi \left.\frac{\partial f_s}{\partial t}\right|_{coll} d^3\mathbf{v} \tag{2.2}$$

This can be re-written as:

$$\frac{\partial}{\partial t}\int \chi f_s d^3\mathbf{v} + \nabla \cdot \int \mathbf{v}\chi f_s d^3\mathbf{v} - \int f_s(\mathbf{a}\cdot\nabla_v)\chi d^3\mathbf{v} = \frac{\partial}{\partial t}\int \chi f_s\Big|_{coll} d^3\mathbf{v} \tag{2.3}$$

where $\Big|_{coll}$ refers to collisions between different species.

Using the definition of the average value $<\chi>$ of a property χ of $n_s <\chi>_s = \int \chi f_s d^3\mathbf{v}$, where n_s is the number density of species a, equation 2.3 becomes:

$$\frac{\partial}{\partial t}(n_s <\chi>_s) + \nabla \cdot (n_s <\chi\mathbf{v}>_s) - n_s <(\mathbf{a}\cdot\nabla_v)\chi>_s = \frac{\partial}{\partial t}(n_s <\chi>_s)\Big|_{coll} \tag{2.4}$$

which is the generalized transport equation (*Kominsky*, 2013).

Conservation of Mass

The law of the conservation of mass states that in a closed system the mass does not change with time (Con, 2013b). The equation for the conservation of mass in MHD starts with equation 2.4. For species with a mass m_s, we can define:

$$\chi = m_s$$

$$<\chi> = m_s$$

$$\mathbf{u_s} = <\mathbf{v_s}>$$

$$\mathbf{v} = \mathbf{u_s} + \mathbf{c_s}$$

$$<\mathbf{v_s}> = <\mathbf{u_s} + \mathbf{c_s}>$$

$$<\mathbf{c_s}> = 0$$

$$<\chi\mathbf{v}>_s = m_s <\mathbf{v_s}> = m_s\mathbf{u_s}$$

$$\nabla_v \chi = 0$$

Inserting these into equation 2.4 gives:

$$\frac{\partial}{\partial t} n_s m_s + \nabla \cdot (n_s m_s \mathbf{u_s}) = m_s \int \frac{\partial f_s}{\partial t}\bigg|_{coll} \tag{2.5}$$

Defining the collision term $S_s = \left(\frac{\partial \rho_s}{\partial t}\right)_{coll}$, and with $\rho_s = n_s m_s$ gives:

$$\frac{\partial \rho_s}{\partial t} + \nabla \cdot (\rho_s \mathbf{u_s}) = \left(\frac{\partial \rho_s}{\partial t}\right)_{coll} = S_s, \tag{2.6}$$

which is the equation for the conservation of mass (*Kominsky*, 2013).

Conservation of Momentum

The derivation of conservation of momentum is similar to that of mass. Momentum cannot be created or destroyed and the amount of momentum in a specified domain will remain constant in a closed system (Con, 2013c). Using the property $m_s \mathbf{v}$ and defining $\chi = m_s \mathbf{v}$, equation 2.1 can be written as:

$$\frac{\partial}{\partial t}(\rho_s < \mathbf{v} >_s) + \nabla \cdot (\rho_s < \mathbf{vv} >_s) - n_s < (\mathbf{F_s} \cdot \nabla_v)\chi >_s = m_s \int \mathbf{v} \left(\frac{\partial f_s}{\partial t}\right)_{coll} \tag{2.7}$$

Defining $\mathbf{v} = \mathbf{u}_s$ and $< \mathbf{c}_s >= 0$ and solving for $\nabla \cdot (\rho_s < \mathbf{vv} >_s)$ and $-n_s < (\mathbf{F_s} \cdot \nabla_v)\chi >_s$ with the pressure tensor defined $P_s = \rho_s < \mathbf{c_s c_s} >$, we arrive at the equation for the conservation of momentum (*Kominsky*, 2013):

$$\frac{\partial \rho_s \mathbf{u_s}}{\partial t} + \nabla \cdot (\rho_s \mathbf{u_s u_s}) + \nabla \cdot (P_s) - n_s < \mathbf{F} >= \mathbf{A_s} \tag{2.8}$$

Conservation of Energy

The derivation of conservation of energy is similar to that of mass and momentum. Energy cannot be created or destroyed and the amount of energy in a specified domain will remain constant in a closed system (Con, 2013a). Starting with equation 2.1 and using the property $\frac{1}{2}m_s v^2$ and defining $\chi = \frac{1}{2}m_s v^2 = \frac{1}{2}m_s(\mathbf{v}\cdot\mathbf{v})$, then $\nabla_v \chi = \frac{1}{2}m_s \nabla_v(\mathbf{v}\cdot\mathbf{v}) = m_s(\mathbf{v}\cdot\nabla_v)\mathbf{v} = m_s\mathbf{v}$ gives:

$$\sum_s \frac{\partial}{\partial t}(\frac{1}{2}\rho_s < v^2 >_s) + \sum_s \nabla \cdot (\frac{1}{2}\rho_s < v^2 \mathbf{v} >_s) - \sum_s n_s < \mathbf{F}\cdot\mathbf{v} >_s = \frac{\partial}{\partial t}(\frac{1}{2}\rho_s < v^2 >_s)\Big|_{coll} \tag{2.9}$$

Solving for $\nabla \cdot (n_s < \chi \mathbf{v} >_s)$, $-n_s < \mathbf{a}\cdot\nabla_v \chi >_s$, and $< \mathbf{F}\cdot\mathbf{c_s} >$, this gives an equation for conservation of energy:

$$\frac{\partial \epsilon_s}{\partial t} + \nabla \cdot (\epsilon_s \mathbf{u}_s) + \nabla \cdot (P_s \cdot \mathbf{u}_s) + \nabla \cdot \mathbf{q}_s - n_s q_s \mathbf{u}_s \cdot \mathbf{E} - \rho_s \mathbf{u}_s \cdot \mathbf{g} = M_s \tag{2.10}$$

where

$$\epsilon_s = \frac{p_s}{\gamma - 1} + \frac{1}{2}\rho_s u_s^2$$

$$P_s = \frac{1}{d}\sum_{ij} P_{aij}\delta_{ij} = \frac{1}{d}\sum_i P_{aii}$$

$$\mathbf{q}_s = \frac{1}{2}\rho_s < c_s^2 \mathbf{c}_s >$$

2.2.2 Single Fluid

The previous equations are applicable to each species in a plasma. To allow for the treatment of the fluid as a whole, the individual species can be summed. The following properties are defined by a sum over all species.

$$\rho = \sum_s n_s m_s$$

$$\rho\mathbf{u} = \sum_s n_s m_s \mathbf{u}_s$$

$$\rho_q = \sum_s n_s q_s$$

$$\mathbf{J} = \sum_s n_s q_s \mathbf{u}_s$$

Conservation of Mass

Using the above summations, equation 2.6 becomes:

$$\frac{\partial \rho}{\partial t} + \nabla \cdot (\rho\mathbf{u}) = 0 \tag{2.11}$$

Conservation of Momentum

Using the above summations, equation 2.8 becomes:

$$\sum_s \frac{\partial \rho_s \mathbf{u}_s}{\partial t} + \sum_s \nabla \cdot (\rho_s \mathbf{u}_s \mathbf{u}_s) + \sum_s \nabla \cdot (P_s) - \sum_s n_s (q_s(\mathbf{E} + \mathbf{u}_s \times \mathbf{B}) + m_s \mathbf{g}) = \sum_s \mathbf{A}_s$$

Because the sum of the collision terms is zero, and total momentum is conserved, the previous equation can be written as:

$$\frac{\partial \rho\mathbf{u}}{\partial t} + \nabla \cdot \sum_s \rho_s \mathbf{u}_s \mathbf{u}_s + \nabla \cdot \sum_s P_s - \rho_q \mathbf{E} - \mathbf{J} \times \mathbf{B} - \rho\mathbf{g} = 0$$

Solving for the summations results in an equation for the conservation of momentum for a single fluid:

$$\frac{\partial \rho \mathbf{u}}{\partial t} + \nabla \cdot (\rho \mathbf{u}\mathbf{u}) + \nabla \cdot P - \rho_q \mathbf{E} - \mathbf{J} \times \mathbf{B} - \rho \mathbf{g} = 0 \tag{2.12}$$

Conservation of Energy

Using the above summations, equation 2.10 becomes:

$$\sum_s \frac{\partial \epsilon_s}{\partial t} + \sum_s \nabla \cdot (\epsilon_s \mathbf{u}_s + P_s \cdot \mathbf{u}_s + \mathbf{q}_s) - \sum_s n_s q_s \mathbf{u}_s \cdot \mathbf{E} - \sum_s \rho_s \mathbf{u}_s \cdot \mathbf{g} = 0$$

Upon solving for $\sum \rho_s u_s^2$, $\sum_s \epsilon_s$, and $\sum_s p_s \mathbf{u_s}$, where the total scalar pressure is

$$p = \frac{1}{d} \sum_i P_{ii} = \frac{\gamma - 1}{2} \sum_s \rho_s < (c_s + w_s)^2 >= \sum_s p_s + \frac{\gamma - 1}{2} \sum_s \rho_s w_s^2,$$

and the total heat flux is

$$\mathbf{q} = \frac{1}{2} \sum_s \rho_s < (c_s + w_s)^2 (\mathbf{c}_s + \mathbf{w}_s) >,$$

this gives conservation of energy:

$$\frac{\partial \epsilon}{\partial t} + \nabla \cdot (\epsilon \mathbf{u} + P \cdot \mathbf{u} + \mathbf{q}) - \mathbf{J} \cdot \mathbf{E} - \rho \mathbf{u} \cdot \mathbf{g} = 0. \tag{2.13}$$

Maxwell's Equations

Maxwell's equations relate $\mathbf{E}$, $\mathbf{J}$, and $\mathbf{B}$ from the previous plasma equations:

Gauss's law:

$$\nabla \cdot \mathbf{E} = \frac{\rho_q}{\epsilon_0}$$

Gauss's law for magnetism:

$$\nabla \cdot \mathbf{B} = 0$$

Faraday's law:

$$\nabla \times \mathbf{E} = -\frac{\partial \mathbf{B}}{\partial t}$$

Ampere's law:

$$\nabla \times \mathbf{B} = \mu_0(\mathbf{J} + \epsilon_0 \frac{\partial \mathbf{E}}{\partial t}),$$

where μ_0 is the permeability, ϵ_0 is the permittivity, $\mathbf{E}$ is the electric field, $\mathbf{B}$ is the magnetic field, $\mathbf{J}$ is the current, and ρ_q is the charge density.

Conservation of Current Density

Using Maxwell's equations, the single species momentum equation multiplied by $\frac{q_s}{m_s}$ and summed over species gives:

$$\frac{\partial}{\partial t}\sum_s n_s q_s \mathbf{u}_s + \nabla \cdot (\sum_s n_s q_s \mathbf{u}_s \mathbf{u}_s) + \nabla \cdot (\sum_s \frac{q_s}{m_s} P_s) - \sum_s n_s \frac{q_s}{m_s} < \mathbf{F} >= \sum_s \frac{q_s}{m_s} \mathbf{A}_s$$

Noting that:

$$\mathbf{J} = \sum_s n_s q_s \mathbf{u}_s$$

gives conservation of current density:

$$\frac{\partial \mathbf{J}}{\partial t} + \nabla \cdot (\mathbf{Ju} + \mathbf{uJ} - \rho_q \mathbf{uu} + \mathbf{P}_q) - \sum_s n_s \frac{q_s}{m_s} < \mathbf{F} >= \sum_s \frac{q_s}{m_s} \mathbf{A}_s \tag{2.14}$$

2.2.3 Ideal

To simplify the single fluid MHD equations, the following assumptions are made:

- The time derivative of E is small.
- Isotropic Pressure:

  If the pressure tensor P is replaced with $p\mathbf{I}$, then $\nabla \cdot P = \nabla p$.
- Charge neutrality: $\rho_q = 0$.
- Neglect small terms:

  Terms involving P_q can be neglected if p_e is small.
- Single ion flow with collision term approximation:

  Used to simplify the magnetic field differential equation.
- Perfect conductivity:

  σ is infinite so that $\mathbf{E} + \mathbf{u} \times \mathbf{B} = \frac{\mathbf{J}}{\sigma} \simeq 0$, giving $\mathbf{E} = -\mathbf{u} \times \mathbf{B}$

Using these assumptions along with Maxwell's equations, the conservation equations become (*Kominsky*, 2013):

- Conservation of Mass

$$\frac{\partial \rho}{\partial t} + \nabla \cdot (\rho \mathbf{u}) = 0$$

- Conservation of Momentum

$$\frac{\partial \rho \mathbf{u}}{\partial t} + \nabla \cdot \left[\rho \mathbf{u}\mathbf{u} + (p + \frac{B^2}{2\mu_0})\mathbf{I} - \frac{1}{\mu_0}\mathbf{B}\mathbf{B} \right] - \rho \mathbf{g} = 0$$

- Conservation of Energy

$$\frac{\partial \epsilon}{\partial t} + \nabla \cdot \left[(\epsilon + p + \frac{B^2}{2\mu_0})\mathbf{u} + \mathbf{q} - \frac{1}{\mu_0}(\mathbf{u} \cdot \mathbf{B})\mathbf{B} \right] - \rho \mathbf{u} \cdot \mathbf{g} = 0$$

- Conservation of Magnetic Flux

$$\frac{\partial \mathbf{B}}{\partial t} + \nabla \cdot (\mathbf{uB} - \mathbf{Bu}) = 0$$

2.3 Magnetospheric Models

To most accurately model the magnetosphere, the collisionless Boltzmann equations for individual species along with Maxwell's equations should be used. The use of these equations in a computational model is costly because the computational complexity of the algorithms for their solutions are high (*Raeder*, 2003). A more efficient solution is to use the ideal MHD equations. In the magnetospheric community, there are three often-used models that implement ideal MHD. The way that each magnetospheric model approaches these equations gives them their uniqueness.

2.3.1 Grid and Geometry

Each model uses a choice of a numerical grid and numerical method to solve the MHD equations. For the magnetosphere, Earth's magnetopause can expand to tens of Earth radii towards the Sun, so the simulation domain for the grid must be at least this large. The tailward boundary can be $\geq 200\ R_E$, and the transverse regions are typically $\geq 50\ R_E$. The choice for the numerical grid resolution and size depends on the computational resources; the grid choice is also influenced by the numerical method. Grids used in MHD models include:

- Uniform Cartesian

  Uniform grids as shown in Figure 2.5 have equal spacing in all dimensions. The amount of programming required and the computational resources used are low, and parallelization is the most straightforward to implement. The most significant limitation of the uniform cartesian grids is that the same resolution must be used everywhere in the domain. The optimal resolution is not necessarily the same for all

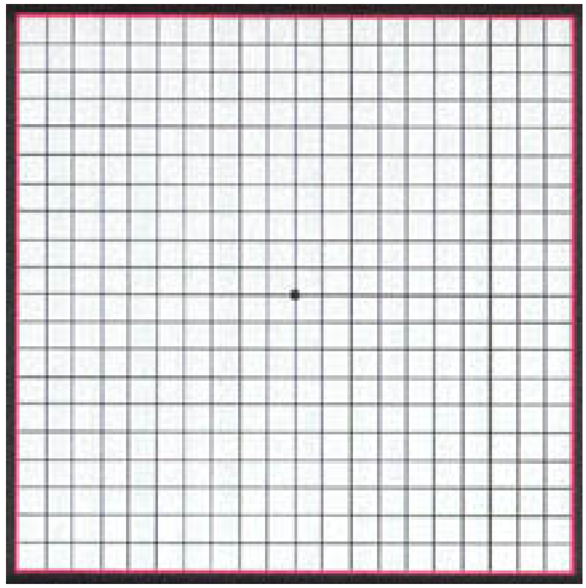

Figure 2.5: Uniform Cartesian Grid (from StackOverflow, 2014).

regions of the domain.

- Stretched Cartesian

  Stretch Cartesian grids, as shown in Figure 2.6, can be "stretched" in each dimension while still maintaining the ease of programming comparable to a uniform cartesian grid. The stretching can allow for higher resolution in regions around Earth, magnetopause, and bow shock regions, and other regions where needed, and lower resolution in areas that do not need it such as the distant magnetotail. Specifically for the magnetosphere, this grid type is very well adapted.

- Structured Adaptive Mesh Refinement (SAMR)

  SAMR grids, similar to that shown in Figure 2.7, have higher grid resolutions in regions that need it. These higher resolutions are added and removed as time progresses as needed. Different refinements are possible, which requires a larger coding and computational resource cost, yet SAMR can provide the most accurate solutions (*Raeder*, 2003).

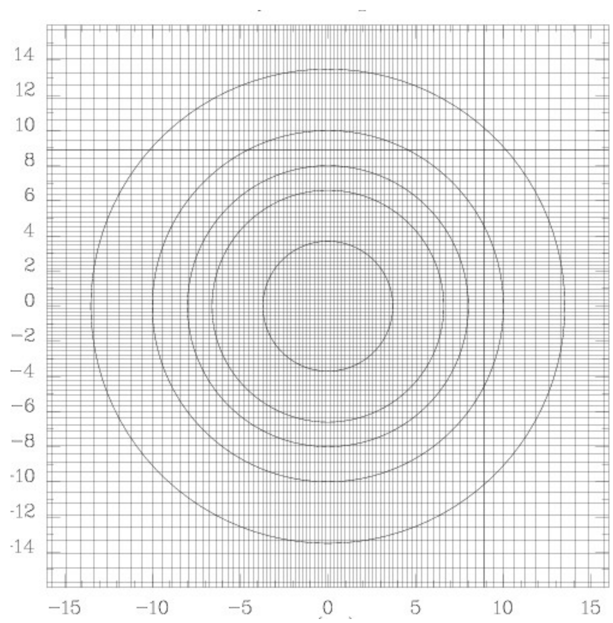

Figure 2.6: Stretched Cartesian Grid (from Univeristy of New Hampshire, 2014).

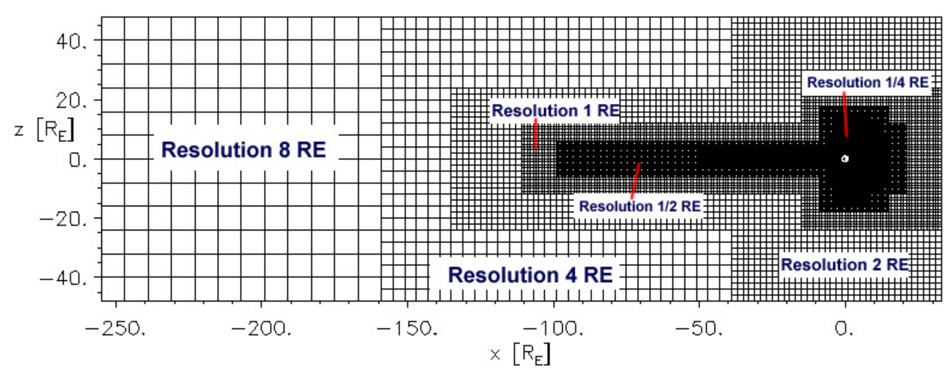

Figure 2.7: Structured Adaptive Mesh Refinement Grid (from NASA, 2014).

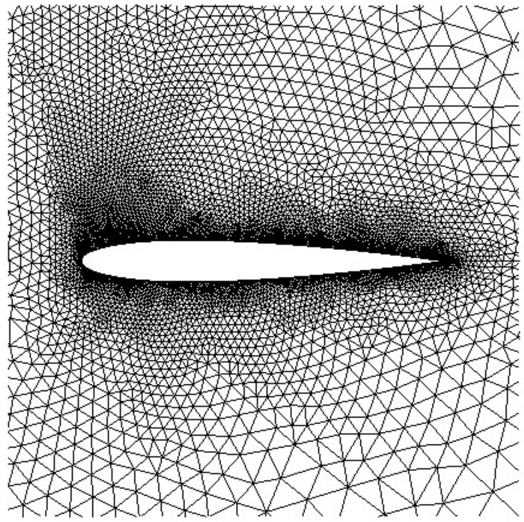

Figure 2.8: Unstructured Grid (from Delft University of Technology, 2014).

- Unstructured Grid

  In an unstructured grid, as shown in Figure 2.8, the shape of each cell is typically different than its neighbors. These grids are typically used in finite element and finite volume methods. They are very difficult to program, computationally expensive, and are difficult to parallelize. Their major benefit is the ability to form well to the object they model.

2.3.2 Boundary Conditions

On the sunward side of the grid boundary, the boundary conditions can be fixed or time dependent. As solar wind data is measured at only a few points near the boundary, it is difficult to determine the extended structure of the solar wind boundary conditions. On all other boundaries, free flow conditions apply with the exception that the $\nabla \cdot \mathbf{B} = 0$ condition is used to derive the normal of the magnetic field (and should be consistent with the numerical scheme) (*Raeder*, 2003).

2.3.3 Initial Conditions

On the sunward side of Earth, there is a region where its magnetic field reaches near zero. The initial conditions for B are created by placing a mirror dipole sunward of Earth such that a plane with zero magnetic field exists close to Earth on the sunward side. The initial solar wind and magnetic field then replaces the mirror dipole sunward of the near zero B region. The plasma initial conditions are typically set at a temperature of 5000 [°K] and a density of 0.1 $[cm^{-3}]$. With these initial conditions, it can take up to ond hour for the magnetosphere to start forming. Because the magnetosphere has a memory of previous conditions that can last many hours, it is important to allow at least a few hours of preconditioning time before using input data for a specific event (*Raeder*, 2003). To date, no evaluation of the influence of preconditioning on model results has been published.

2.3.4 Spatial Discretization

There are four different approaches used for spatial discretization in MHD models of the magnetosphere: finite differences, finite volumes, finite elements, and spectral.

Finite difference methods are most used in magnetospheric models, and some of the concepts from finite differencing schemes are found in the other methods. Conservative finite difference schemes have the best fit for global MHD simulations (*Raeder*, 2003).

2.3.5 Numerical Implementation

There are simple differencing schemes that can have 2nd order accuracy. Schemes such as predictor-corrector and leap-frog can be accurate, but they lack stability, which is required in a majority of the computational domain. The Courant-Friedricks-Levy (CFL) criteria limits the timestep for stability. The Alfvén speed can be extremely large. A "Boris Correction" or some variant is used to limit the Alfvén speed allowing for larger time steps without increasing errors in the solution (*Raeder*, 2003).

2.3.6 The Open Global Geospace Circulation Model

The Open Global Geospace Circulation Model (OpenGGCM) solves the ideal MHD equations for the magnetosphere using a conservative finite difference method for the gas dynamic part of the normalized ideal MHD equations. The equations solved are:

$$\frac{\partial \rho}{\partial t} = -\nabla \cdot (\rho \mathbf{v})$$

$$\frac{\partial \rho \mathbf{v}}{\partial t} = -\nabla \cdot (\rho \mathbf{v}\mathbf{v} + pl) + \mathbf{j} \times \mathbf{B}$$

$$\frac{\partial e}{\partial t} = -\nabla \cdot (\{e + p\}\mathbf{v}) + \mathbf{j} \cdot \mathbf{E}$$

$$\frac{\partial \mathbf{B}}{\partial t} = -\nabla \times \mathbf{E}$$

$$\nabla \cdot \mathbf{B} = 0$$

$$\mathbf{E} = -\mathbf{v} \times \mathbf{B} = \eta \mathbf{j}$$

$$\mathbf{j} = \nabla \times \mathbf{B}$$

$$e = \frac{1}{2}\rho v^2 + \frac{p}{\gamma - 1}$$

The OpenGGCM treats the $\mathbf{j} \times \mathbf{B}$ and $\mathbf{E} \cdot \mathbf{j}$ terms as source terms due to low plasma beta (the ratio of plasma pressure to the magnetic pressure) and large gradients in the magnetic field that do not allow for a full conservative formalism. The magnetic field is initialized with the superposition of Earth's dipole such that at approximately $16R_E$, B_z is zero. After this, the magnetic field from $16R_E$ sunward is replaced by the initial solar wind magnetic field. This ensures the $\nabla \cdot \mathbf{B} = 0$ condition for ideal MHD is met (CCMC, 2014).

2.3.7 The Block Adaptive-Tree Source Roe-type Upwind Scheme Model

The Block Adaptive-Tree Source Roe-type Upwind Scheme (BATS-R-US) model uses a finite volume discretization and solves the conservative MHD equations:

$$\frac{\partial \rho}{\partial t} + \mathbf{u} \cdot \nabla p + \rho \nabla \cdot \mathbf{u} = 0$$

$$\rho \frac{\partial \mathbf{u}}{\partial t} + \rho \mathbf{u} \cdot \nabla \mathbf{u} + \nabla p - \mathbf{j} \times \mathbf{B} = 0$$

$$\frac{\partial \mathbf{B}}{\partial t} + \nabla \times \mathbf{E} = 0$$

$$\frac{\partial p}{\partial t} + \mathbf{u} \cdot \nabla p + \gamma p \nabla \cdot \mathbf{u} = 0$$

$$\mathbf{j} = \frac{1}{\mu_0} \nabla \times \mathbf{B}$$

$$\mathbf{E} = -\mathbf{u} \times \mathbf{B}$$

The $\nabla \cdot \mathbf{B}$ constraint can be implemented using four different divergence control schemes. The eight wave, diffusive/parabolic, projection, and a conservative form of the constrained transport scheme extended to adaptive grids. The grid is set using an adaptive mesh refinement technique. This technique adapts specific sections of the computational domain so that areas where higher resolution or lower resolution are most appropriate can be used. If a higher resolution is needed, then a cell is divided into eight children. When lower resolution is needed, a block of eight is grouped into one cell. Initial conditions at boundaries of the computational domain are set to solar wind conditions and the mirror dipole method described previously is used.

Chapter 3: Validation

3.1 Overview

Validation and Verification analyses help model users and developers gain a greater confidence and understanding of the accuracy of model output and its numerical implementation, respectively. Validation analyses are most often used to show the user community how the model output compares with measured data. Verification analyses are used to ensure that the numerical implementation of the mathematics are correct.

Model validation encompasses many ways of looking at model output (*Sargent*, 2004). There are many different methods of validation, and the appropriate method for a specific model depends on its intended use. Sargent *Sargent* (2004) describes fifteen different methods of validation:

- **Animation**: The output of the model is plotted graphically over a time range.
- **Comparison to other models**: The results from previously validated models are compared to that of a new model.
- **Degenerative tests**: The degeneracy in the behavior of the model is tested with a specific selection of input and internal parameters that are expected to result in degenerate model output.
- **Event validity**: Important events predicted by a model are compared to the important events of the real system.
- **Extreme condition test**: The output of the model should be plausible even when unlikely or rare conditions are input into the system initially.

- **Face validity**: Discussing the models output with scientists who are experienced and knowledgeable about the modeled system.

- **Historical Data Validation**: If historical data exists, it is used as input into a model and the output is compared to the real system.

- **Historical methods**

- **Internal validity**: Several runs with the same input are made to determine the amount of variability in the model. The larger the variability, the larger the questionability of the model.

- **Multistage validation**: Using multiple validations at once.

- **Operational graphics**: Various model forecast performance measures are graphically displayed as the model progresses through time.

- **Parameter variability - sensitivity analysis**: Changing the input and internal values of a model to determine the effect of the model's output/behavior.

- **Predictive validation**: Models are used to predict the system's behavior, and comparisons are made to the system's actual behavior to determine if they are similar.

- **Traces**: The internal behavior of the model is followed to determine if the logic in the model is correct and the needed accuracy is obtained.

- **Turing tests**: Scientists knowledgeable about the system are asked to determine if they can distinguish a model from the measurements from the modeled system.

Sargent (2004) defines two basic approaches to verification of computational models as static and dynamic testing.

- **Static Testing**: In static testing, the model is analyzed for correctness by using techniques such as structured walk-throughs, correctness proofs, and examining the structure properties of the program.

- **Dynamic Testing**: In dynamic testing, the model is tested with differing conditions where the data received is used to determine if the program has correct implementations. Four dynamic tests described by Sargent are traces, investigations of input-output relations using different validation techniques, internal consistency checks, and reprogramming critical components to determine if the same results are obtained.

The following two subsections contain examples of the types of validation currently used in both terrestrial weather and space weather. Research on terrestrial weather prediction models have involved primarily *parameter variability* studies that test the physics of the model using artificial input parameters. Research on space weather prediction models have involved primarily *predictive validation* using measured solar wind input data.

3.2 Terrestrial Weather Validation

Terrestrial weather models have been in operation by the NWS longer than space weather models have with the Space Weather Prediction Center (SWPC). Terrestrial weather methods of validation have been improved over that time and their validation methods should be considered for space weather modeling.

A majority of terrestrial weather models used for prediction use the comparison to other models validation technique described in (*Sargent*, 2004). This is similar to what is currently done with space weather models used in prediction. The following terrestrial weather models, both for weather and climate prediction, show *predictive* and *parameter variability - sensitivity analysis* validation techniques, respectively. The following three examples are representative of modern terrestrial weather validation.

Boznar et al. (2012) validates a short-term fine-resolution Weather Research and Forecasting (WRF) model by comparing its output to observations made in Slovenia. The complex terrain in Slovenia can cause problems with wind profiles in the models, and the motivation for this analysis was to determine how extremes in height were handled by the model. They found that the model performed better with stations that were on top of hills and worse with stations that were in basins and valleys. This is an example of *predictive validation.*

Molteni et al. (2006) performed a sensitivity analysis on the European Center for Medium-range Weather Forecasts (ECMWF) model in which a perturbation was input into the model to determine how it affected the output as a part of a larger validation effort. This is an example of a *parameter variability - sensitivity analysis.*

Andrejczuk et al. (2006) performed simulations of cloud-clear air interfacial mixing. In this study they use initial velocity fields made from high, moderate, and low intensity levels of turbulent kinetic energy input into the models. This is also an example of *parameter variability* as they use a variety of input conditions and then evaluate the model output.

Katzav (2011) argued that severe testing of climate model predictions (CMPs) should have a larger role in the assessment of CMPs. Severe testing is a *parameter variability* validation in which input variables are set to extreme values. *Katzav* (2011) suggested that the current view on model assessment, that CMP quality should depend on simulation accuracy, is insufficient reasoning and explains that severe testing addresses concerns about relying on successes that are based on results obtained from data accommodation. Secondly, severe testing helps test the maturity of the science underlying CMPs. Lastly, Katzav suggests that even though some severe testing may already occur, it is not nearly enough, and increased severity testing will help science progress. Severe testing is the term used by Katzav and is similar to *parameter variability. parameter variability* and severe (extreme condition) testing will be used in this dissertation.

3.3 Space Weather Validation

With a lack of measurements in the Sun-to-Earth domain, MHD modeling has been a key to predictive analysis in space weather, especially in regions where dense or long-term measurement do not exist. In recent years, there has been an increasing amount of attention to validation in the space weather modeling community as interest in transitioning models into operations increases. The number of space weather researchers that use *parameter variability* validation is limited. The following examples do not use *parameter variability* validation, but rather show the large use of the *comparison to other models* validation technique.

Taktakishvili et al. (2009) used a combination of the halo CME analytical cone model (*Xie et al.*, 2004) and the Enlil solar wind model (*Odstrcil*, 2003) to predict the CME arrival time at Earth using historical solar wind data. This is *historical data* validation. Because they also compared their results with two other models, they also employed the *comparison to other model* validation technique.

Pulkkinen et al. (2011) compared ground magnetometer predictions made by fourteen different models to the measurements made from twelve different geomagnetic observatories and used four different metrics to quantify the model performance for four different storm events. The three validation tests they used can be classified as *comparison to other models*, *predictive validation*, and *historical data* validation.

MacNeice (2009a) documented a set of procedures to test the prediction capability of the Wang-Sheeley-Arge (WSA) model (*Arge et al.*, 2003). *MacNeice* (2009b) discussed model results using data taken from the solar wind at Earth up to four days in advance of geomagnetic storms. Both papers used a *predictive validation* technique.

Garcia and Hughes (2007) performed a statistical comparison between the Lyon-Fedder-Mobarry magnetosphere MHD-based model (*Lyon et al.*, 2004) and empirical models of the magnetopause location to determine which better predicted the actual position of the magnetopause. This is an example of the *comparison to other models* validation technique.

Mozer and Briggs (2003) used the forecasts of 96 solar wind shocks at the L1 point made by the Hakamada-Akasofu-Fry (HAF) model (*Hakamada and Akasofu*, 1982) and compared it to real time data from the solar wind electron proton alpha monitor (SWEPAM) and MAG (magnetometer) instruments on the Advanced Composition Explorer (ACE) spacecraft (*Stone et al.*, 1998). This is an example of the *historical data validation* as well as *predictive validation.*

Owens et al. (2005) used the WSA model and 8 years of plasma measurements at the L1 point. A mean square error (MSE) metric was used to compare the model with the observations. Owens also performed the *predictive validation* via an event-based analysis in which the WSA was validated using hits, misses, and false alarms for the prediction of high speed enhancements (HSE).

Although *predictive validation* is the most commonly used method in space weather model analysis, the focus in this dissertation is on *parameter variability* as it allows a different perspective on space weather models. *Parameter variability* is different from *predictive validation* in the way that input conditions are used. *Predictive validation* uses measured data as input, while *parameter variability* uses input conditions that were not measured, but are representative of space weather conditions. The use of *predictive validation* in space weather can give model users confidence in and a better understanding of the best performing model under prototypical space weather conditions.

The most common validation approach used in space weather is one that compares model output to in-situ data. This type of validation is done frequently and offers a limited perspective on model behavior. There is still a need for a comprehensive understanding of space weather models. A comprehensive understanding can be accomplished through performing a wider variety of validation analyses. This dissertation aims to provide a foundation for a more comprehensive understanding of space weather models through inter- and intra-model comparisons using a new visualization tool and the validation method of *parameter variability - sensitivity analysis.*

Chapter 4: Experiments

Validation encompasses the entire methodology in how analysis on models are performed. *Sargent* (2004) categorized a large number of methods into a concise list. The list is not limited to a specific science domain or type of model, and when describing validation used in a research paper, a link can usually be made back to Sargent's list. Because the goal of understanding all information available about validation is large, it is typically researched in smaller and more specific pieces such that over time the information gained from the research will make it easier to understand validation as a whole.

The next three sections describe validation experiments that were performed to gain a better understanding of space weather models. Three magnetosphere models were studied using a less utilized, but important, validation method than that more commonly found in the space weather literature. In the first section, the responses of magnetospheric MHD models to a common space weather phenomenon that is linked to causing harmful effects on space-based technology is considered. This phenomena is a change in the z direction of the magnetic field in the upstream solar wind from positive to negative. In the second section, the effect of differences in preconditioning times for MHD magnetospheric models is analyzed. In the last section, the effects of two extreme space weather conditions on the MHD magnetospheric models is considered. First, conditions in space weather that cause high magnetospheric compression are analyzed and then conditions that cause low magnetospheric compression are considered. In all analyses, a tool specifically developed for this research, called model output difference imaging, is used to visualize the differences between model outputs.

4.1 Response to a reversal in B_z^{IMF} from positive to negative

4.1.1 Background

The first research done on the impact in the magnetosphere of a southward directed interplanetary magnetic field (B_s) was in the late 1960's and early 1970's when the Dungey theory of magnetospheric convection was tested. The support for Dungey's claim came from positive correlations between the AE geomagnetic index and the magnitude of B_s (*Maezawa*, 1976). *Gonzalez and Echer* (2005) analyzed 64 intense geomagnetic storms and showed that the time delay between the peak B_s and the minimum D_{st} value was approximately two hours. *Gonzalez and Echer* (2005) noted that because the typical storm duration was approximately ten hours for the storms studied, the two hour delay can represent up to 20% of the main phase of a typical storm. This is important to forecasters as they can use this information to predict that the minimum D_{st} will occur, on average, two hours after peak B_s.

Analysis was done on the interplanetary conditions that caused geomagnetic storms during solar cycle 23 (*Echer et al.*, 2008). One of the conclusions was that out of the 90 storm events considered, none of them occurred during northward IMF. They also found that the structures that led to the intense southward IMF, ordered from highest to lowest occurrence frequency, were magnetic clouds, sheath fields, combined magnetic cloud and sheath fields, and co-rotating interaction regions.

4.1.2 Motivation

There are many factors involved in the response of the magnetosphere to the solar wind. Numerous studies have been performed to offer explanations on why certain space weather events occur, and they have been tested with strong statistical support. To better understand how a change in a single variable effects the magnetospheric system, as approximated by MHD models, it was decided to perform a *parameter variability - sensitivity analysis* validation in which the only changing parameter was B_z^{IMF}, which changed from positive to negative. In this analysis, the other input variables (B_x^{IMF}, B_y^{IMF}, $\mathbf{V}$, ρ, and T) were kept constant to limit the number of factors that may influence model output and to simplify interpretation.

4.1.3 Methodology

When comparing two models through visual inspection of each output separately, there is difficulty involved in determining what the major differences between the two are. The motivation for developing a model output differencing visualization tool was to make this type of comparison easier. First, data from each of the MHD magnetospheric models was placed and interpolated onto one common grid. An open source tool, Kameleon (*Kameleon*, 2013), developed by the CCMC, was used for the interpolation. Kameleon is a C++ based code that supports a few of the available CCMC MHD magnetospheric models. The Kameleon software supports the OpenGGCM, BATS-R-US, and SWMF models, which are the three MHD magnetospheric models used in these experiments. Finally, a tool was needed that could load a large data set, plot all of it, and view planar cuts. The tool used for this was Paraview (*Paraview*, 2013) which is maintained by Kitware (*Kitware*, 2013), Paraview was specifically designed to enable 3-D visualization of scientific data and to handle very large data sets with parallelized operations. Paraview also has a Python interface, which allows plots to be made and manipulated via a script instead of manually using a graphical user interface.

The second tool was used for the *parameter variability - sensitivity validation* analysis (*Sargent*, 2004). This technique was implemented by inputting artificial data into magnetospheric MHD models, that are not in-situ based, in order to make controlled comparisons between model outputs. All of the data used as input into the models are of this form.

There are many magnetospheric models, and because the time required to make a comparison between them is prohibitive, and given the limitation of the Kameleon library, which at present only supports three magnetospheric MHD models, three MHD magnetospheric models were chosen for the experiments. To work around the limits of compiling and executing the models, the models were executed on computers at the CCMC.

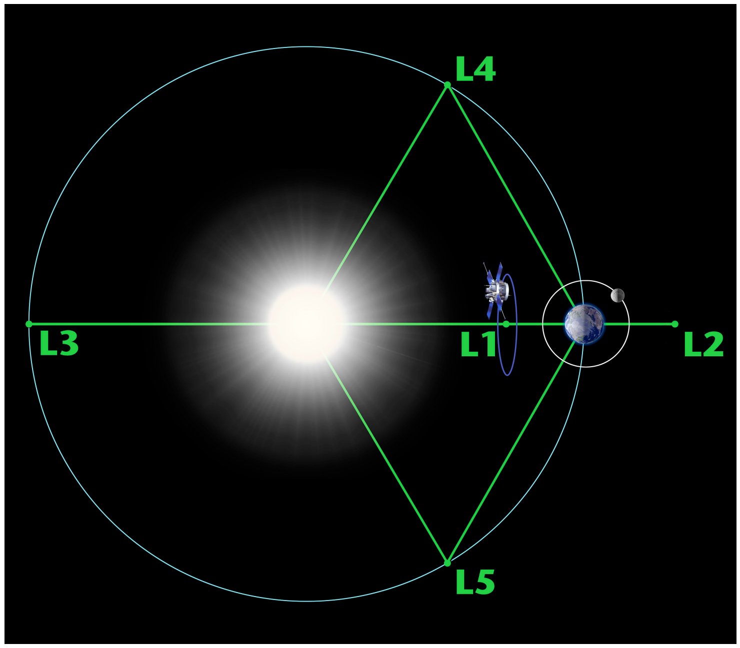

Figure 4.1: The five Lagrange points (from NASA, 2014).

Acquiring Data

The uniqueness to the *parameter variability* technique described previously is that the data used as inputs into the models are not in-situ measurements from the past, but are physically relevant artificial data that has meaning to the space weather community. The CCMC allows for model runs to be configured using a web interface; the run is submitted to staff who then execute the model with the selected inputs and configuration. The input parameters are submitted through a data file that contains values for $\mathbf{B}^{\mathbf{IMF}}$, $\mathbf{V}$, ρ, T. To determine the values to use as artificial inputs, Advanced Composition Explorer (ACE) measurements were used because they provide measurements from the solar wind taken from the L1 point ahead of Earth in the Sun-to-Earth line over a full solar cycle, as shown in Figure 4.1. The in-situ data that was measured by instruments on the ACE spacecraft were obtained from the OMNIWeb web site provided by the NASA Goddard Space Flight Center (OMNIWeb, 2013) between the dates of January 1st, 2000 to January 1st, 2011.

MATLAB was used to read in the OMNIWeb data files, and histograms were created for

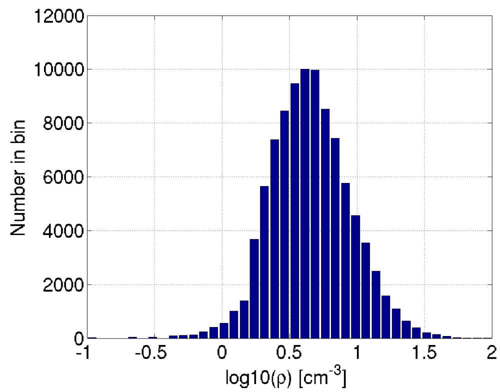

(a) Mean = 5.76 cm^{-3}, 80th and 20th Percentile = 11/2 cm^{-3}, 95,128 Measurements

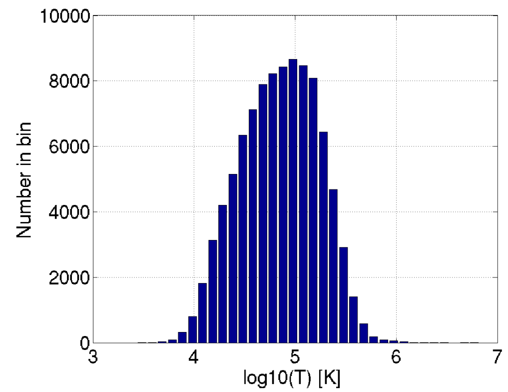

(b) Mean = 101289 K, 80th and 20th Percentile = 217139/20554 K, 95,255 Measurements

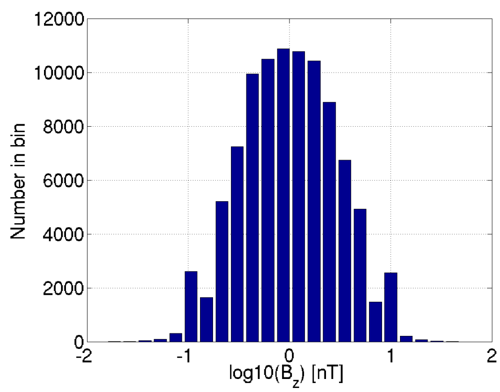

(c) Mean = 0.02 nT, 80th and 20th Percentile = 3.1/-3.0 nT, 96,417 Measurements

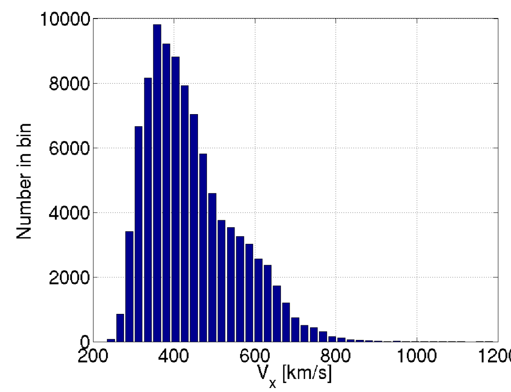

(d) Mean = 441.71 km/s, 80th and 20th Percentile = 604/320 km/s, 96,311 Measurements

Figure 4.2: Histogram of (a) ρ, (b) T, (c) B_z^{IMF} and (d) V_x values measured by ACE, from January 1st, 2000 to January 1st, 2011. These histograms were used to determine appropriate values as artificial inputs to the models.

Table 4.1: ACE solar wind measurement histograms

Variable	**20th Percentile**	**Mean**	**80th Percentile**
ρ $[cm^{-3}]$	2	5.76	11
T $[K]$	20554	101289	217139
V_x $[km/s]$	310	442	604
B_z $[nT]$	-3.0	0.02	3.1

Table 4.2: Input parameters for B_z^{IMF} reversal experiment

ρ $[cm^{-3}]$	T $[K]$	V_x $[km/s]$	B_z $[nT]$
5.76	101289	-442	+3.1 to -3.0 at 00:30

the solar wind variables. Figure 4.2(a) is the histogram of solar wind plasma density. The mean is 5.76 $[cm^{-3}]$, the 80th percentile is 11 $[cm^{-3}]$, and the 20th percentile is 2 $[cm^{-3}]$. Figure 4.2(b) is the histogram of solar wind temperature. The mean is 101289 $[K]$, the 80th percentile is 217139 $[K]$ and the 20th percentile is 20554 $[K]$. Figure 4.2(c) is the histogram of the solar wind interplanetary magnetic field. The mean is 0.02 $[nT]$, the 80th percentile is 3.1 $[nT]$ and the 20th percentile is -3.0 $[nT]$. Figure 4.2(d) is the histogram of solar wind velocity in the x direction, from Earth towards the Sun. The mean is 442 $[km/s]$, the 80th percentile is 604 $[km/s]$ and the 20th percentile is 310 $[km/s]$. The 20th and 80th percentiles were used for consistency with climatological values from in-situ data, specifically for the experiment studying the effects of extreme solar wind conditions on the magnetosphere, higher and lower values for input conditions are required to simulate high and low compression. The percentile and mean values for each variable are displayed in Table 4.1.

The simulations analyzed in this section used the input values shown in Table 4.2.

4.1.4 Results

There are two different time periods in each run where the overall state of the magnetosphere will significantly differ. First, the period of time before the B_z^{IMF} reversal occurs in which the magnetic field of the IMF is the same direction as Earth's. Second, the period of time after the B_z^{IMF} reversal in which the direction of the IMF is opposite to that of Earth's. The reversal in B_z^{IMF} occurs 30 minutes into each run, the total time for each run was 6 hours. The changes expected are only due to a reversal in B_z^{IMF} direction and the differences between each model.

The grid used in the OpenGGCM model is different than that used in the BATS-R-US and SWMF models. The stretched cartesian grid used in the OpenGGCM model has high resolutions in the entire current sheet region and high resolutions near-Earth extending in the Z and Y directions from the origin. The SAMR grid used in the BATS-R-US and SWMF models has high resolution near-Earth and in the near-Earth current sheet region with lower resolutions in the distant tail and distant northern and southern tail lobes.

There are differences in how each model treats magnetospheric conditions near-Earth (within $10R_E$). The OpenGGCM and BATS-R-US models do not account for particle drifts associated with the ring current. The SWMF model accounts for particle drifts and the ring current.

The differences between the BATS-R-US and SWMF models are expected to be due to the ring current. Based on Ampere's law, $\nabla \times \mathbf{B} = \mu_0 \mathbf{J}$, the additions of a ring current should lead to an increase of the z component of the magnetic field on the sunward side of the ring current and decrease the z component of the magnetic field on the tailward side of the ring current. This means the magnetic pressure is expected to be larger in the sunward side of the ring current and smaller in the tailward side of the ring current.

The magnetic pressure at the dayside magnetopause is effected by the reversal from a positive B_z^{IMF} direction to a negative B_z^{IMF} direction. A decrease in the magnetic pressure at that location will cause a movement of the magnetopause towards Earth.

Figure 4.3 shows the OpenGGCM model output during the timeframe where the magnetopause moves Earthward due to a reduction in magnetic pressure, consistent with expectations.

To better understand the differences in the position of the magnetopause between the three models before and after the B_z^{IMF} reversal, model output difference images are used.

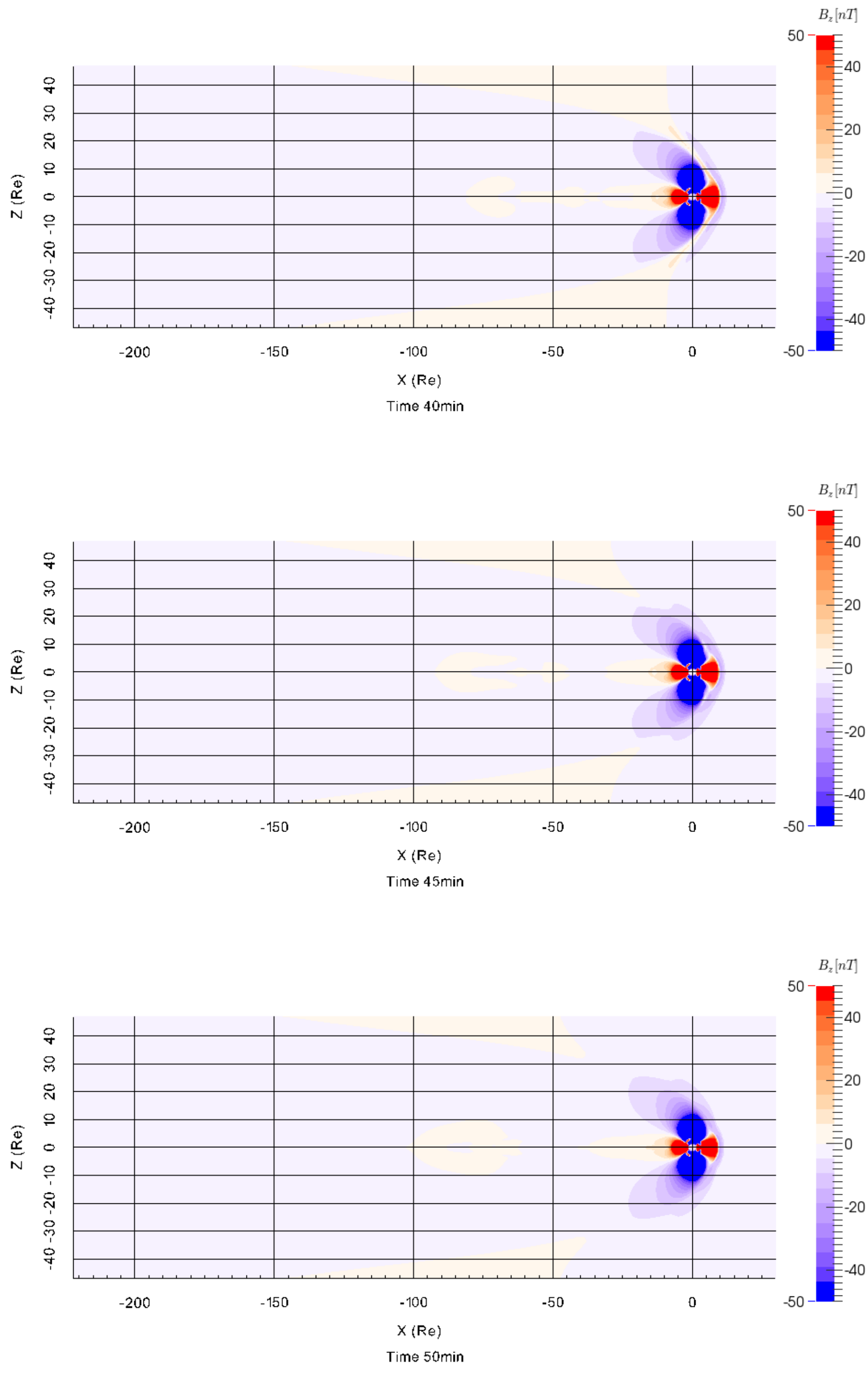

Figure 4.3: OpenGGCM B_z output shortly after the B_z^{IMF} reversal.

Figure 4.4 shows three comparisons between two models at a time. The top image is a percent difference of B_z between the OpenGGCM and BATS-R-US models; the BATS-R-US model values are subtracted from the OpenGGCM model values for each grid point on the interpolated grid and that result is divided by their mean at that grid point. The middle image is a percent difference of B_z between the OpenGGCM and SWMF models. The bottom image is a percent difference of B_z between the BATS-R-US and SWMF models. The top image of Figure 4.4 shows large and negative percent differences near the location of the magnetopause. The negative value means that the second model in the top image, BATS-R-US, has higher values. From this type of information, the model with the farthest and closest magnetopause can be determined. Before the B_z^{IMF} reversal the OpenGGCM model magnetopause is closest to Earth and the SWMF model magnetopause is farthest from Earth.

The SWMF model has a slightly higher magnetic pressure near the magnetopause in comparison to the BATS-R-US model, which can be explained by the effect that the ring current has locally. The differences in current strength before the B_z^{IMF} reversal are shown in Figure 4.5, where comparing the top (BATS-R-US) and bottom (SWMF) images, the tail currents are lower with the SWMF model. Earth has a ring current brought about by the motions of plasma trapped in the near-Earth magnetosphere. This current, which lies between 4-7 R_E, induces its own magnetic field. The direction of its magnetic field in the near-Earth tail region opposes the direction of the field created by the current sheet current, weakening it near-Earth. The direction of B_z from the ring current near the magnetopause is the same as the direction of Earth's magnetic field and thus increases the magnetic pressure in that location. That increase in magnetic pressure explains why the SWMF model magnetopause is farthest from Earth, as shown in Figure 4.4.

Figure 4.6, 60 minutes after the B_z^{IMF} reversal, shows that under negative B_z^{IMF} conditions, the OpenGGCM model magnetopause is closest to Earth and the BATS-R-US magnetopause is farthest from Earth.

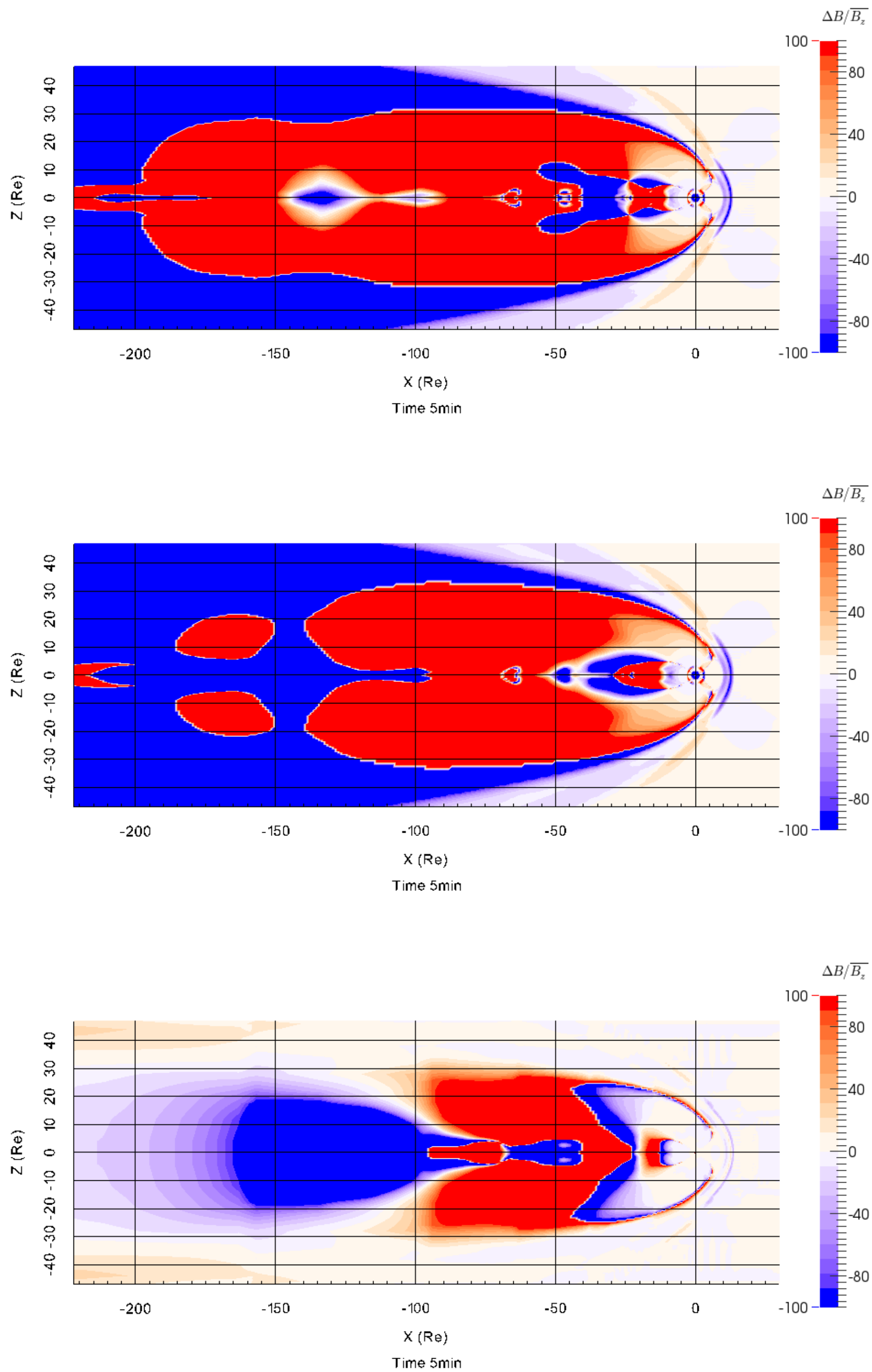

Figure 4.4: B_z percent differences between the OpenGGCM and BATS-R-US models (top), the OpenGGCM and SWMF models (middle), and the BATS-R-US and SWMF models (bottom) 25 minutes before the B_z^{IMF} reversal.

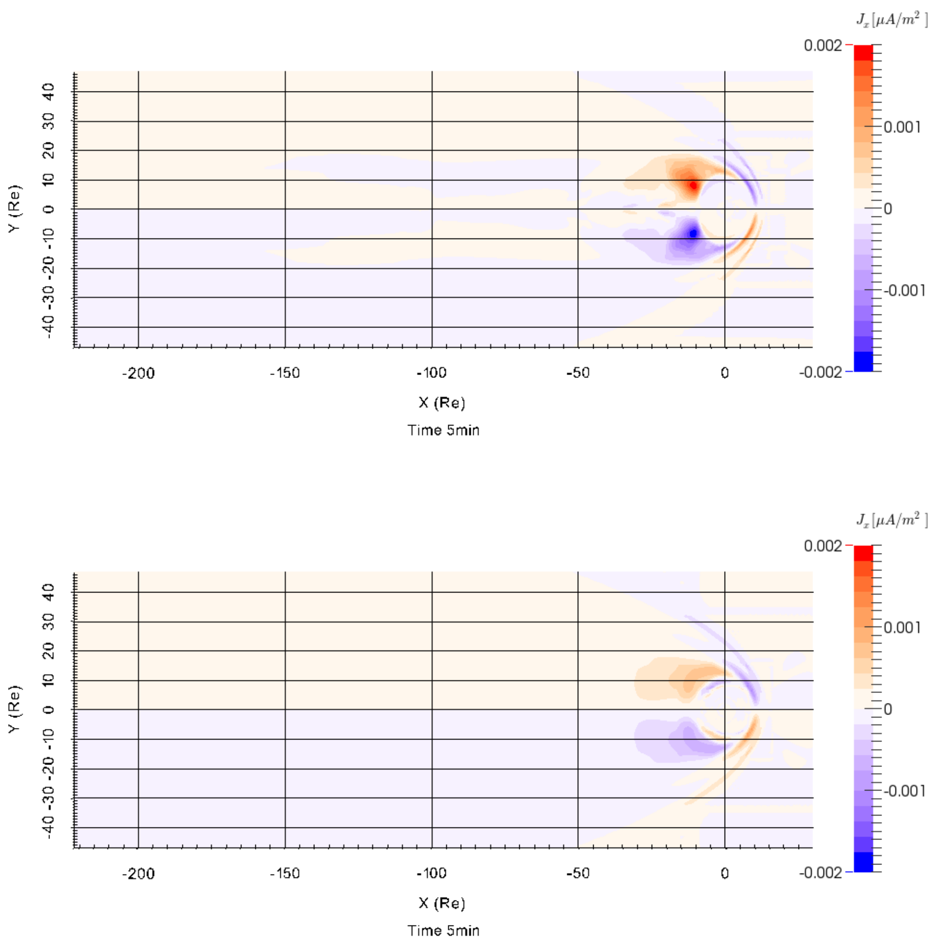

Figure 4.5: J_x for BATS-R-US (top) and SWMF (bottom).

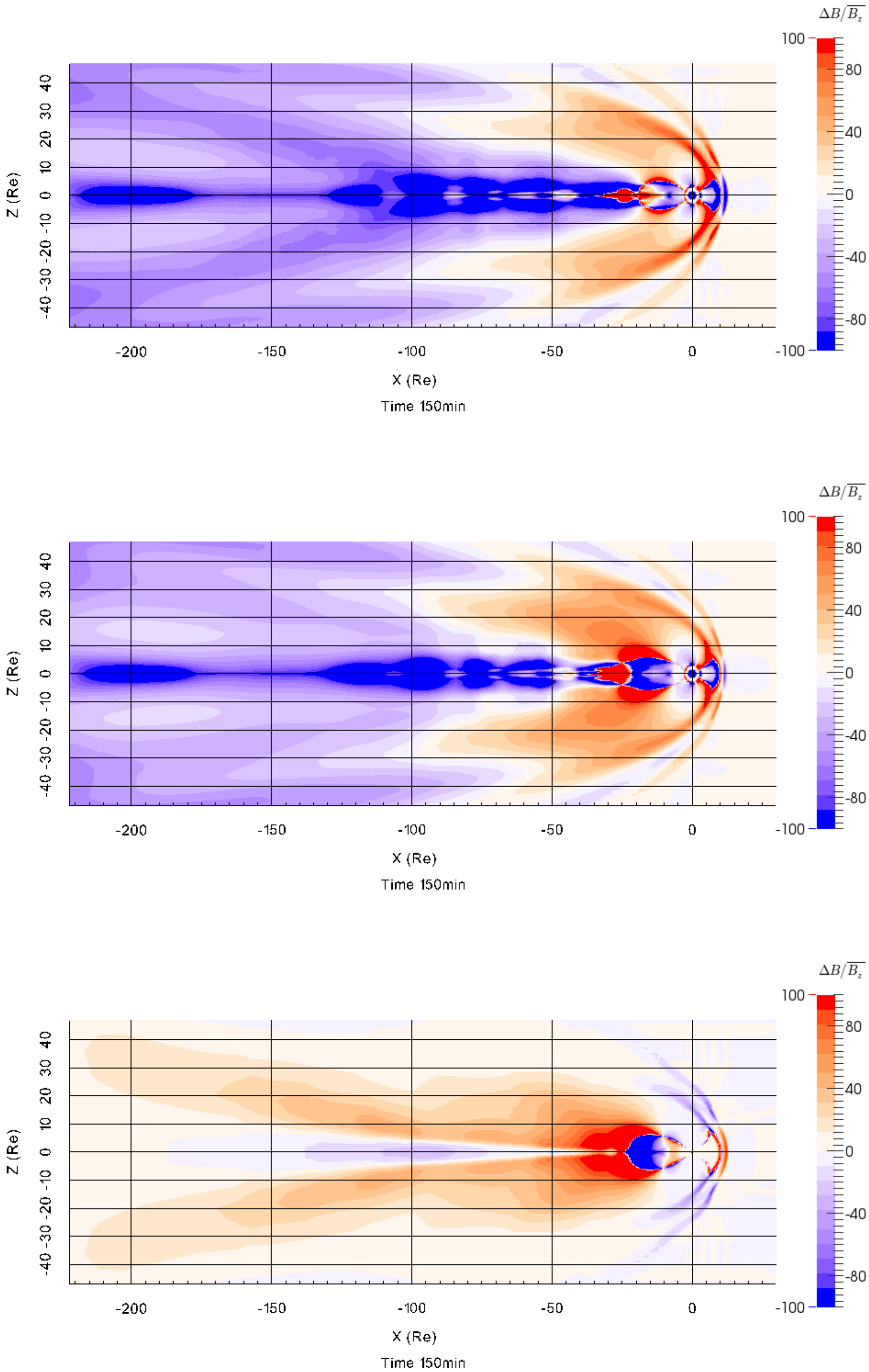

Figure 4.6: B_z Percent differences between the OpenGGCM and BATS-R-US models (top), the OpenGGCM and SWMF models (middle), and the BATS-R-US and SWMF models (bottom) 60 minutes after the B_z^{IMF} reversal.

When plasma from the sun traveling at supersonic speeds interacts with the magnetosphere, it eventually slows down below the speed of sound. This transition from supersonic to subsonic causes a shock region ahead of the magnetosphere, which is referred to as the bow shock. The velocity of the plasma continues to decrease as it compresses and heats, leading to higher densities between the magnetopause and the bow shock. Figure 4.7 shows this for all three models. There are higher densities in the current sheet that are typically on the order of 0.1 to 1 cm^{-3}, but these values fit in one color bin of the plots and are not visible.

Through various mechanisms, plasma can enter the magnetosphere cavity. Some of this plasma becomes trapped on the closed magnetic field lines that surround Earth resulting in higher near-Earth densities. The differences in densities seen near-Earth and in the tail region between the models before the B_z^{IMF} reversal are shown in Figure 4.8. The larger differences seen in the magnetotail when comparing the OpenGGCM model with the SWMF model is due to the OpenGGCM model not accounting for the ring current. This plot also shows that the SWMF model has highest densities in the current sheet region.

After the B_z^{IMF} reversal, shown in Figure 4.9, the OpenGGCM densities in the distant current sheet become higher than the BATS-R-US. The SWMF model still has higher densities in the current sheet, which is shown in the third image that compares the BATS-R-US and SWMF models (where there are darker blue colors in the current sheet).

As noted previously, and shown in Figure 4.10, the solar wind U_x slows down from a supersonic to a subsonic speed which causes a shock. U_x is then reduced more as its distance from Earth decreases. The current sheet is formed from two opposing magnetic field directions close to one another, which is caused by the stretching in the magnetotail. In this region there is a near-zero B_z, which allows for reconnection. This reconnection transports particles in the current sheet region both tailward and Earthward. The velocities seen in the current sheet region in all models are consistent with this.

Before the B_z^{IMF} reversal, Figure 4.11 shows that the OpenGGCM model has higher U_x in the distant tail current sheet compared to the BATS-R-US model and the SWMF model.

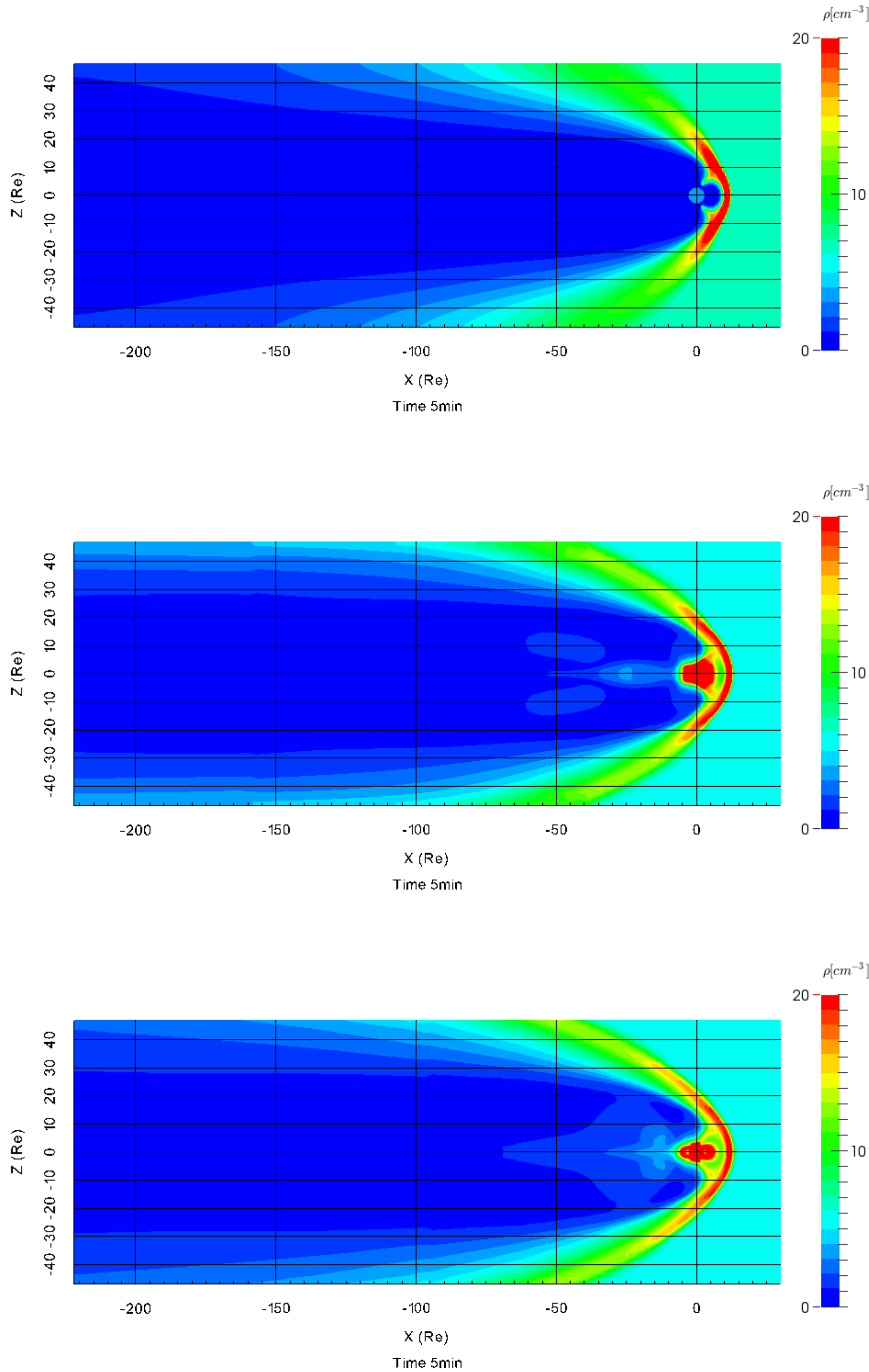

Figure 4.7: ρ for OpenGGCM (top) , BATS-R-US (middle), and SWMF (bottom) 25 minutes before the B_z^{IMF} reversal.

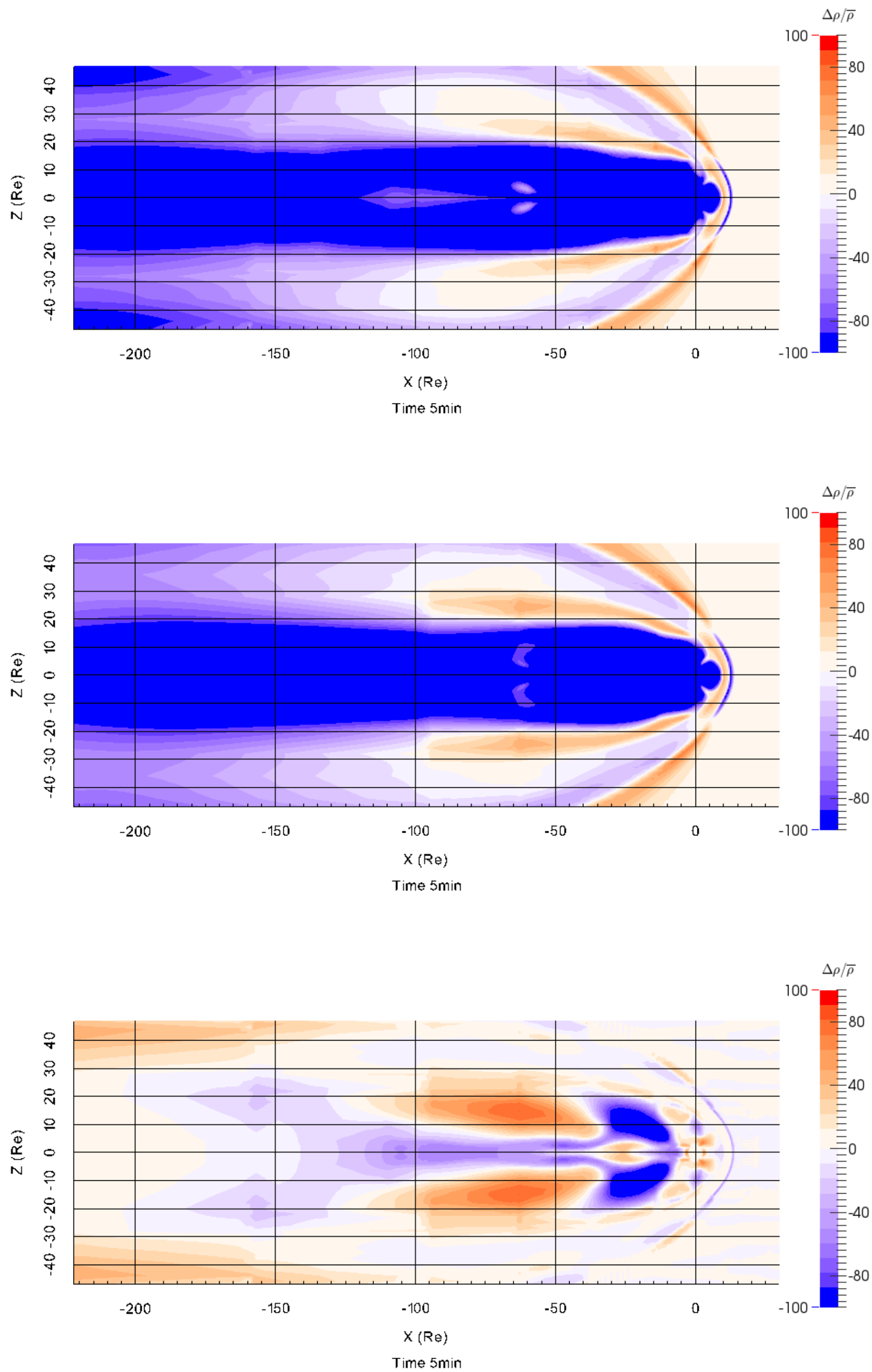

Figure 4.8: ρ Percent differences between the OpenGGCM and the BATS-R-US models (top), the OpenGGCM and SWMF models (middle), and the BATS-R-US and SWMF models (bottom) 25 minutes before the B_z^{IMF} reversal.

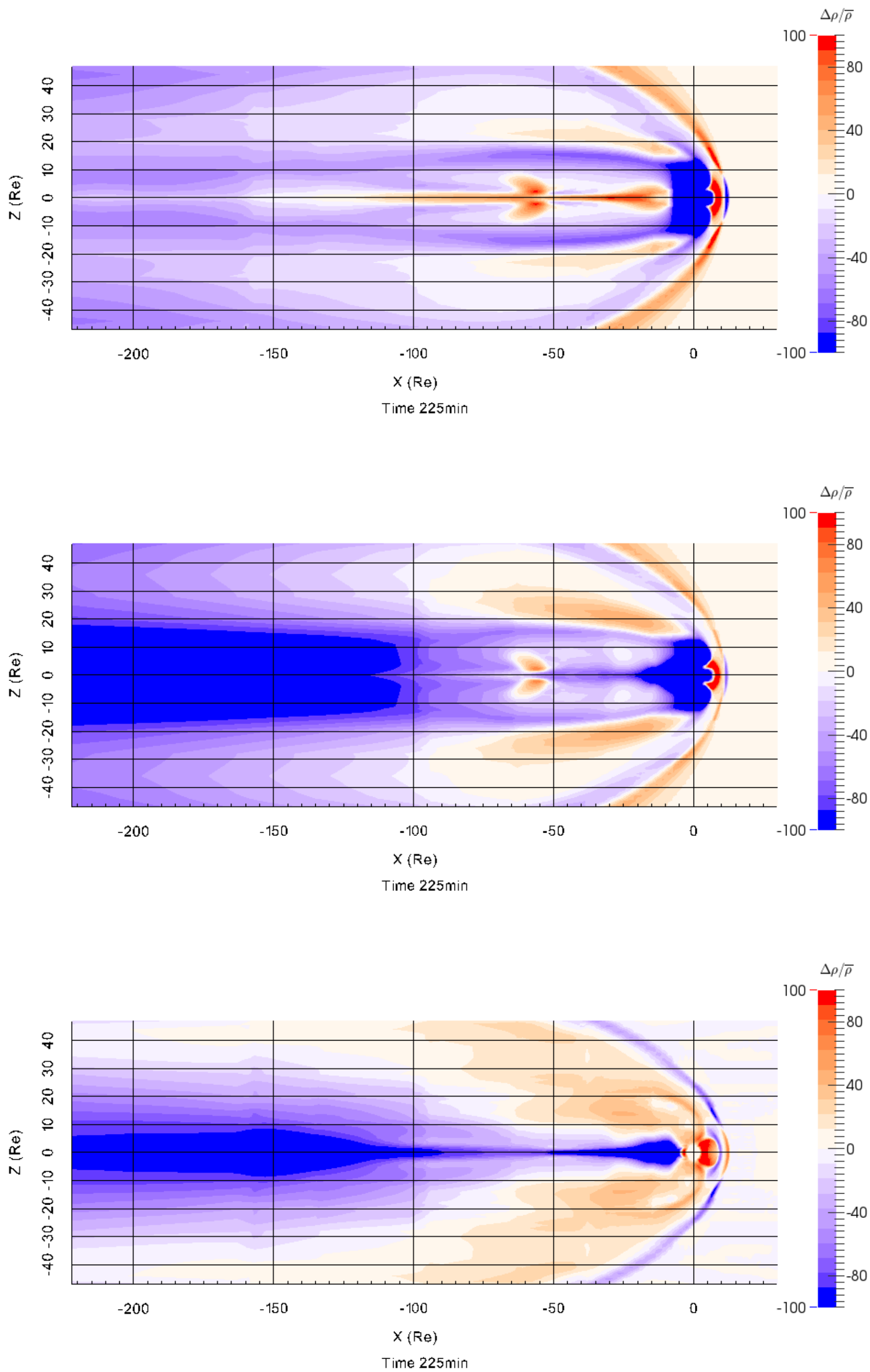

Figure 4.9: ρ Percent differences between the OpenGGCM and BATS-R-US models (top), the OpenGGCM and SWMF models (middle), and the BATS-R-US and SWMF models (bottom) 115 minutes after the B_z^{IMF} reversal.

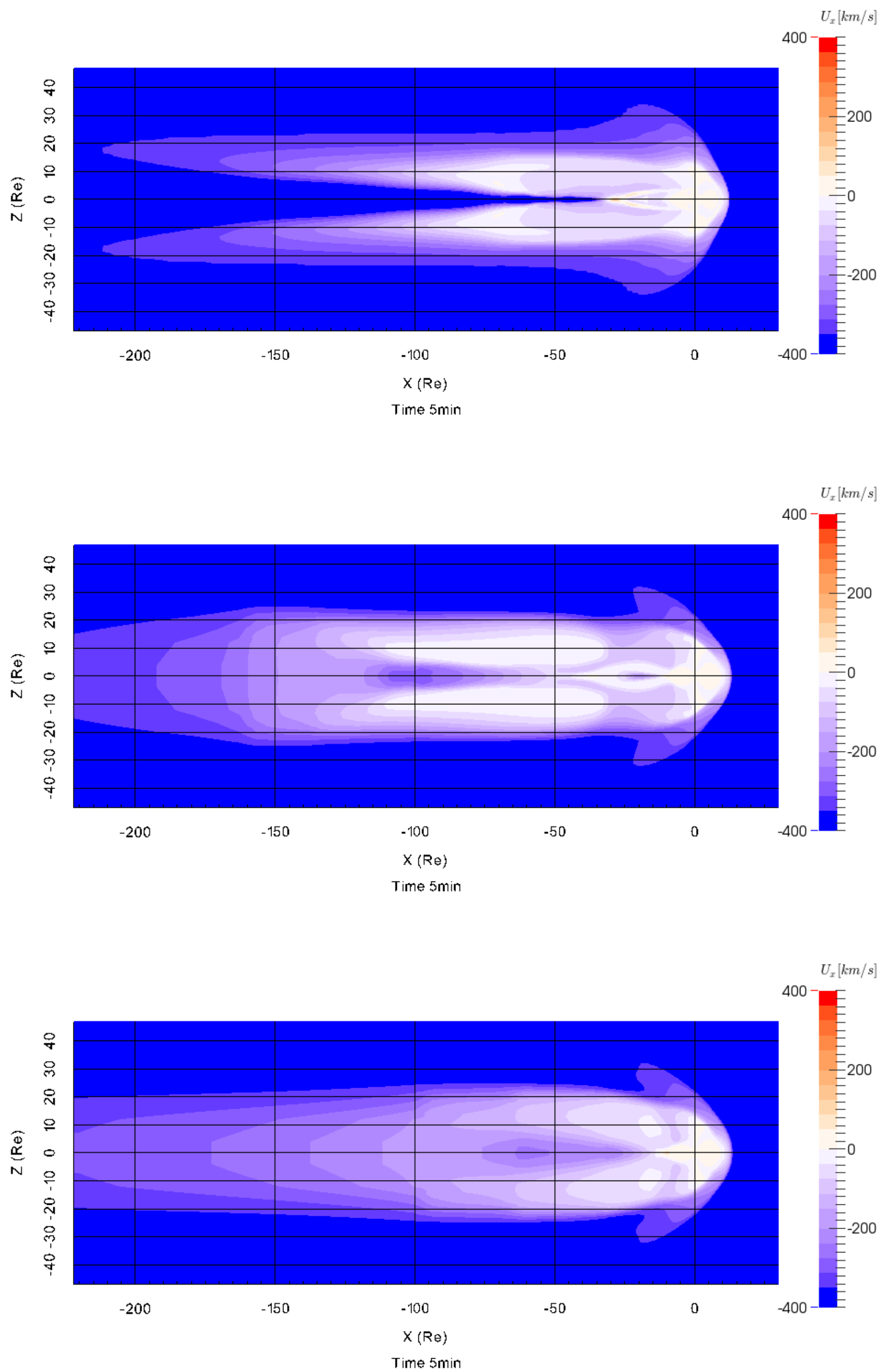

Figure 4.10: U_x for OpenGGCM (top), BATS-R-US (middle), and SWMF (bottom) 25 minutes before the B_z^{IMF} reversal.

The near-Earth current sheet velocities are higher in the BATS-R-US model and the SWMF model than the OpenGGCM model. In comparison, the BATS-R-US model and the SWMF model comparison (bottom), shows that the SWMF model has higher U_x in the near-Earth current sheet and the BATS-R-US model has higher U_x in the distant tail.

After the B_z^{IMF} reversal, Figure 4.12 shows the BATS-R-US model has higher U_x compared to the OpenGGCM model in the current sheet region (top), while the OpenGGCM model compared to the SWMF model (middle) shows higher U_x in the current sheet region for the OpenGGCM model and higher U_x in the north and south tail lobes outside of the current sheet region for the SWMF model. Comparing the BATS-R-US model and the SWMF model (bottom), the BATS-R-US model has higher U_x in the current sheet region.

4.1.5 Discussion and Conclusions

The position of the magnetopause and shape of the magnetosphere are determined by the magnetic field of Earth and its interaction with the solar wind. The OpenGGCM model, which did not account for a near-Earth ring-current, has the weakest magnetic pressure and therefore the closest magnetopause to Earth of the three models. The model-predicted position of the magnetopause is important for forecasters because they need to be able to tell companies with space-based technologies, especially those in geosynchronous orbit, if their equipment may be effected by the plasma that comes from the solar wind.

Garcia and Hughes (2007) discuss how the absence of the ring current in the Lyon Fedder Mobarry (LFM) magnetospheric model compares to magnetopause location measurements made by satellites. They found that an insufficient ring current would not push the magnetopause far enough Sunward. The ring current effect on the magnetopause location is evident with this experiment as well.

The models show the slowdown of U_x Earthward of the bow shock, and inside the magnetosphere. The velocities in the current sheet region are important to forecasters as to the timing of storms impacts seen at Earth. Reconnection is tied to the U_x such that a faster reconnection will yield faster velocities and a slower reconnection will yield slower velocities.

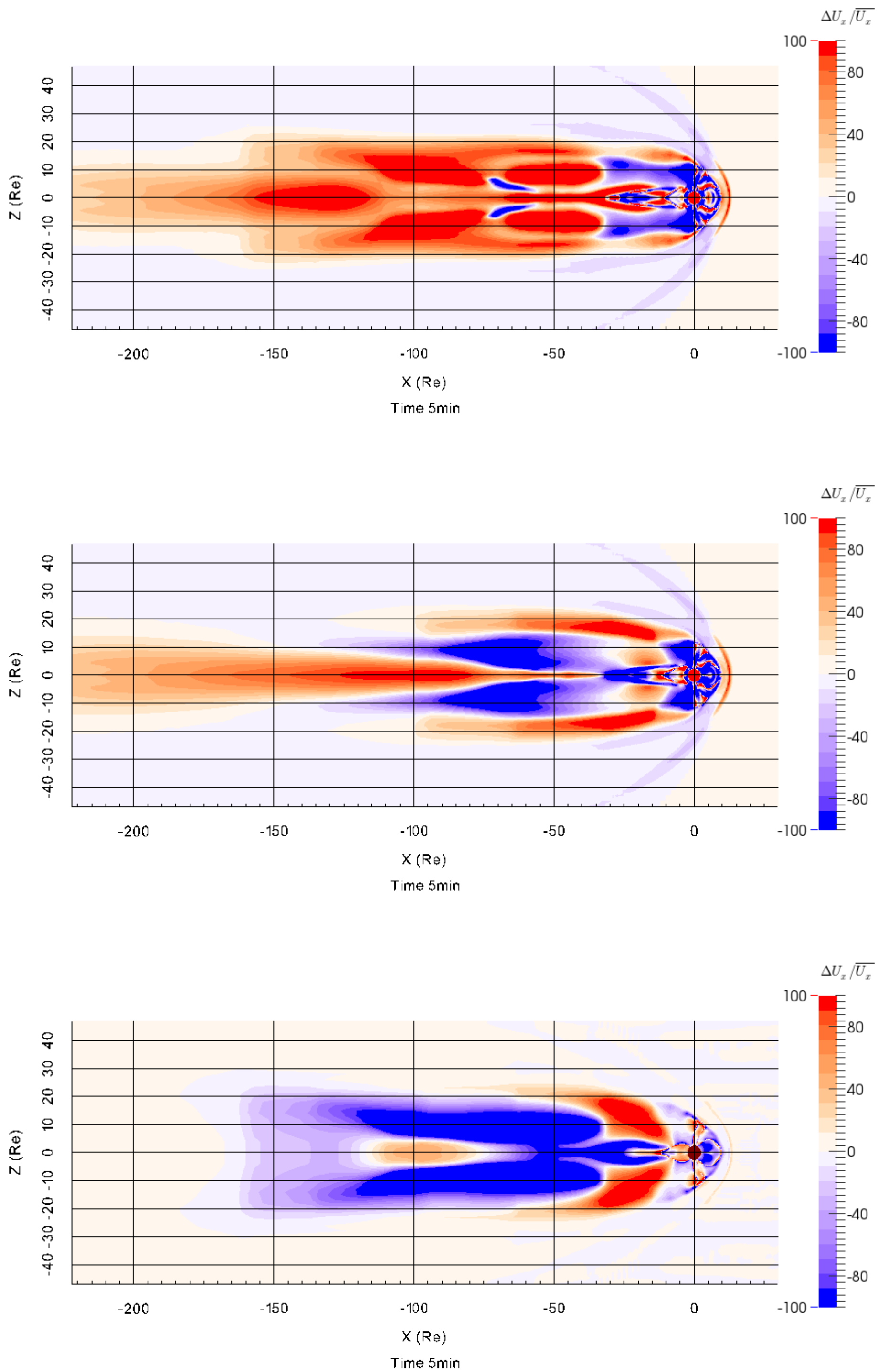

Figure 4.11: U_x percent differences between OpenGGCM and BATS-R-US (top), OpenGGCM and SWMF (middle), and BATS-R-US and SWMF (bottom) 25 minutes before the B_z^{IMF} reversal.

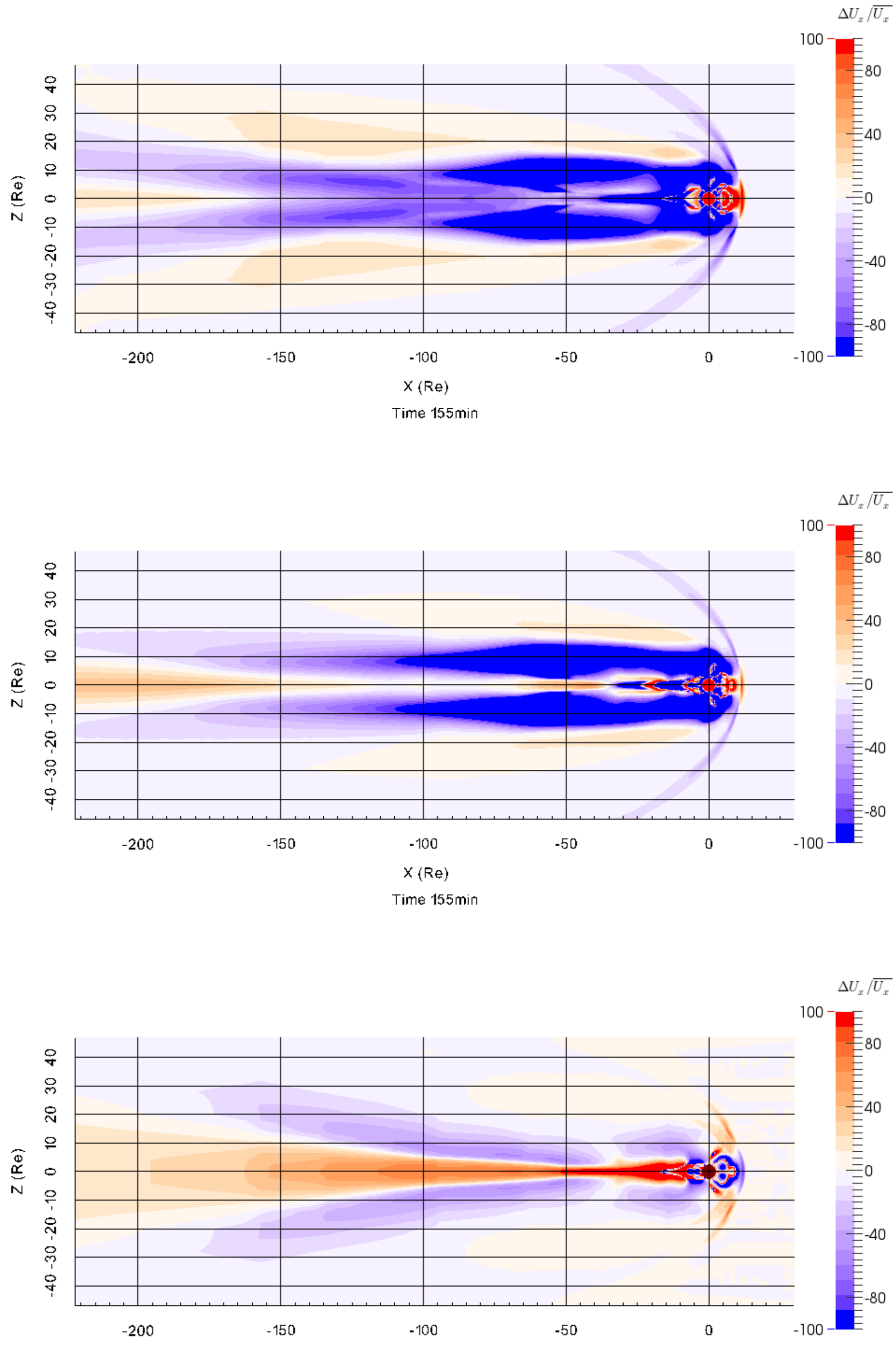

Figure 4.12: U_x percent differences between OpenGGCM and BATS-R-US (top), OpenGGCM and SWMF (middle), and BATS-R-US and SWMF (bottom) 85 minutes after the B_z^{IMF} reversal.

Model output differences can give model developers a better view of the differences between their model and other models for similar regions in space. With model runs involving in-situ data, the space weather community is already doing a lot of analysis into determining which model is better for select events.

Summary

For a reversal in B_z^{IMF}, the following occur in the models:

- The OpenGGCM model magnetopause is closest to Earth as it has the weakest near-Earth magnetic pressure.
- Under positive B_z^{IMF} conditions, the ring current pushes the SWMF model magnetopause farther sunward than that in the BATS-R-US model.
- Under negative B_z^{IMF} conditions, the SWMF model magnetopause is farther Earthward than that in the BATS-R-US model.
- The differences in magnetopause positions between BATS-R-US and SWMF are due to the effects of the ring current addition to the SWMF model.
- Densities are highest with the SWMF model and lowest with the OpenGGCM model.
- The OpenGGCM model tail currents are significantly different from the BATS-R-US model and SWMF at over 100 percent differences.

4.2 The influence of preconditioning on MHD magnetospheric models

This section addresses the influence of the amount of time spent on preconditioning on magnetospheric MHD models. There are examples of previous research dealing with magnetospheric preconditioning as described in the following section, but the term preconditioning used here has a slightly different meaning as described previously in Section 2.3.3. In order to perform a *parameter variability - sensitivity validation*, it is necessary to be able to control input into the model, and for consistency, there is a necessity to keep as many of the inputs constant.

4.2.1 Background

Lavraud et al. (2006) performed a study on the state of the magnetosphere for a subset of coronal mass ejection and co-rotating interaction region events and looked to identify if there was a preconditioning effect for sustained northward interplanetary magnetic fields (IMF). The study aimed to test a hypothesis that a cold dense plasma sheet prior to storm initiation, which is known to enhance the ring current, is caused by a sustained northward IMF. The enhancement of the ring current would lead to lower storm-time D_{st} values. Measured and modeled D_{st} values were compared with that of a semi-empirical D_{st} model. The modeled D_{st} tended to underestimate the actual measured D_{st} during events where there was a sustained northward IMF before the start of a storm. Plasma data from Los Alamos satellites were consistent with a colder and denser plasma sheet being present for the events in which a sustained northward IMF was present prior to storm initiation. A follow up study by *Weigel* (2010) showed that there was no statistically significant preconditioning effect as claimed.

Juusola et al. (2013) considered how the ring current plays a role in steady magnetospheric convection (SMC). SMC occurs when there is a balance of reconnection rates on the dayside and in the distant tail region. This study showed that the ring current strength needed to be at a specific level, no higher and no lower, in order for SMC to occur. Through a study of B_z^{IMF} and V_x along with the SYM-H index, *Juusola et al.* (2013) determined that most SMC events are preconditioned with low V_x and a slightly negative B_z^{IMF}, which provides energy to the ring current and prevents bursty convection from occurring, thus allowing a continuous SMC event.

4.2.2 Motivation

The preconditioning described by *Lavraud et al.* (2006) involved the condition of the magnetosphere prior to a storm that would cause lower D_{st} values during the storm. The preconditioning described by *Juusola et al.* (2013) uses the term preconditioning as a set of specific conditions that must be met in order for SMC events to occur. The term preconditioning used in these papers involves an actual state that the magnetosphere needs to be in at or prior to an event. Magnetospheric models are started with artificial initial conditions and then run for a certain amount of time prior to actual or user provided data being used as boundary conditions. The preconditioning considered in this thesis involves the amount of time between the start of the run and the time of an event versus the state of the solar wind or magnetospheric variables prior to an event.

According to *Raeder* (2003) and *Buchner et al.* (2003), the magnetosphere will form within one hour from the start of preconditioning in a MHD simulation. According to *Raeder* (1999), the initial conditions for the OpenGGCM model magnetic field are started from the superposition of Earth's dipole with a mirror dipole that is equally as strong, such that B_x is zero in the $x = 16R_E$ plane. Sunward of $x = 16R_E$, the B field in this plane is replaced by the initial solar wind field and the run is started. *Buchner et al.* (2003) presented a question to the community when discussing the length of preconditioning time used in magnetospheric MHD models and noted that because the magnetosphere has a long memory from previous conditions, it may take a few hours of preconditioning time to stabilize the magnetosphere. However, there has been no published research on the appropriate amount of time or the influence of the preconditioning time on model predictions.

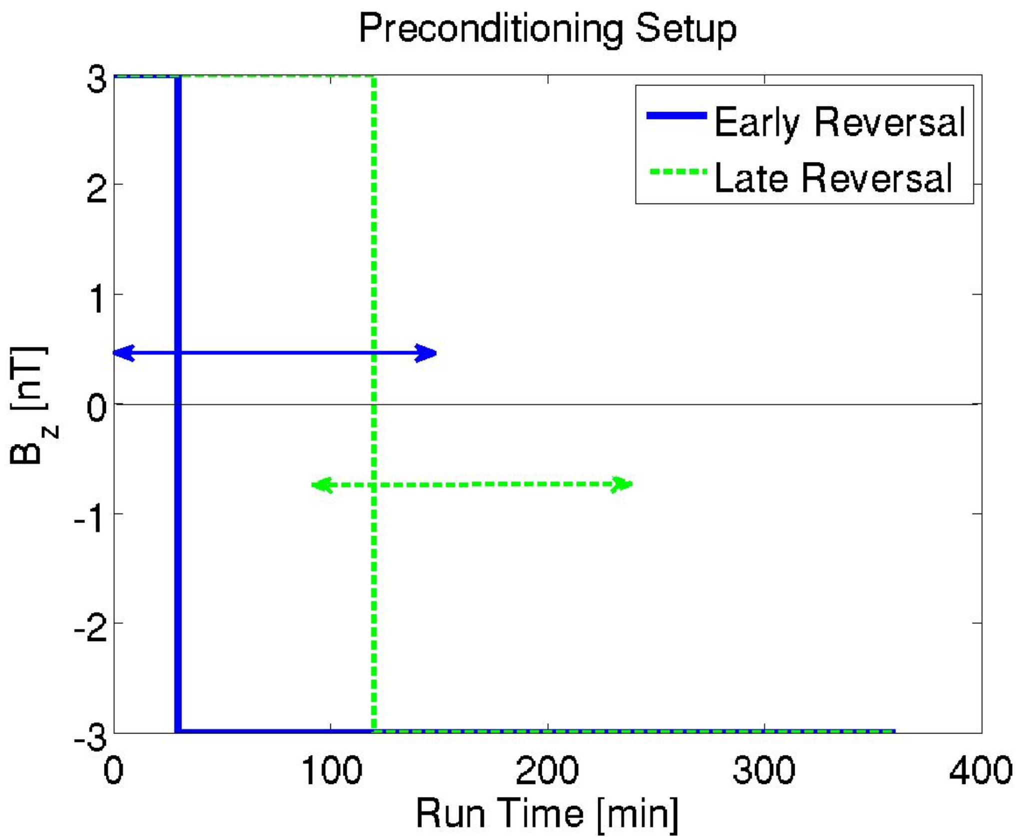

Figure 4.13: Setup for the preconditioning experiment. Two equal length time intervals from each run with the reversal starting at 30 minutes into the start of the interval.

4.2.3 Methodology

The methodology used in this section is similar to the methodology for the B_z^{IMF} reversal experiment described in section 4.1.3.

To evaluate the differences between the two models with a time-shifted B_z^{IMF} reversal, the output data from the two models were taken between 30 minutes before the reversal to 2 hours after the reversal, as shown in Figure 4.13, and then inserted into the code that creates the difference output, which was then processed by a Paraview Python code that creates images.

As shown in Table 4.3 for run 1, T, U_x, and ρ were kept constant throughout the entire run. The only difference between the two runs is the time at which B_z^{IMF} was reversed from

Table 4.3: Input parameters for preconditioning experiment

Run Num.	ρ $[cm^{-3}]$	T $[K]$	U_x $[km/s]$	B_z $[nT]$
1	5.76	101289	-442	+3.1 to -3.0 at 00:30
2	5.76	101289	-442	+3.1 to -3.0 at 02:00

a positive to negative value. This is physically meaningful as a B_z^{IMF} reversal is a typical cause for enhanced magnetospheric activity.

4.2.4 Results

In Figure 4.14, the top comparison is between the early and late reversal runs for the OpenGGCM model. Red indicates locations where the early reversal has higher values, while blue indicates locations where the late reversal has higher values. The OpenGGCM model B_z output shows differences in the positioning of the entire magnetopause with the late reversal having a magnetopause that is farther Sunward. There are also differences in the current sheet region with neither the early or late reversal showing consistently higher or lower values in one specific region of the current sheet. The BATS-R-US and SWMF models show differences in the current sheet region between $\pm$ 20 R_E in the z direction.

After the B_z^{IMF} reversal, towards the end of the run, there are still differences in the OpenGGCM model (top) run, while there are minimal to no differences in the BATS-R-US model (middle) and the SWMF model (bottom) run, as shown in Figure 4.15. The differences shown for the OpenGGCM model have decreased near the magnetopause, but are still large in the current sheet region.

In Figure 4.16, the largest differences occur in the current sheet regions. The OpenGGCM model differences do not extend far tailward within ± 10 R_E in the z direction. The differences in both the BATS-R-US and SWMF models are highest in the current sheet region and extend into the distant tail within ± 20 R_E in the z direction. In the BATS-R-US model runs, the early reversal has higher values in the near-Earth current sheet region. In the SWMF model, the early reversal has higher values nearest Earth outside of the current sheet region. There are lower values for the late reversal in the distant tail region.

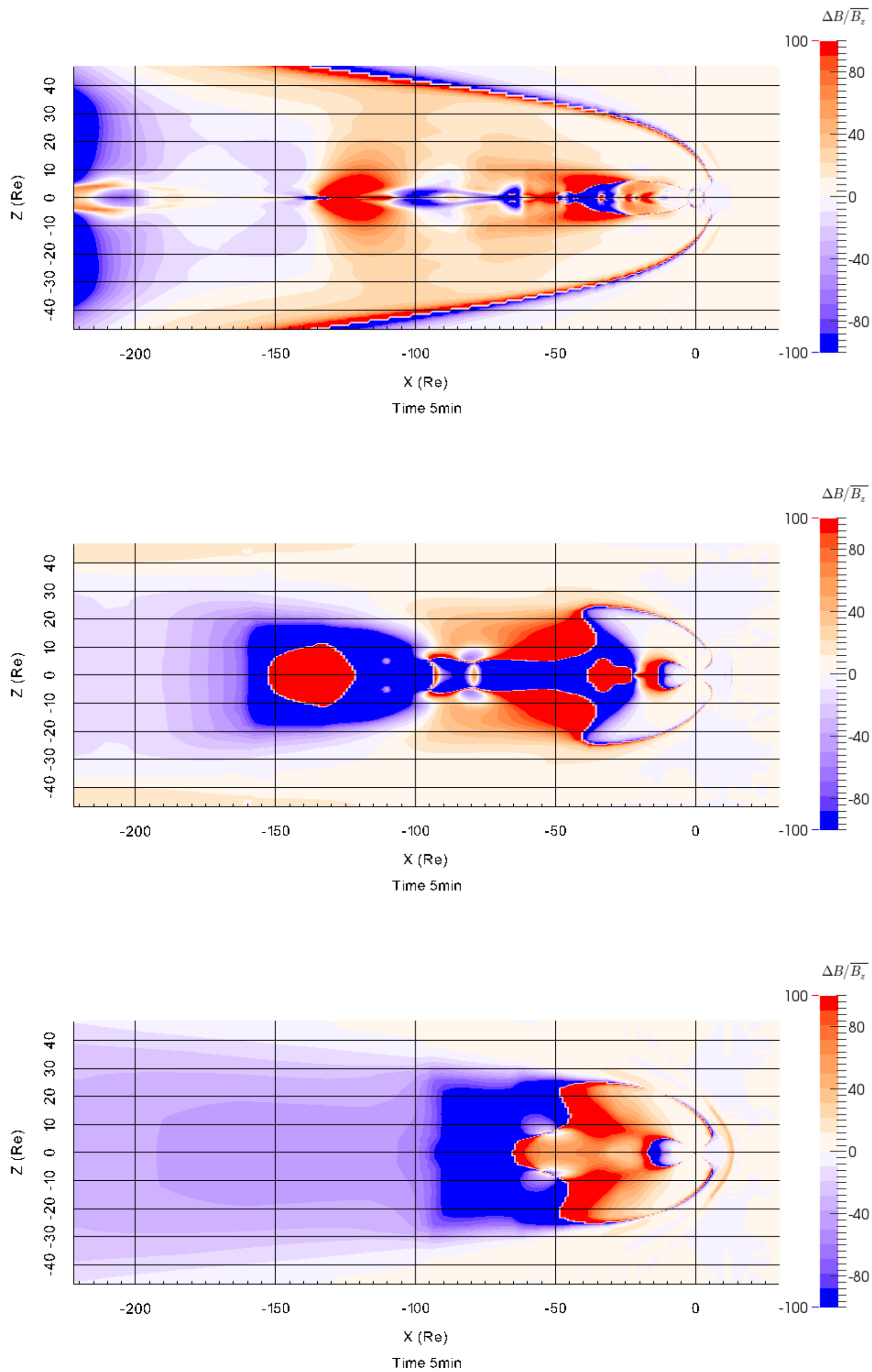

Figure 4.14: B_z percent differences between the OpenGGCM model early and late reversals (top), BATS-R-US early and late reversals (middle), and SWMF early and late reversals (bottom) 25 minutes before the B_z^{IMF} reversal.

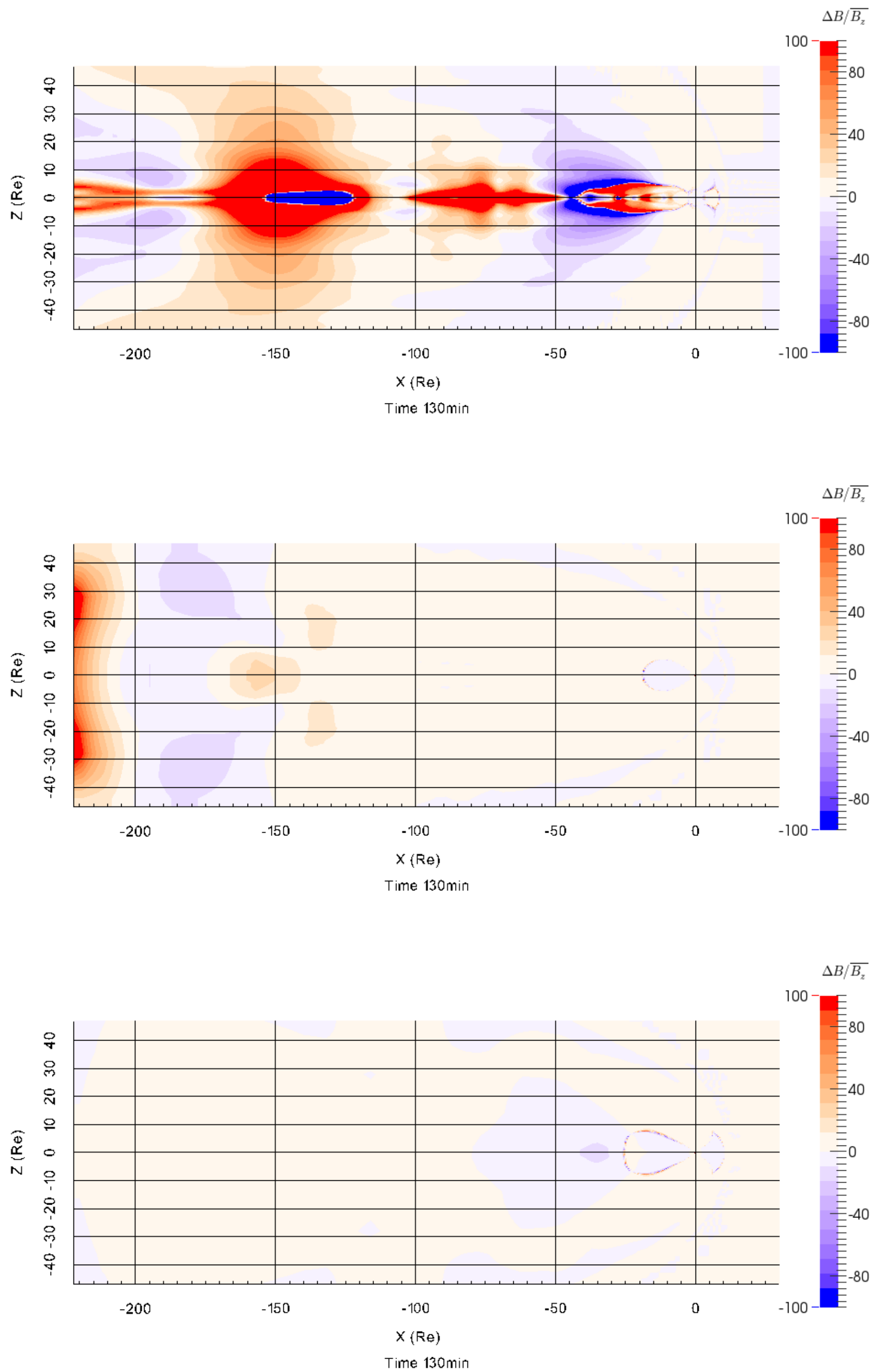

Figure 4.15: B_z percent differences between the OpenGGCM model early and late reversals (top), BATS-R-US early and late reversals (middle), and SWMF early and late reversals (bottom) 60 minutes after the B_z^{IMF} reversal.

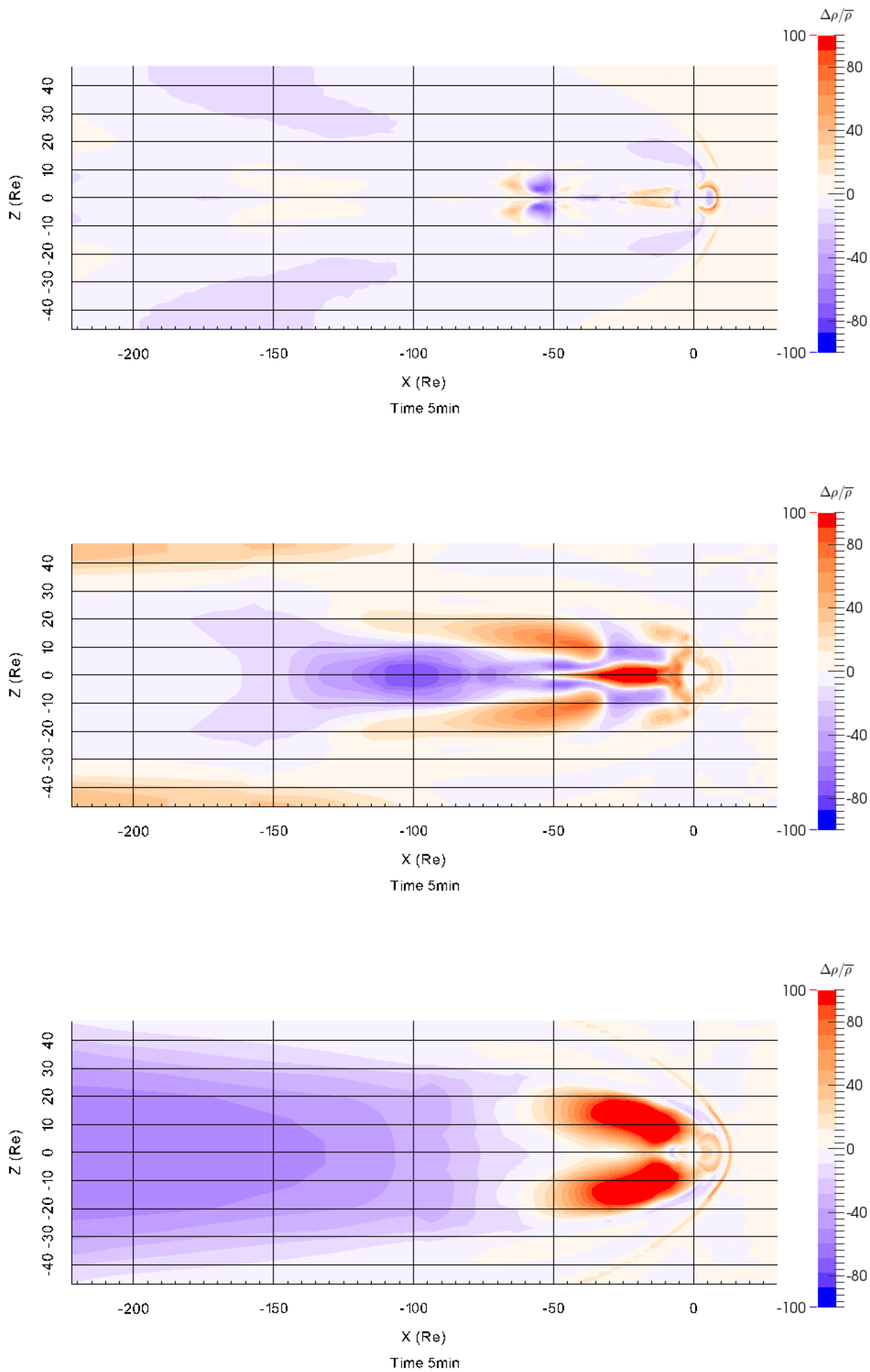

Figure 4.16: ρ percent differences between the OpenGGCM model early and late reversals (top), BATS-R-US early and late reversals (middle), and SWMF early and late reversals (bottom) 25 minutes before the B_z^{IMF} reversal.

After the B_z^{IMF} reversal, as shown in Figure 4.17, there are only small regions of differences in the OpenGGCM model (top). The SWMF model (bottom), and the BATS-R-US model (middle), have near zero differences.

The U_x plots in Figure 4.18 show the highest differences in the current sheet region for all three models. No one run has higher differences in which the opposite run does not. The regions in which one run has higher values over the other is not consistent. The BATS-R-US model (middle) late reversal has highest values in the current sheet region. The SWMF model (bottom) has highest differences with the late reversal run in the north and south hemispheres of the magnetosphere outside of the current sheet region and far from Earth, while the early reversal has higher values close to Earth.

After the B_z^{IMF} reversal, as shown in Figure 4.19, most of the OpenGGCM model (top) differences are in the current sheet region. The early reversal has higher values tailward of -40R_E, while the late reversal has higher values Earthward of -40R_E.

4.2.5 Discussion and Conclusions

The differences in the magnetopause position, for all three models, are of concern to forecasters. If there is any risk of the magnetopause traveling farther towards Earth than geosynchronous orbit, then the companies that control space based technology may need to take action to protect their equipment from plasma in the solar wind.

The differences seen with all three models, for all three scalar plots, before the B_z^{IMF} reversal, show that under northward IMF conditions, the model output depends strongly on preconditioning time. With a different output from the same model, there is an expectation that this would change the effects that the B_z^{IMF} reversal has on each model under non-artificial conditions. This preconditioning result is similar to results seen with each event validity validation done where each result is different because the conditions before B_z^{IMF} reversals were different, as seen in a study by *Juusola et al.* (2013).

After the B_z^{IMF} reversal, all three models had smaller differences. The BATS-R-US and SWMF models both show a decrease of difference to near zero percent. The OpenGGCM

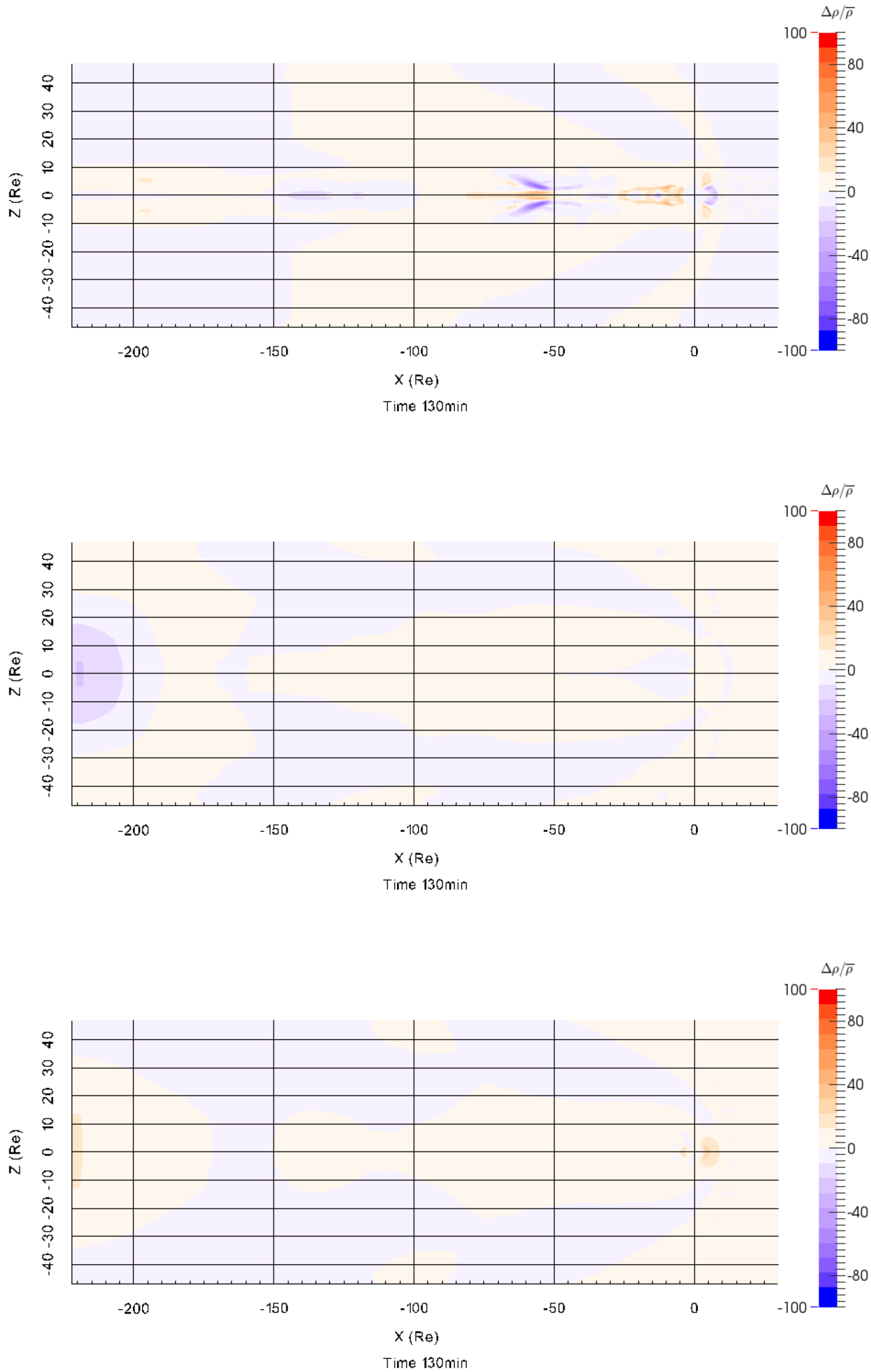

Figure 4.17: ρ percent differences between the OpenGGCM model early and late reversals (top), BATS-R-US early and late reversals (middle), and SWMF early and late reversals (bottom) 60 minutes after the B_z^{IMF} reversal.

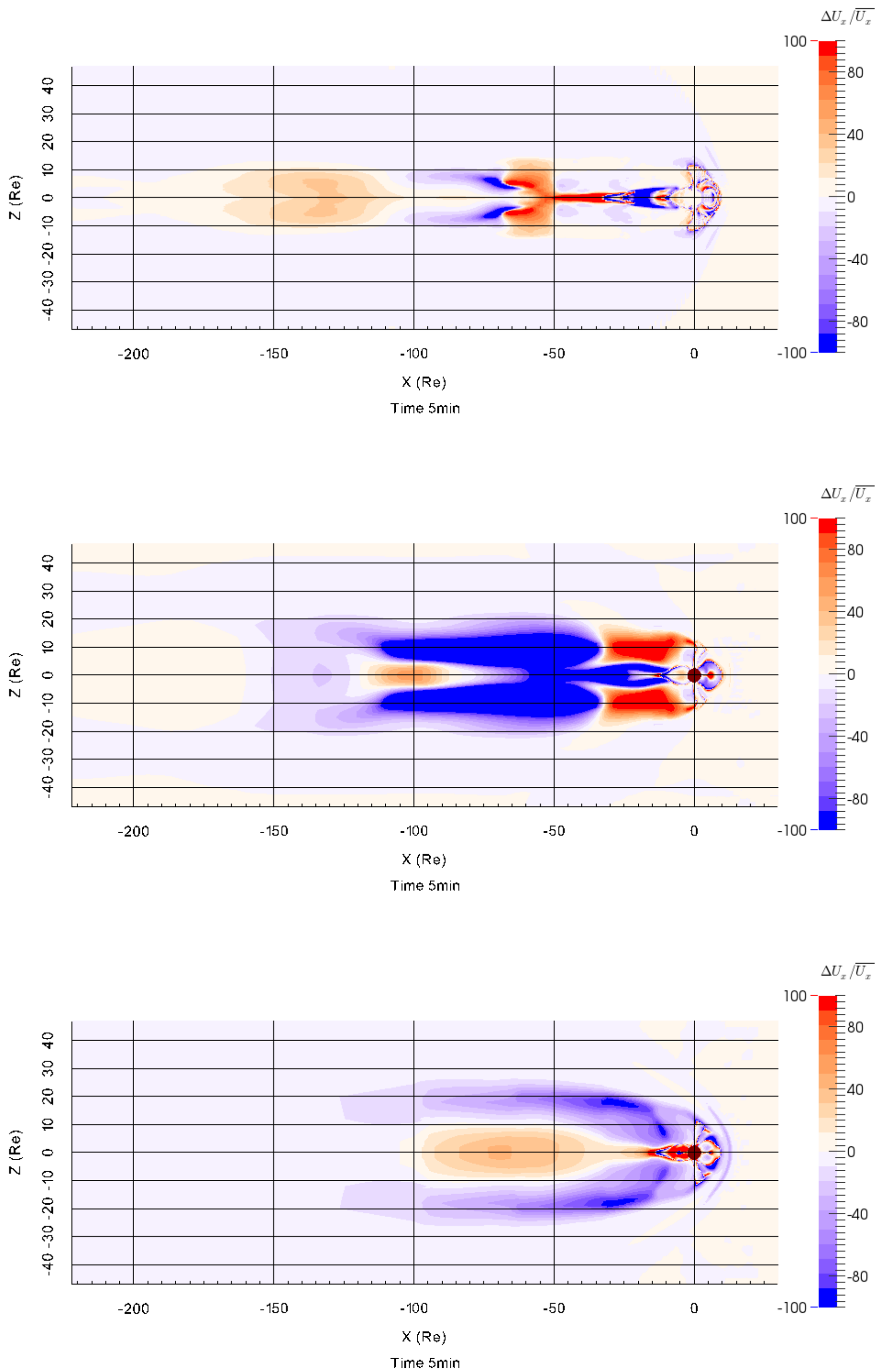

Figure 4.18: ρ percent differences between the OpenGGCM model early and late reversals (top), BATS-R-US early and late reversals (middle), and SWMF early and late reversals (bottom) 25 minutes before the B_z^{IMF} reversal.

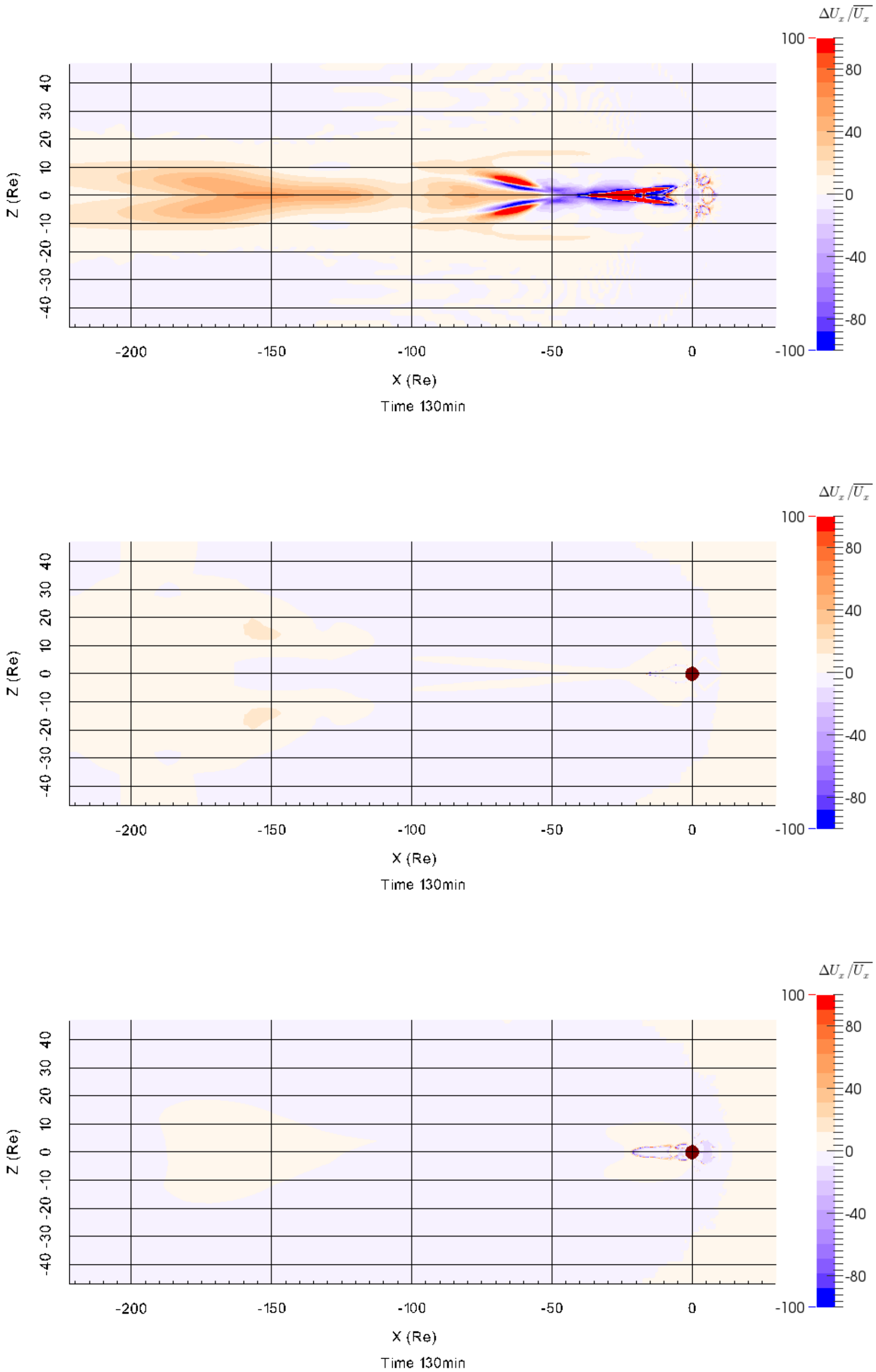

Figure 4.19: ρ percent differences between the OpenGGCM model early and late reversals (top), BATS-R-US early and late reversals (middle), and SWMF early and late reversals (bottom) 60 minutes after the B_z^{IMF} reversal.

model was the exception in the current sheet region.

In determining if these models had enough preconditioning, the evidence from this research shows a significant sensitivity to preconditioning time before the B_z^{IMF} reversal and much smaller differences after the B_z^{IMF} reversal.

Summary

- Longer preconditioning time allowed the magnetosphere to relax more giving different positions for the magnetopause with all three models.
- The OpenGGCM model magnetopause position differences were larger than that of SWMF or BATS-R-US.
- There were large differences for all three models before the B_z^{IMF} reversal.
- The differences in the current sheet region for the OpenGGCM model were similar before and after the reversal.
- The BATS-R-US and SWMF model differences decreased after the B_z^{IMF} reversal to near zero.

4.3 Extreme conditions in the magnetosphere

4.3.1 Background and Motivation

In order to improve predictability of the magnetopause location under extreme events, *Shue et al.* (1998) took magnetopause crossing satellite measurements and compared them to two models. The first model (*Petrinic and Russell*, 1996) was compared to the *Shue et. al.* (1997) model. Both models compared well with the magnetopause crossings at the day-side magnetopause, while the *Shue et. al.* (1997) model had a poorer fit for magnetopause crossings at the flanks. The explanation for the discrepancies was that they were "due to the inappropriate linear extrapolation from the parameter range for average solar wind conditions to that for extreme conditions". Upon correction, the *Shue et. al.* (1997) model was able to better predict magnetopause flank crossings.

Companies and government agencies with space-based assests are interested in the duration of extreme storms. *Cid et al.* (2013) studied the effectiveness of a hyperbolic function for estimating the decay time after minimum D_{st} values for extreme storms. A hyperbolic function was used because previously used linear functions did not accurately predict the the decay time of extreme storms. The extremity of the storm was determined by the D_{st} index where data was available, and a "Local Disturbance Index" taken from the H component of geomagnetic field measured at each observatory where D_{st} data was not available.

Extreme space weather events are an active area of research. For example, statistical analysis on the long range correlations was by *Sharma and Veeramani* (2011) used a database of over 5 million events. The basis for the research was that dynamical and statistical features in extreme events are complicated due to the turbulent nature of the solar wind. An auto-correlation function and a detrended fluctuation analysis were performed to find the long-range correlations. In this work, the extreme events were compiled from a database. Although the used data was not model–based and the approach involved examining statistical properties, it did not involve a comparison to other models. By comparing multiple

Table 4.4: Input parameters for extreme conditions experiment

Run Num.	ρ	T	Vx	B_z
3	11	101289	-604	-3.0
4	2	101289	-320	3.1

models given the same generic input, as done in this experiment, along with the extremes of input variables, forecasters may gain a better understanding of which model is best to use for a variety of extreme space weather conditions.

4.3.2 Methodology

The similarities of the methodologies in all three experiments are described in the methodology section for the B_z^{IMF} reversal experiment in section 4.1.3 of this dissertation.

As shown in Table 4.4, in order to compress the magnetosphere, input variables were chosen corresponding to a high solar wind velocity, a negative solar wind magnetic field, and a high solar wind density. Under high compression, magnetospheric features may be difficult to resolve due to limitations in resolution. For the low compression run, input variables were chosen that lead to a small compression of the magnetosphere: a low solar wind velocity, a positive B_z, and a low density.

4.3.3 Results

High Magnetospheric Compression

As shown in Figure 4.20, all three models have similar B_z contours. The OpenGGCM model magnetopause is closest to Earth. In Figure 4.21, the BATS-R-US model magnetopause is shown to be farther Sunward than that for the SWMF model. Figure 4.21 also shows higher B_z values to occur in the tail region for the BATS-R-US and SWMF models.

The shape of the BATS-R-US and SWMF magnetosphere at the end of the model runs have not significantly changed from the beginning, as shown in Figure 4.22. The OpenGGCM model has higher B_z values in the near-Earth current sheet region. The values of B_z, ρ and

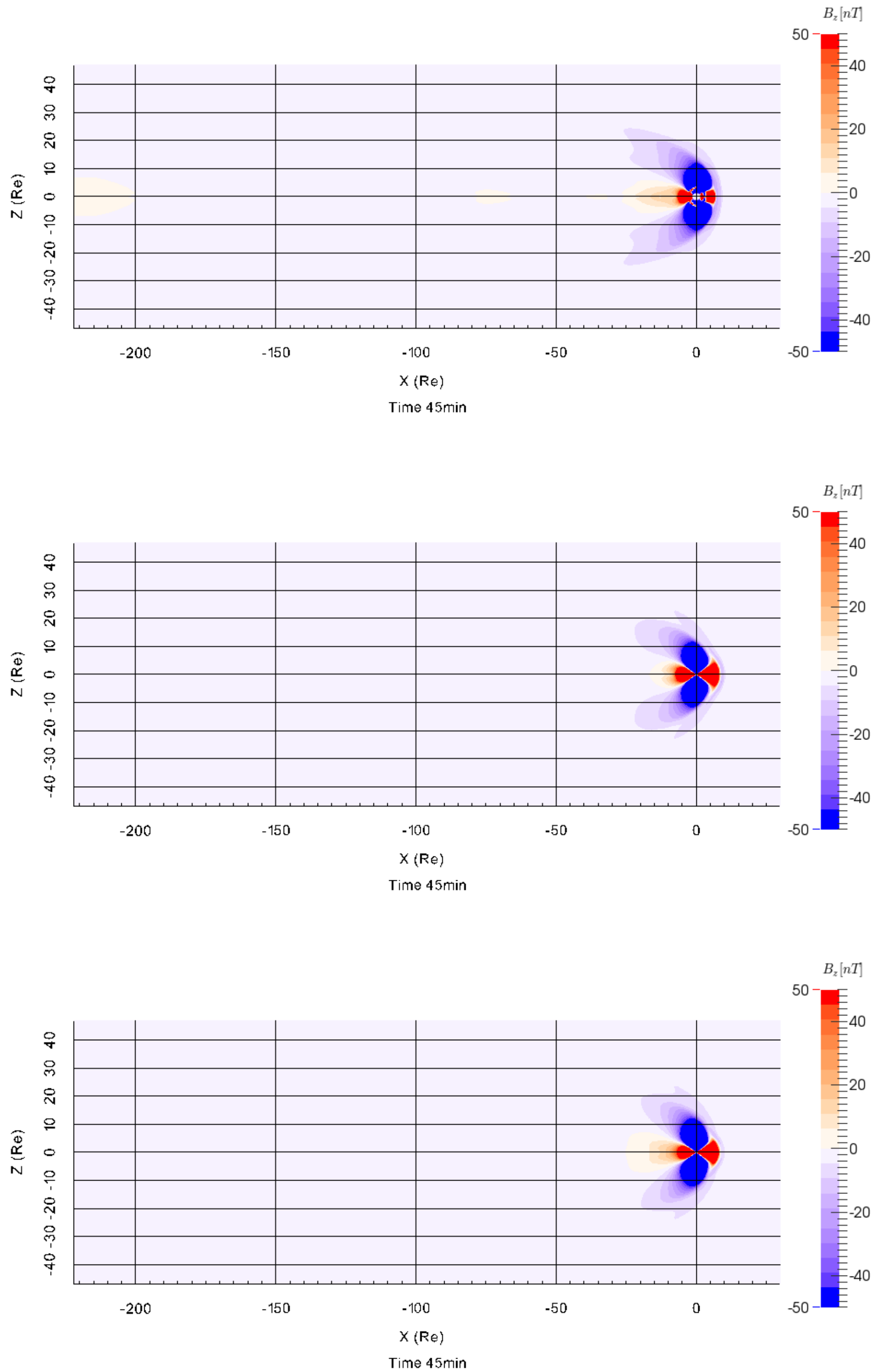

Figure 4.20: B_z for OpenGGCM (top), BATS-R-US (middle), and SWMF (bottom).

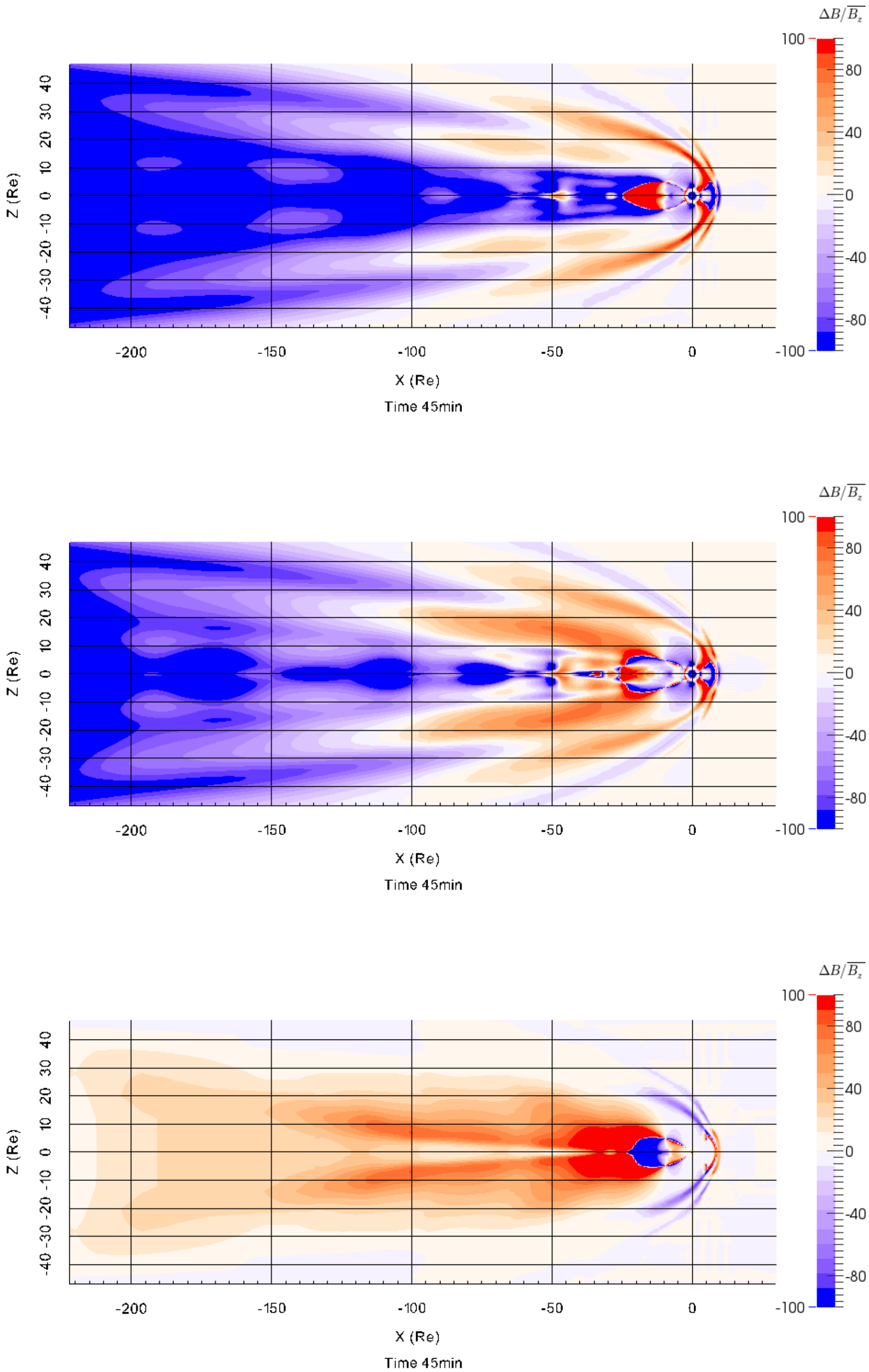

Figure 4.21: B_z percent differences between OpenGGCM and BATS-R-US (top), OpenGGCM and SWMF (middle), and BATS-R-US and SWMF (bottom).

U_x stabilize to a near constant value approximately one hour into the BATS-R-US run. The BATS-R-US and SWMF models, compared in Figure 4.23, show large regions of higher B_z from the BATS-R-US model that are next to regions with higher B_z from the SWMF model. The SWMF model, viewed from U_x plots, shows the largest oscillations.

With a dense and fast solar wind, a large region of high density at the magnetopause is expected, consistent with Figure 4.24. Also, as described in the first experiment, the OpenGGCM model does not include a model of the inner magnetosphere while the SWMF model does, and the observations are consistent with this. In Figure 4.24, the top two plots show the BATS-R-US and SWMF models to have higher densities in the current sheet region compared to the OpenGGCM, while the bottom plot shows that the densities in the current sheet are similar between the BATS-R-US and SWMF models. The scalar ρ plots do not show many differences from the beginning to the end of the run.

As shown in Figure 4.26, all three models begin with high tailward U_x in the current sheet region. The maximum U_x observed in each model is different. The OpenGGCM model (top) maximum U_x is 1,410 km/s, the BATS-R-US model (middle) maximum U_x is 1,560 km/s, while the SWMF model (bottom) maximum U_x is 841 km/s. The SWMF model maximum U_x is just over half of the other two models. At the end of the runs, as shown in Figure 4.27, the same movements occur in the BATS-R-US model (middle) and SWMF (bottom), and the same region that was observed in the OpenGGCM model (top) is observed in U_x plots as a large region of Earthward velocity.

As shown in Figure 4.28, the largest differences are in the current sheet region for all three comparisons. Between the OpenGGCM and BATS-R-US models (top) the BATS-R-US model has largest differences in U_x, with the OpenGGCM model having larger differences in the tail lobes. Between the OpenGGCM and SWMF models (middle), the SWMF model has larger differences. Between the BATS-R-US and SWMF models (bottom) the BATS-R-US model has the largest differences in U_x in the current sheet region with the SWMF model having larger differences in the tail lobes of the distant tail. As time progresses, all three comparisons have differences similar to that observed in the beginning of the run. The

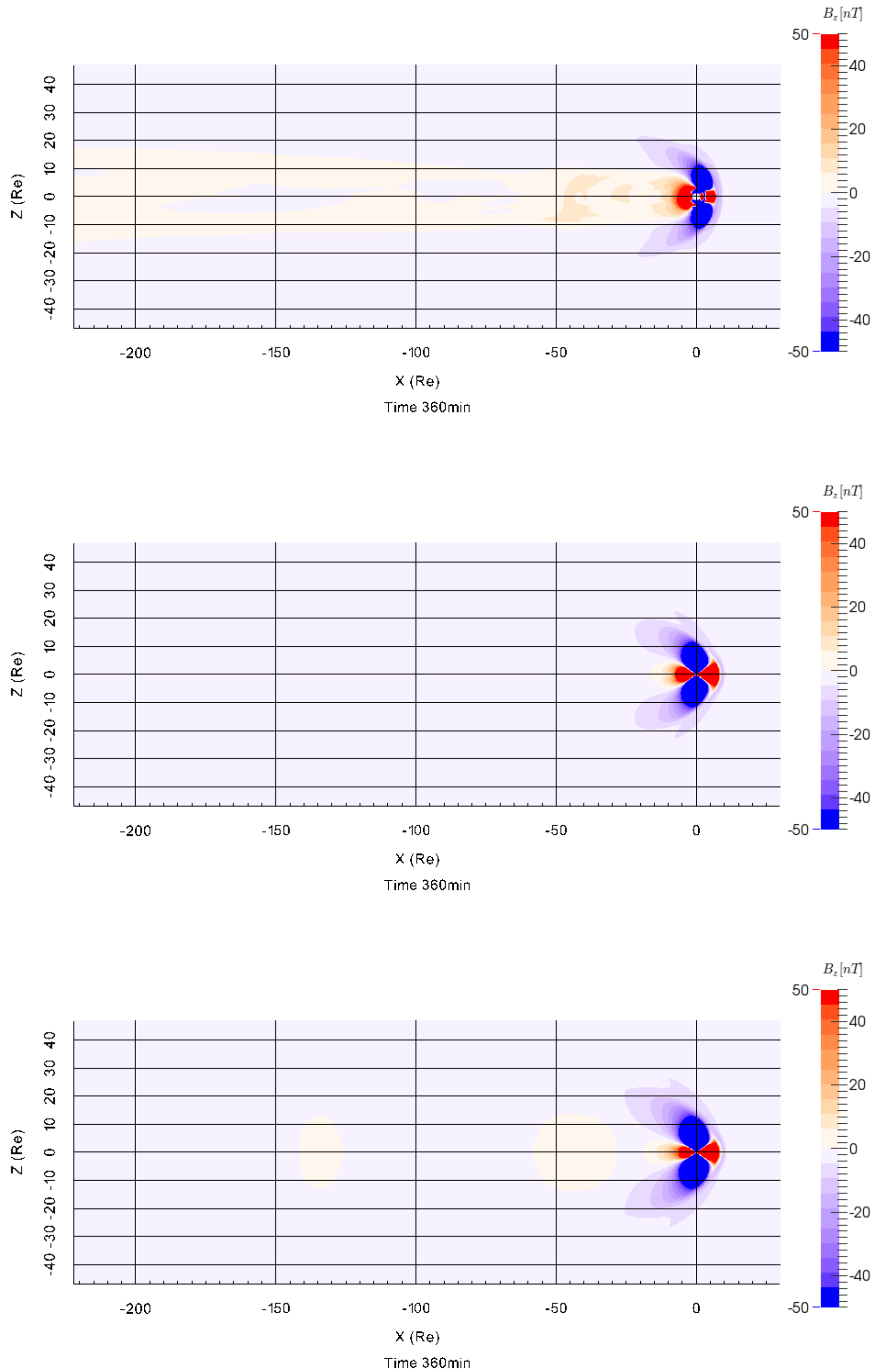

Figure 4.22: B_z for OpenGGCM (top), BATS-R-US (middle), and SWMF (bottom).

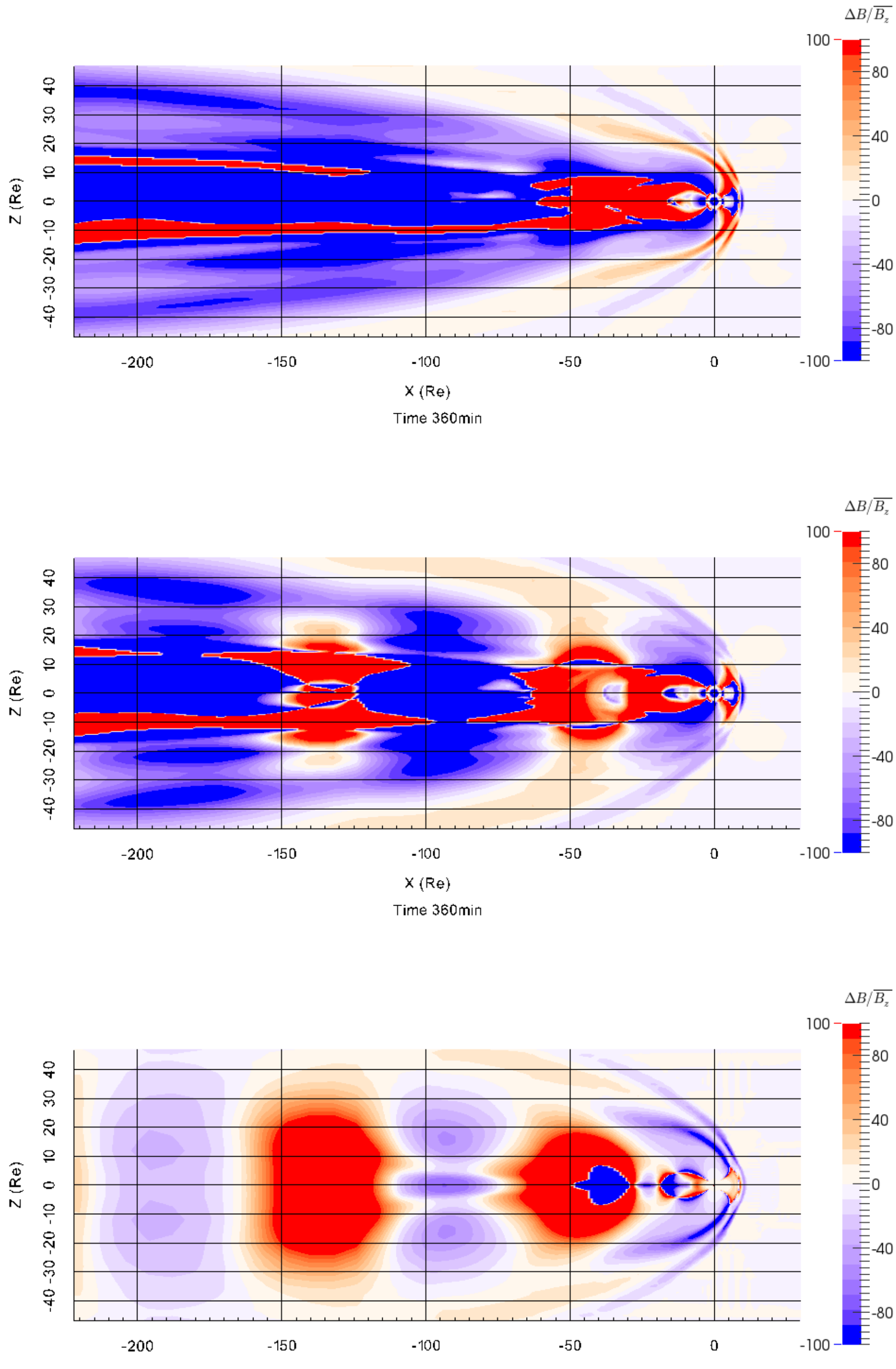

Figure 4.23: B_z percent differences between OpenGGCM and BATS-R-US (top), OpenGGCM and SWMF (middle), and BATS-R-US and SWMF (bottom).

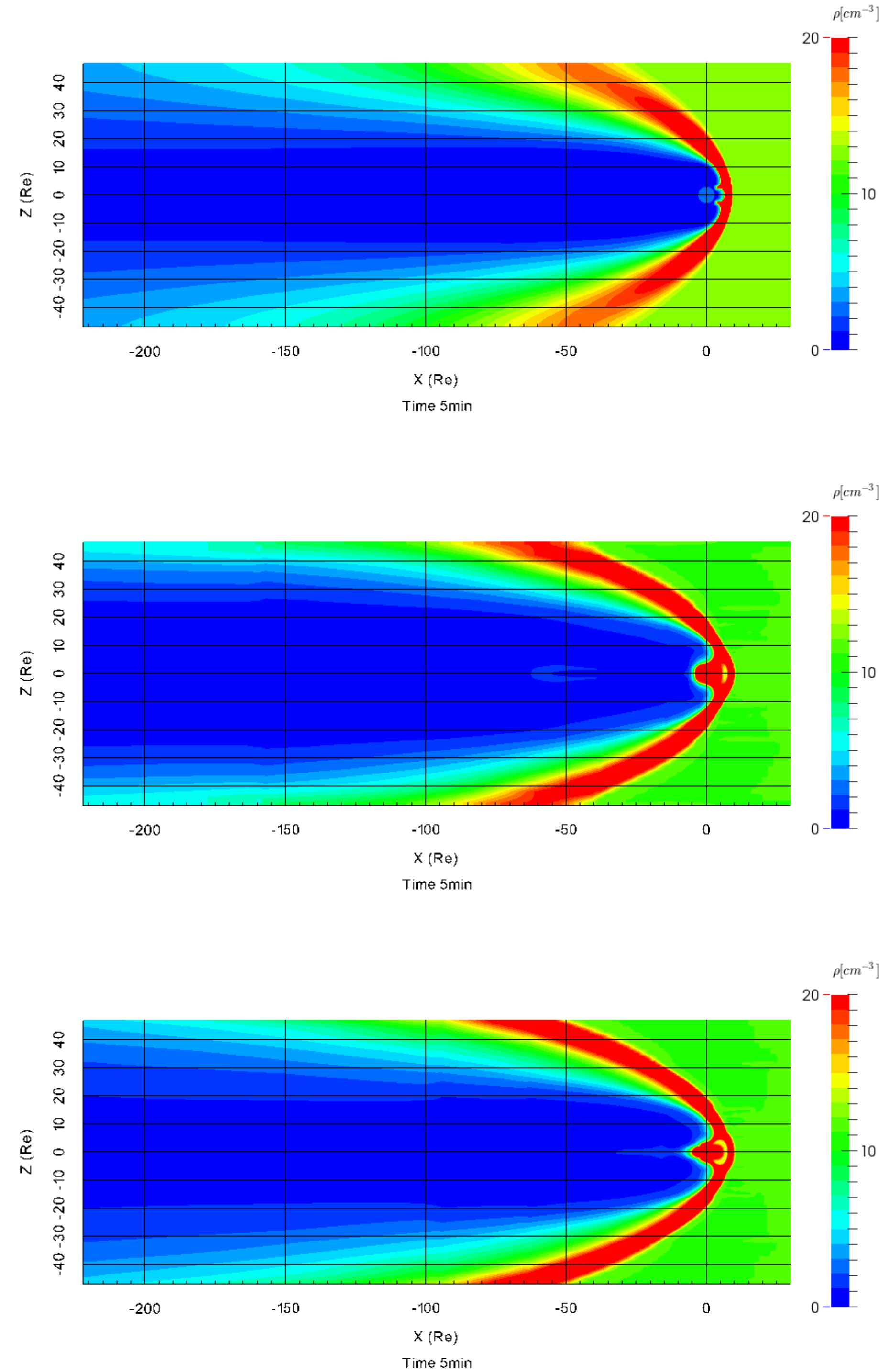

Figure 4.24: ρ for OpenGGCM (top), BATS-R-US (middle), and SWMF (bottom).

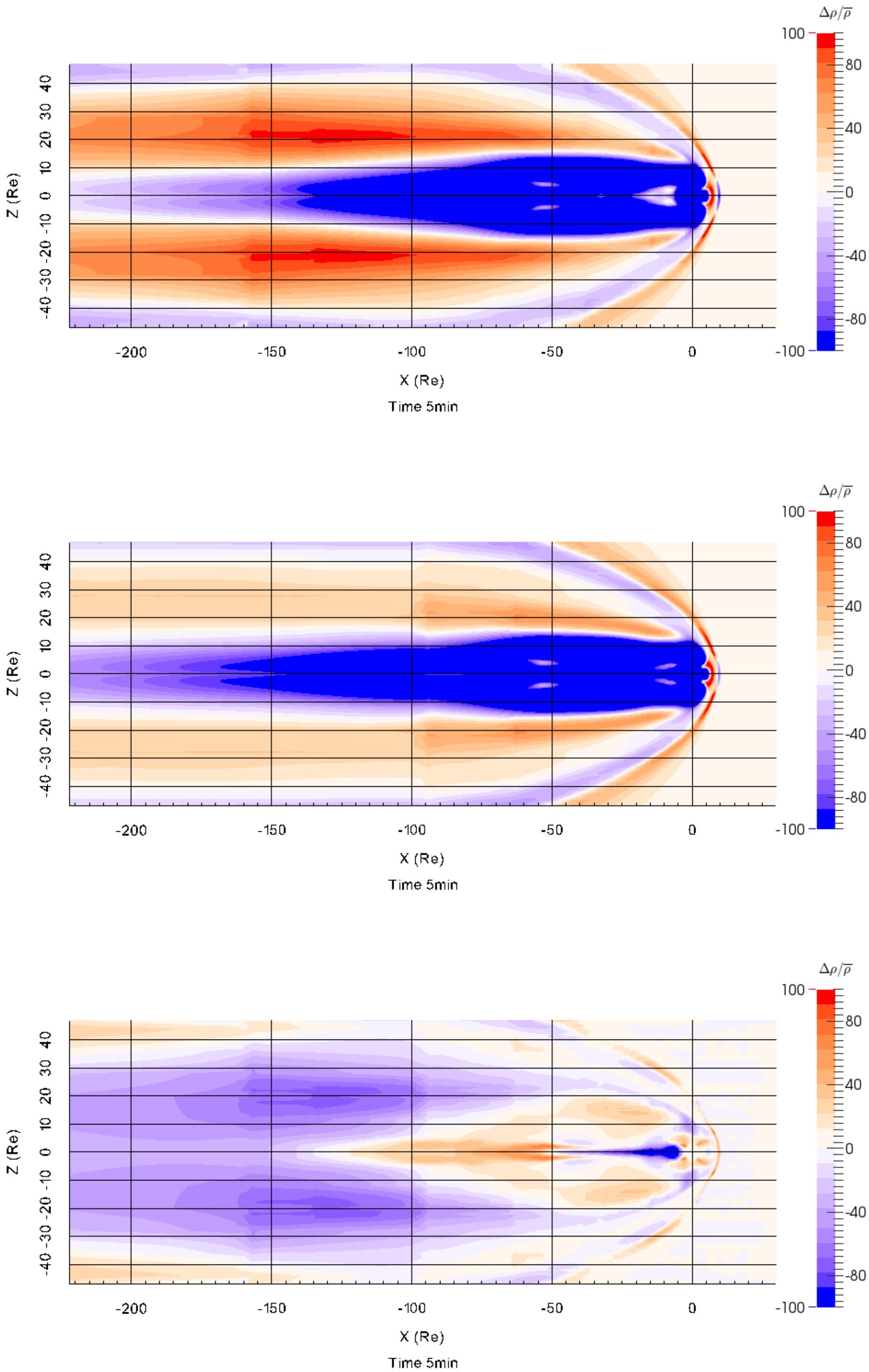

Figure 4.25: ρ percent differences between OpenGGCM and BATS-R-US (top), OpenGGCM and SWMF (middle), and BATS-R-US and SWMF (bottom).

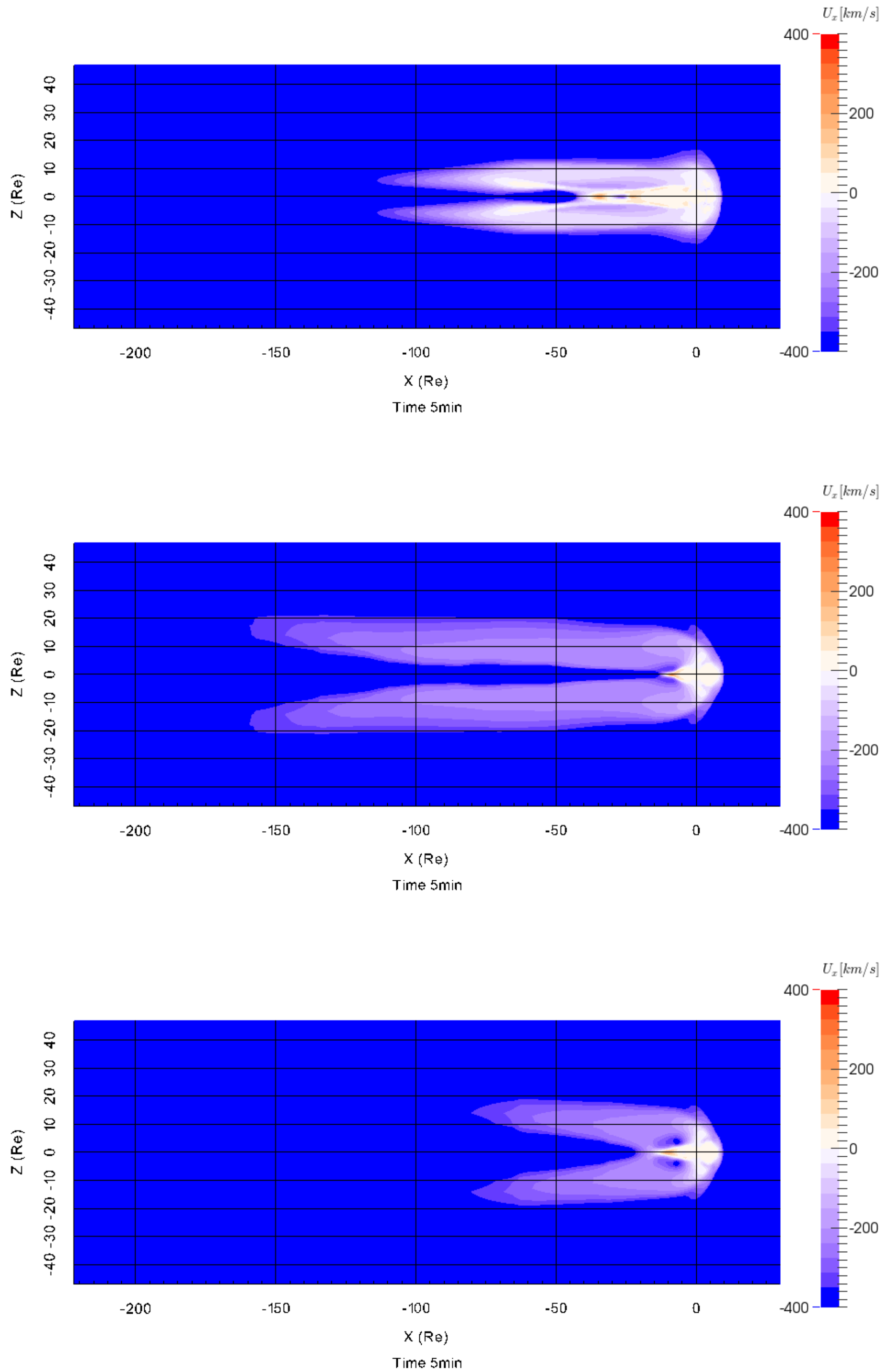

Figure 4.26: U_x for OpenGGCM (top), BATS-R-US (middle), and SWMF (bottom).

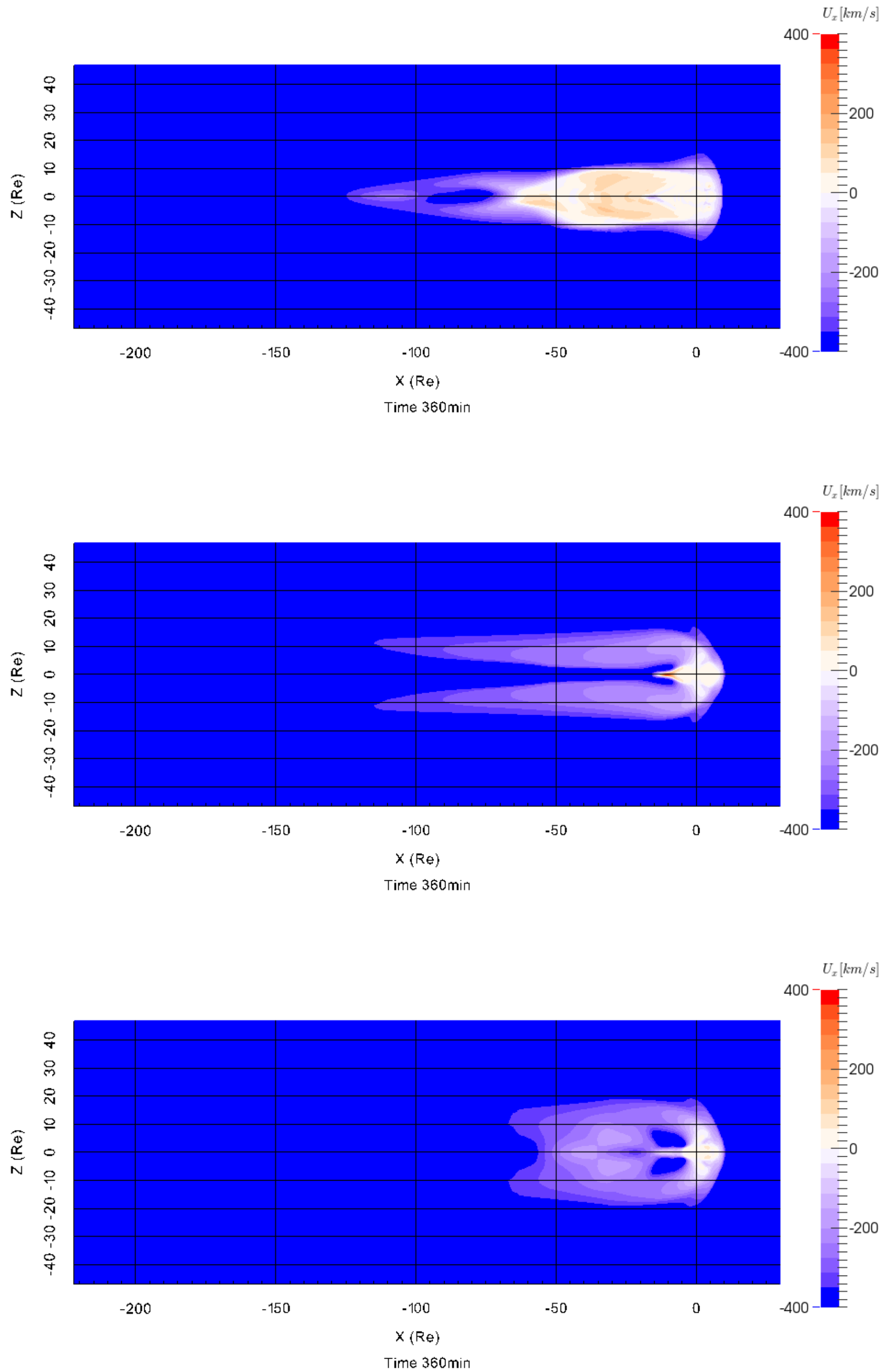

Figure 4.27: U_x for OpenGGCM (top), BATS-R-US (middle), and SWMF (bottom).

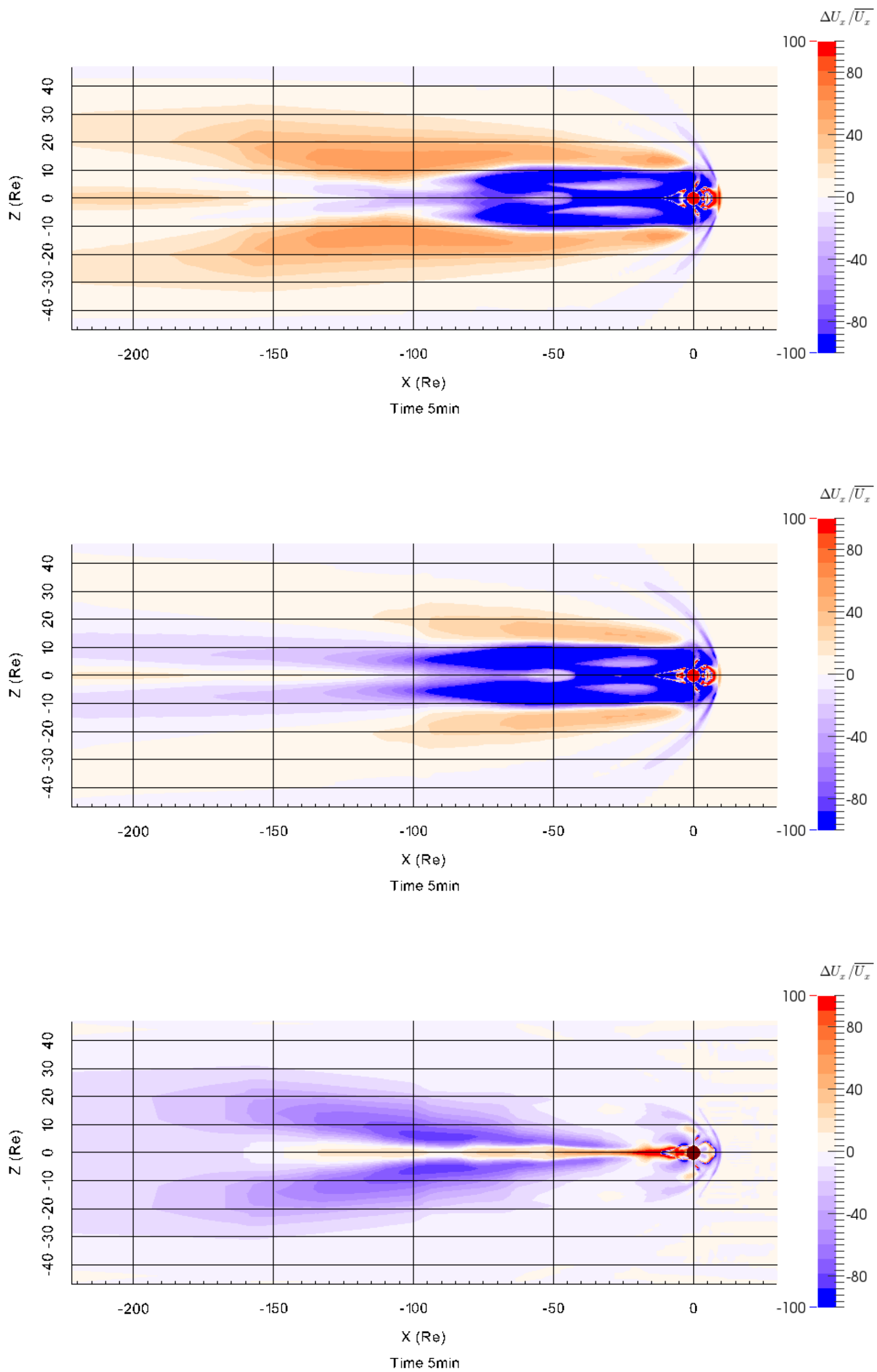

Figure 4.28: U_x percent differences between OpenGGCM and BATS-R-US (top), OpenGGCM and SWMF (middle), and BATS-R-US and SWMF (bottom).

differences between the BATS-R-US and SWMF models have increased in the current sheet region giving the BATS-R-US model higher values, as shown in Figure 4.29.

Low Magnetospheric Compression

This section contains a discussion of the differences between the three models for conditions that lead to a low magnetospheric compression. As shown in Figure 4.30, B_z in the OpenGGCM model (top) shows the most stretching in the magnetotail, while the BATS-R-US (middle) and SWMF (bottom) appear similar to each other and do not stretch as far. As time progresses, the OpenGGCM model shows the most fluctuations, while the BATS-R-US and OpenGGCM models have minimal fluctuations. For all three models, there is minimal change from the beginning of the run to the end of the run.

As shown in Figure 4.31, the OpenGGCM and BATS-R-US models (top) and the OpenGGCM and SWMF models (middle) differences are similar. The differences between the BATS-R-US and SWMF models are near zero for all regions in the magnetosphere. There is only a small region of differences in the magnetopause tailward of the cusps. As time progresses in the run, there are minimal changes between all three models, although the OpenGGCM and BATS-R-US models have a difference reduction in the current sheet region. The same is true for the OpenGGCM and SWMF model differences.

The maximum density for the OpenGGCM, BATS-R-US and SWMF model runs are 11 cm^{-3}, 29 cm^{-3} and 29 cm^{-3} respectively. As shown in Figure 4.32, the near-Earth ρ is high for the BATS-R-US and SWMF models with the OpenGGCM model having low ρ. There is minimal change between the three models for the length of the run.

As shown in Figure 4.33, the OpenGGCM vs. BATS-R-US models (top) and the OpenGGCM vs. SWMF models (middle) show large differences near Earth extending tailward in the current sheet region. The only differences between the BATS-R-US and SWMF models (bottom) are near Earth where the BATS-R-US model has the larger differences with the SWMF model having higher values in the distant tail lobes. As time progresses, there are no major changes in the plots.

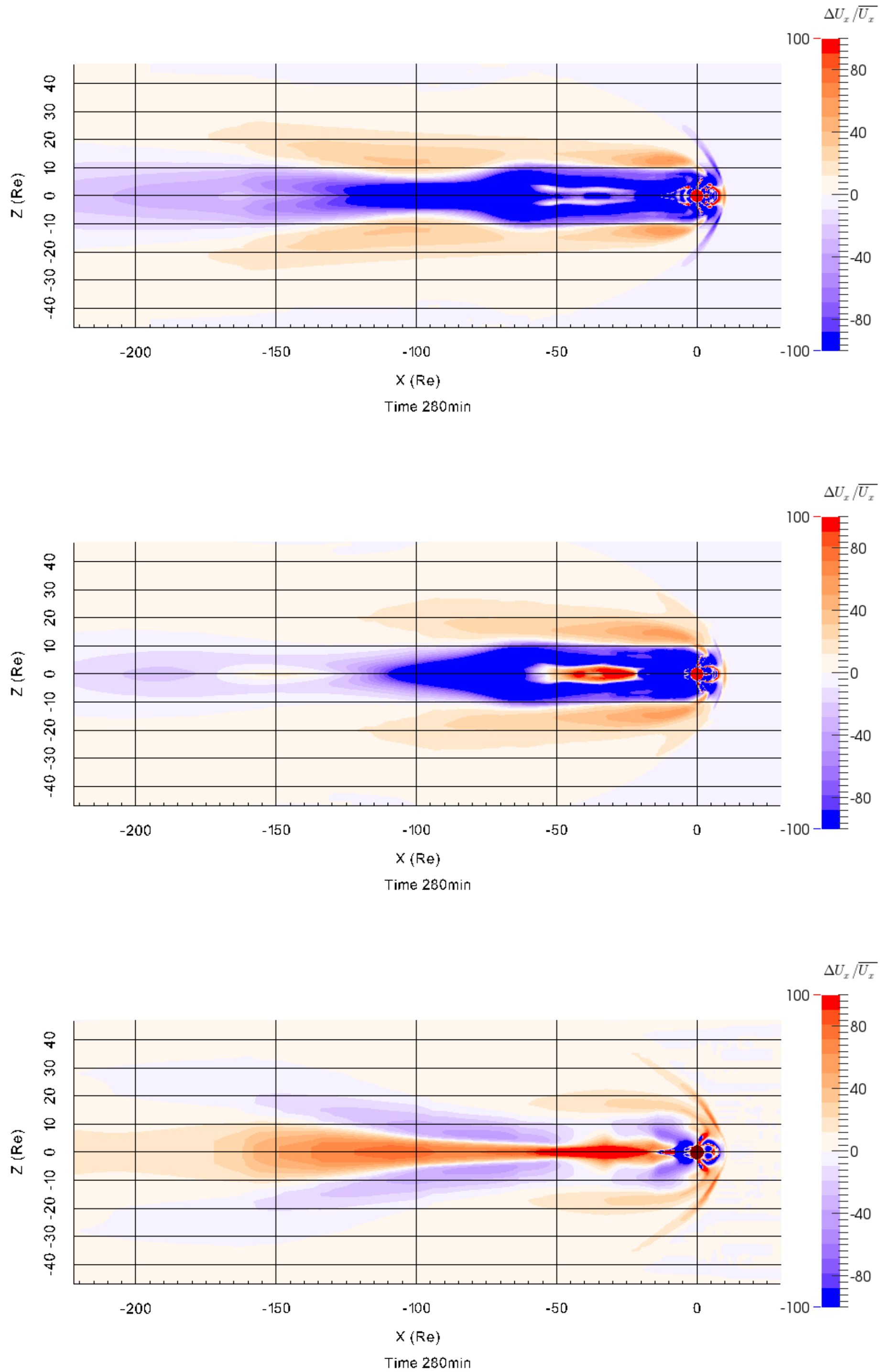

Figure 4.29: U_x percent differences between OpenGGCM and BATS-R-US (top), OpenGGCM and SWMF (middle), and BATS-R-US and SWMF (bottom).

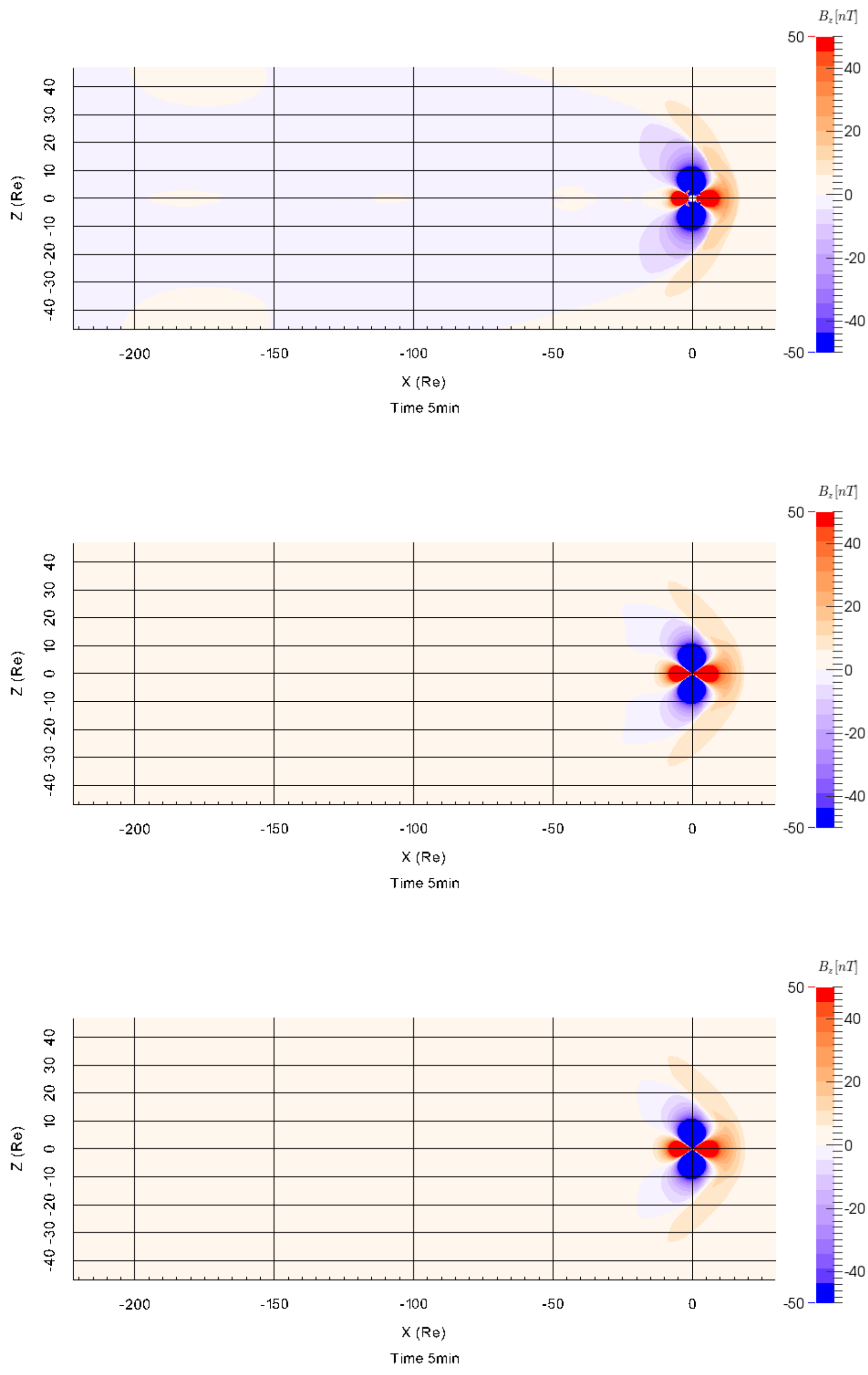

Figure 4.30: B_z for OpenGGCM (top), BATS-R-US (middle), and SWMF (bottom).

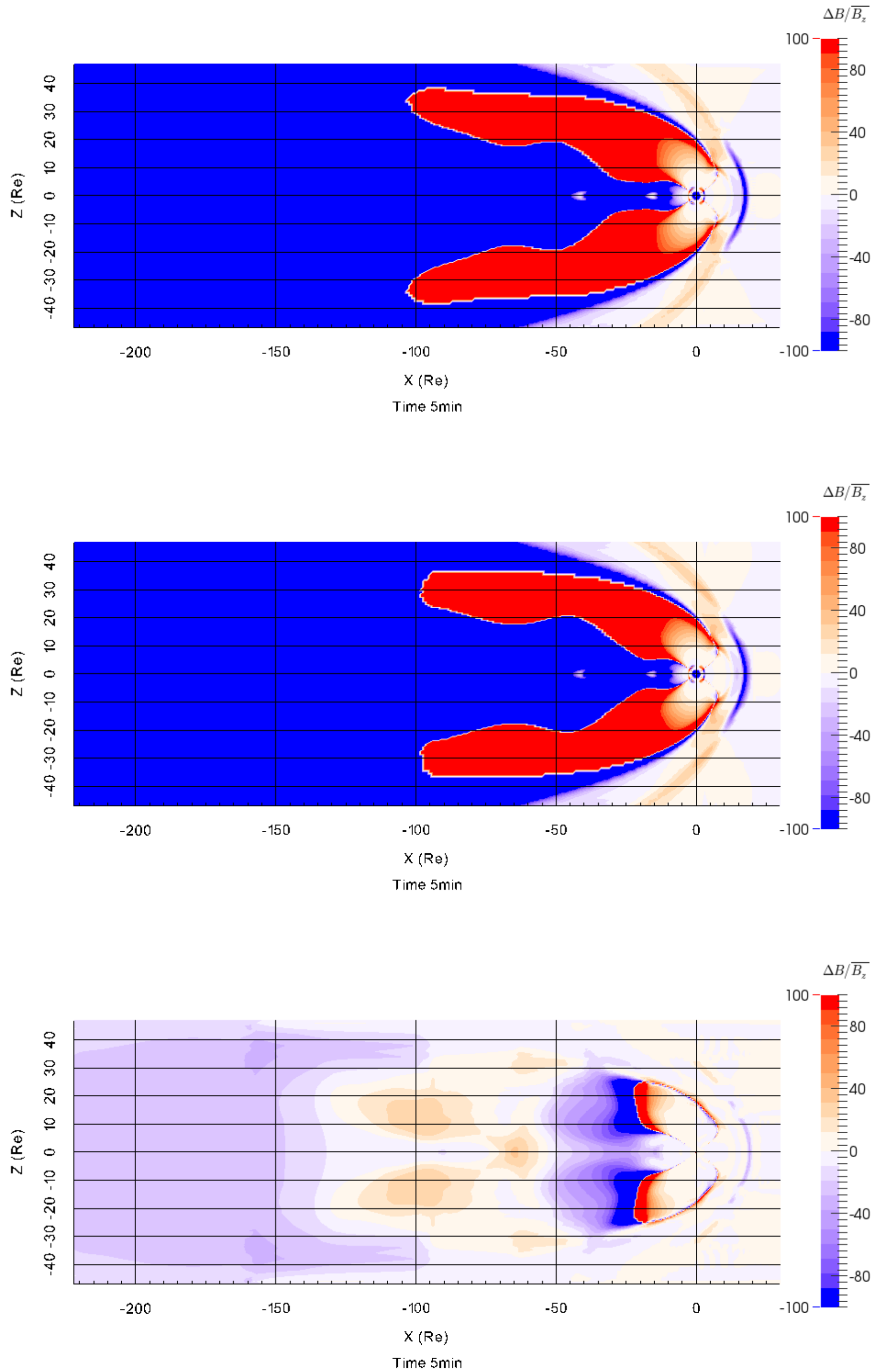

Figure 4.31: B_z percent differences between OpenGGCM and BATS-R-US (top), OpenGGCM and SWMF (middle), and BATS-R-US and SWMF (bottom).

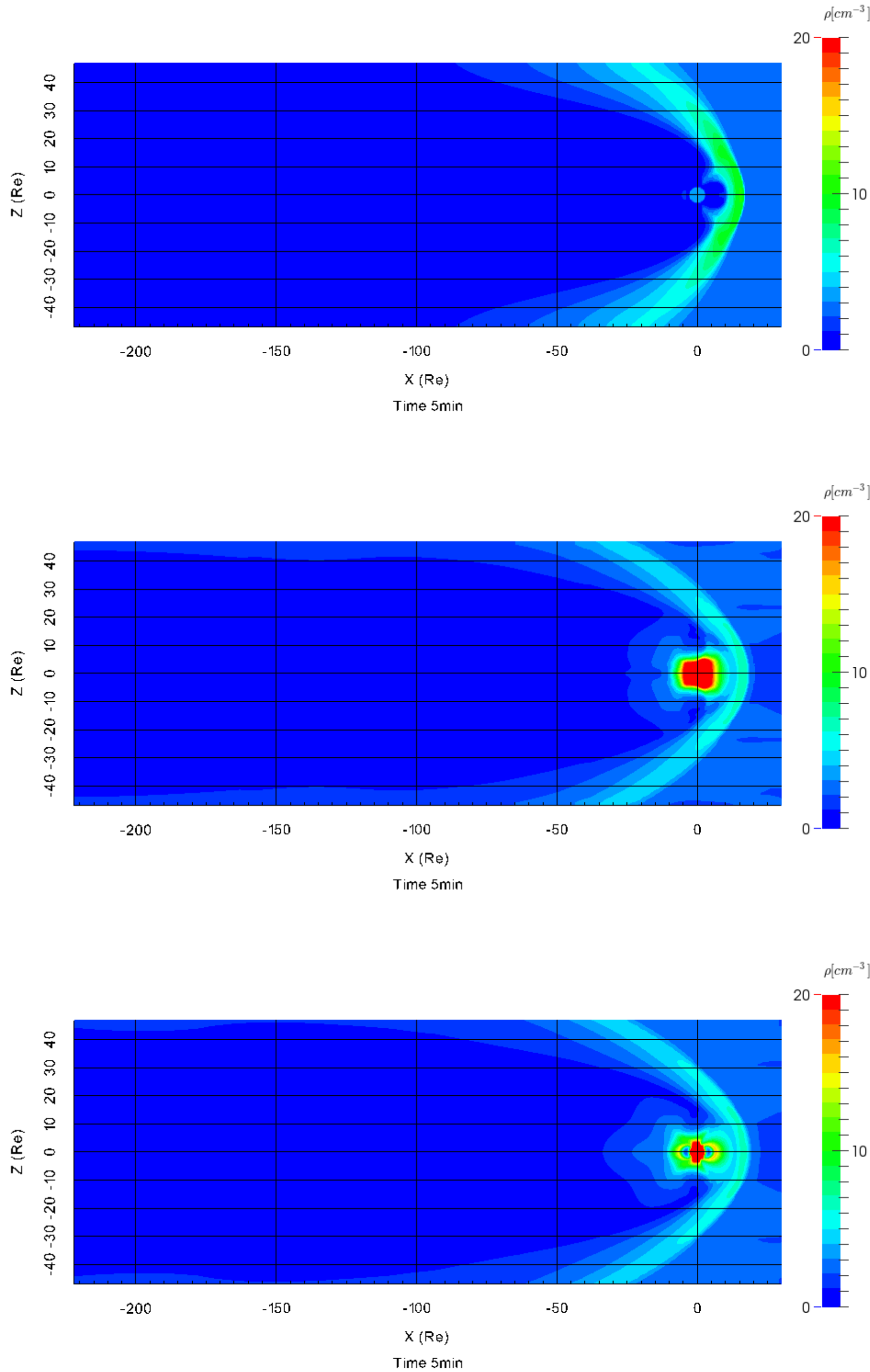

Figure 4.32: ρ for OpenGGCM (top), BATS-R-US (middle), and SWMF (bottom).

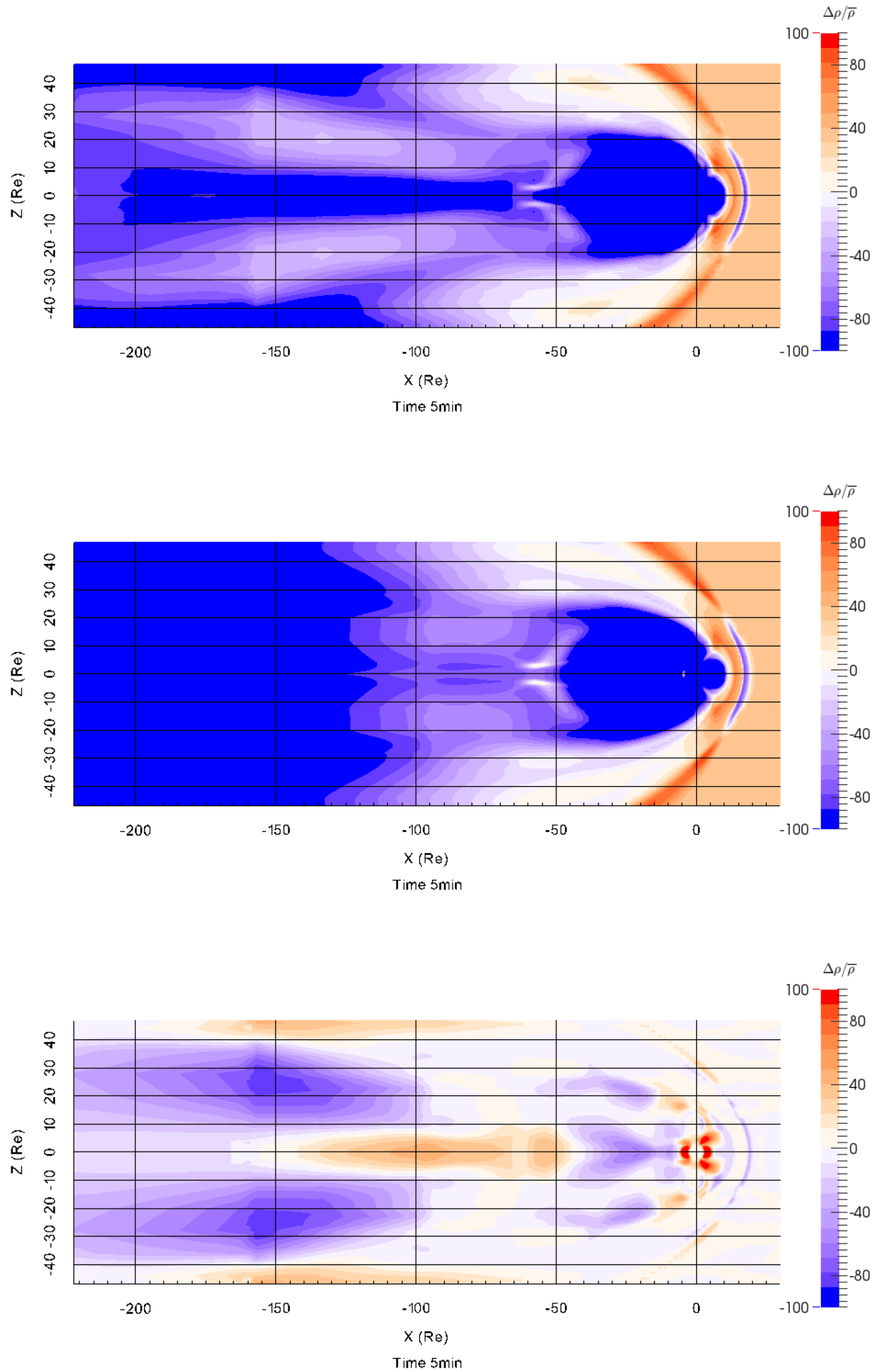

Figure 4.33: ρ percent differences between OpenGGCM and BATS-R-US (top), OpenGGCM and SWMF (middle), and BATS-R-US and SWMF (bottom).

The maximum U_x for the OpenGGCM, BATS-R-US, and SWMF models are 809 km/s, 347 km/s and 349 km/s, respectively. Shown in Figure 4.34, the current sheet U_x is high for the OpenGGCM but not for the BATS-R-US and SWMF models. There is minimal change between the three models for the length of the time series. The OpenGGCM model has fluctuations in the tail region for U_x, while the other two models do not.

As shown in Figure 4.35, the OpenGGCM vs. BATS-R-US models (top) have higher U_x in the current sheet and near-Earth regions for the OpenGGCM model. The OpenGGCM vs. SWMF models (middle) differences in U_x are higher in the current sheet and near-Earth regions for the OpenGGCM model. The BATS-R-US vs. SWMF model differences show high values for the BATS-R-US model in the near-Earth tail lobes of the magnetosphere.

4.3.4 Discussion and Conclusions

High Compression

A strong southern component of the solar wind IMF will weaken the magnetic field at Earth's magnetopause due to their different orientations. Combined with a fast solar wind velocity and high solar wind densities, the magnetosphere will compress because the kinetic pressure from the solar wind becomes larger than the magnetic pressure of Earth's magnetic field.

The B_z plots show magnetopause locations. The OpenGGCM model is closest to Earth due to the weaker magnetic pressure that is a result of the model not accounting for a ring current. The BATS-R-US magnetopause, because it does not account for the ring current, is expected to be similar to the OpenGGCM. This is not observed in the results, and is likely due to differences in how each model couples to the inner boundary. The SWMF magnetopause location is expected to be farther from Earth than that of the OpenGGCM model.

The three models produce three different predictions of how the magnetosphere reacts to solar wind conditions that will cause high compression. The OpenGGCM model has a region of higher B_z in the near-Earth current sheet region at the end of the run. There

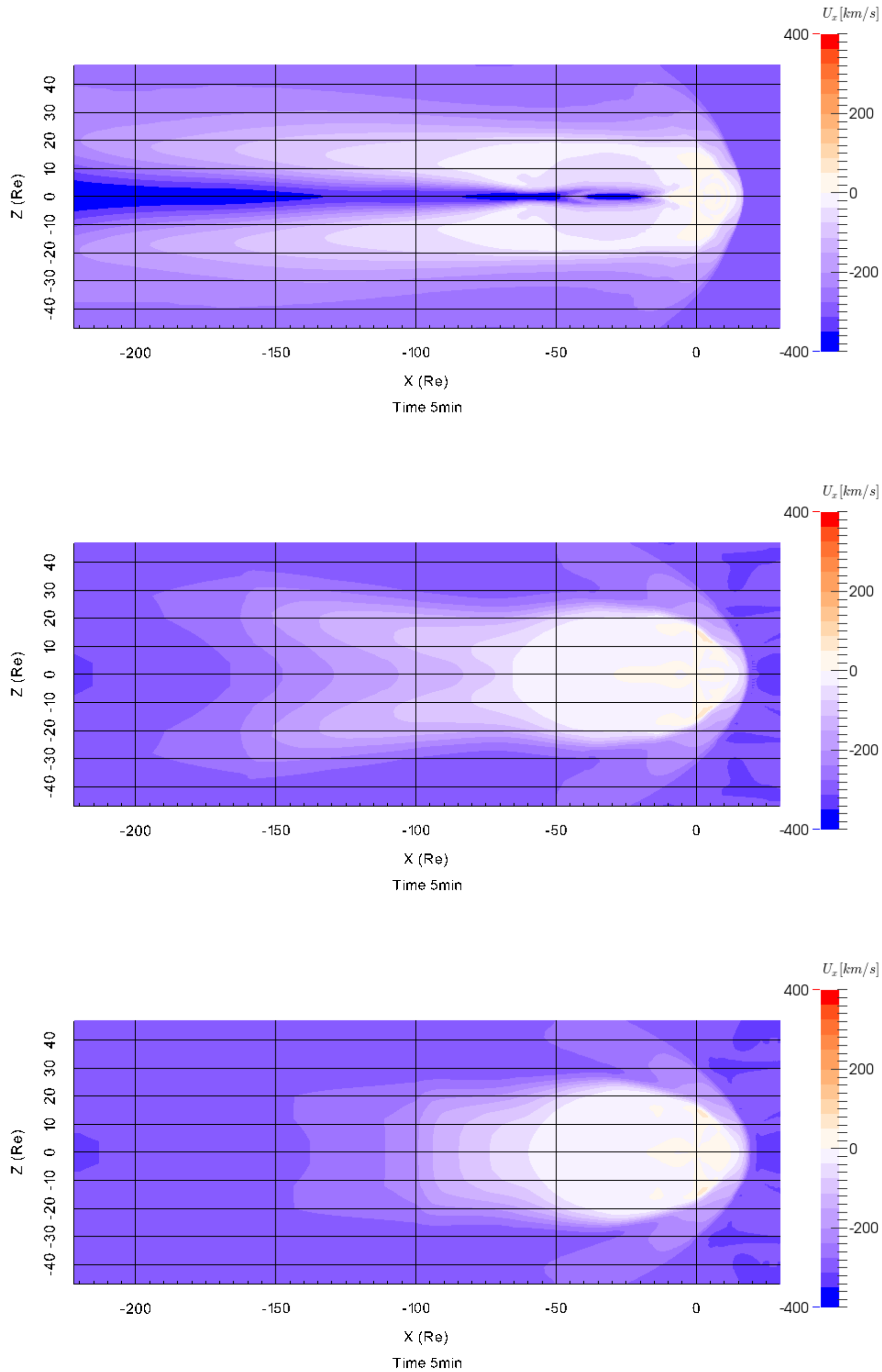

Figure 4.34: U_x for OpenGGCM (top), BATS-R-US (middle), and SWMF (bottom).

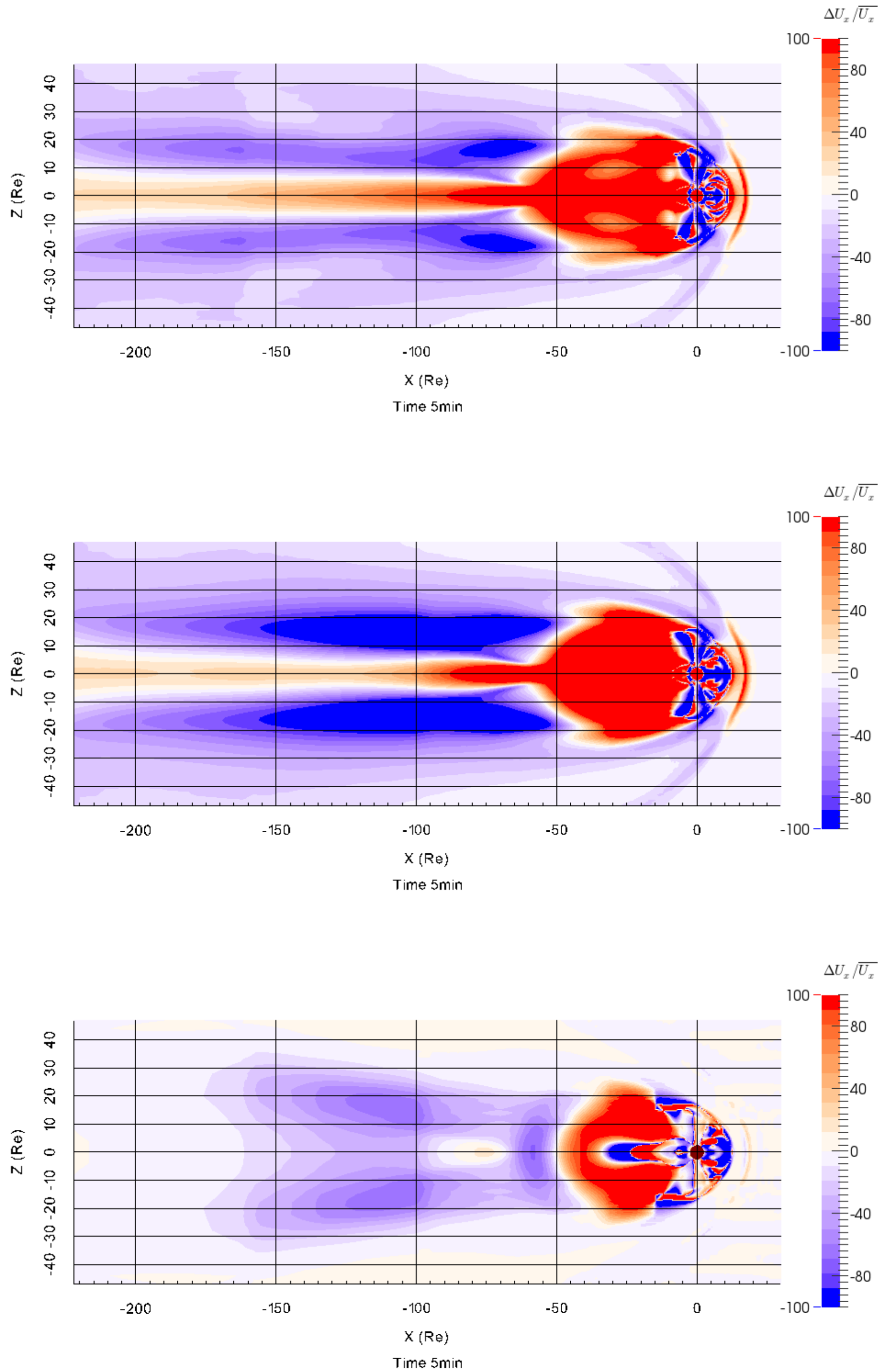

Figure 4.35: U_x percent differences between OpenGGCM and BATS-R-US (top), OpenGGCM and SWMF (middle), and BATS-R-US and SWMF (bottom).

are high Earthward velocities in the same region at the end of the run. The velocities in the tail region come from reconnection in the current sheet. The BATS-R-US model appears to stop movement entirely before the midway point of the run. The reasoning for this result is currently unknown and requires further research. The SWMF model, as time progresses, appears to oscillate with increasing movement not stopping by the end of the run. One hypothesis is that there is a destabilization caused by the RCM in which the global magnetosphere starts to oscillate. Towards the end of the run there is little increase in the oscillations, and along with the OpenGGCM model results, it would be important to study the model results with a longer time frame than 6 hours.

Low Compression

Opposite to the conditions for a high compression of the magnetosphere, low compression occurs with a slow solar wind U_x, a positive B_z and a low ρ. B_z^{IMF} and Earth's B_z are both the same direction, which increases the magnetic field strength at the magnetopause causing a strong magnetic pressure that pushes the magnetopause Sunward. The effect of the ring current is minimal, which keeps the magnetopause locations fairly close to one another for all three models.

The OpenGGCM model current sheet velocities are larger in a low compression environment than that in the BATS-R-US and SWMF models, where the differences were very close to zero over the entire domain. The speeds of plasma in the current sheet can play a large role in the effects of the plasma as observed at Earth. The resistive MHD used in the OpenGGCM model may allow for faster reconnection in the current sheet region and explain the faster velocities observed in the current sheet region.

Summary

For extreme conditions in the solar wind, the following occurs in the considered MHD models of the magnetosphere:

- The OpenGGCM model has a large region of Earthward U_x in the current sheet region that grows as time progresses in a compressed environment.

- The BATS-R-US model is either completely stable or stops in a compressed environment.
- In a compressed environment, the SWMF model will eventually oscillate.
- The OpenGGCM model has the highest tailward velocities under strong compression conditions.
- The RCM inner magnetosphere model may explain the smaller maximum velocities observed in the SWMF model.
- The OpenGGCM model has the highest B_z under strong compression.
- All three models have similar magnetopause positions under low compression.
- The OpenGGCM model current sheet velocities are largest under low compression.

Chapter 5: Summary and Conclusions

The objective of this work was to perform three experiments in order to further our understanding of the behavior of and differences between magnetospheric MHD models. Three experiments were performed. The first experiment was used to determine the differences between model predictions when B_z^{IMF} changed from positive to negative while all other inputs were constant. The second experiment determined the sensitivity of the models to the length of time that they were preconditioned prior to a change in B_z^{IMF} from positive to negative. The third experiment used extreme solar wind conditions, corresponding to weak and strong magnetospheric compression.

The type of analysis performed for this thesis is expected to be useful to model developers. A next step for this research will be to expand the experiments to include more magnetospheric models. We found that the model output depended on preconditioning time; therefore a next step is to determine the shortest preconditioning time for which the output is nearly the same. Another analysis will be to expand the number of artificial input conditions used for the comparisons made in the first experiment.

Finally, an important goal for model developers is to allow forecasters to have and understanding of the uncertainties and differences between the predictions of their models. To accomplish this, the tendencies determined from this thesis should be used when interpreting forecasts. We conclude that more validation of the type performed for this thesis is needed because of the significant differences found between models (and within a given model for different preconditioning times) and the fact that output of these models are regularly used for interpretation of observations.

Appendix A: Run Image Outputs

All images created from model outputs can be found at
http://briandcurtis.com/BDCDissertationImages.html
with the following organizational structure:

- Experiment 1 - B_z reversal (early)
  - Brian_Curtis_042213_1 = OpenGGCM
  - Brian_Curtis_042213_2 = BATS-R-US
  - Brian_Curtis_042213_3 = SWMF
  - Results/0_1 = OpenGGCM - BATS-R-US
  - Results/0_2 = OpenGGCM - SWMF
  - Results/1_2 = BATS-R-US - OpenGGCM
- Experiment 2 - Preconditioning
  - Brian_Curtis_042213_5 = OpenGGCM (late reversal)
  - Brian_Curtis_042213_6 = BATS-R-US (late reversal)
  - Brian_Curtis_042213_7 = SWMF (late reversal)
  - Precondition/Results/0_3 = OpenGGCM (early) - OpenGGCM (late)
  - Precondition/Results/1_4 = BATS-R-US (early) - BATS-R-US (late)
  - Precondition/Results/2_5 = SWMF (early) - SWMF (late)
- Experiment 3 - Extreme Conditions
  - High Compression
    - Brian_Curtis_042413_1 = OpenGGCM
    - Brian_Curtis_042413_2 = BATS-R-US

    * Brian_Curtis_042413_3 = SWMF
    * Results/8_9 = OpenGGCM - BATS-R-US
    * Results/8_10 = OpenGGCM - SWMF
    * Results/9_10 = BATS-R-US - SWMF
- Low Compression
    * Brian_Curtis_042413_5 = OpenGGCM
    * Brian_Curtis_042413_6 = BATS-R-US
    * Brian_Curtis_042413_7 = SWMF
    * Results/12_13 = OpenGGCM - BATS-R-US
    * Results/12_14 = OpenGGCM - SWMF
    * Results/13_14 = BATS-R-US - SWMF

Bibliography

Historical observing metadata repository (homr), 2013.

conservation of energy science definition, 2013a.

conservation of mass science definition, 2013b.

conservation of momentum science definition, 2013c.

Spdf - omniweb service, 2013.

Ccmc openggcm model, 2014.

Nasa - an x1.4 solar flare and a cme, 2014.

Geomagnetic disturbance task force (gmdtf), 2014.

Nasa's cosmicopia – sun –heliosphere, 2014.

Hf and lower frequency radiation - the ionosphere, 2014.

Wmap observatory: Lagrange points, 2014.

The sun-earth connection, 2014.

Nasa's cosmicopia – glossary op, 2014.

Mhd reconnection - scholarpedia, 2014.

Bats-r-us grid, 2014.

Openggcm run jxr02102, 2014.

The sun-earth connection: Heliophysics solar storm and space weather, 2014a.

Apod: 2002 november 14, 2014b.

geometry - how to map a point onto a warped grid, 2014.

Development of an unstructured finite-volume flow solver, 2014.

Ahrens, C. D., *Essentials of Meteorology*, West Pubishing Company, 1994.

Andrejczuk, M., W. W. Grabowski, S. P. Malinowski, and P. K. Smolarkiewicz, Numerical simulation of cloud-clear air interfacial mixing: effects on cloud microphysics, *Atmospheric Science*, *63*, 3204–3225, 2006.

Arge, C. N., D. Odstrcil, V. J. Pizzo, and L. R. Maer, Improved method for specifying solar wind speed near the sun, *AIP Conference Preceedings*, *679*, 190–193, 2003.

Boznar, M. Z., P. Mlankar, and B. Grasic, Short-term fine reolution wrf forecast data validation in complex terrain in slovenia, *International Journal of Environment and Pollution*, *50*, 1–4, 2012.

Buchner, J., T. Dum, and M. Scholer, *Space Plasma Simulation*, Springer-Verlag, 2003.

Chapman, S., and V. C. A. Ferraro, A new theory of magnetic storms, *Nature*, *126*, 129, 1930.

Cid, C., J. Palacios, E. Saiz, Y. Cerrato, J. Aguado, and A. Guerrero, Modeling the recovery phase of extreme geomagnetic storms, *Journal of Geophysical Research*, *118*, 4352–4359, 2013.

Dungey, J. W., Interplanetary magnetic field and the auroral zones, *Physical Review Letters*, *6*, 47–48, 1961.

Echer, E., W. D. Gonzalez, B. T. Tsurutani, and A. L. C. Gonzalez, Interplanetary conditions causing geomagnetic storms (dst $\leq$ -100 nt) during solar cycle 23 (1996-2006), *Journal of Geophysical Research*, *113*, 1–16, 2008.

Fiebrich, C. A., History of surface weather observations in the united states, *Earth-Science reviews*, *93*, 77–84, 2009.

Garcia, K. S., and W. J. Hughes, Finding the lyon-fedder-mobarry magnetpause: A statistical perspective, *JGRA*, *112*, 6229, 2007.

Gonzalez, W. D., and E. Echer, A study on the peak dst and peak negative bz relationship during intense geomagnetic storms, *Geophysical Research Letters*, *32*, L18,103, 2005.

Hakamada, K., and S. I. Akasofu, Simulation of three-dimensional earth solar wind data supplied by nasa's national space science data solar wind disturbance and resulting geomagnetic storms, *Space Science Rev.*, *31*, 3–70, 1982.

Hwang, K.-J., M. L. Goldstein, D. E. Wendel, A. N. Fazakerley, and C. Gurgiolo, Cluster observations near reconnection x lines in earth's magnetotail current sheet, *Journal of Geophysical Research*, *118*, 4199–4209, 2013.

J.B.L. Jones, R. H. R. I. G. T. D. T., R.D. Bentley, Advances in space research, *Space Weather*, *36*, 2005.

Juusola, L., N. Partamies, and E. Tanskanen, Effects of the ring current on preconditioning the magnetosphere for steady magnetospheric convection, *Geophysical Research Letters*, *40*, 1917–1921, 2013.

Kallenrode, M.-B., *Space Physics*, 3 ed., Springer, 2004.

Katzav, J., Should we asses climate model predictions in light of severe tests?, *EOSTr*, *92*, 195, 2011.

Kelley, M. C., *The Earth's Ionosphere*, 2 ed., Elsevuer Inc., 2009.

Kennel, C. F., *Convection and Substorms*, Oxford University Press, 1995.

Kominsky, P., Derivation of conservative mhd equations, 2013.

Krimigis, S. M., D. G. Mitchell, E. C. Roelof, K. C. Hsieh, and D. J. McComas, Imaging the interaction of the heliosphere with the interstellar medium from saturn with cassini, *Science*, *326*, 971–973, 2009.

Kulsrud, R. M., *Plasma Physics for Astrophysics*, Princeton University Press, 2005.

Lanzerotti, L. J., Space weather effects on technologies, *Geophysical Monograph Series*, *125*, 2001.

Lavraud, B., M. F. Thomsen, J. E. Borovsky, M. H. Denton, and T. I. Pulkkinen, Magnetospheric preconditioning under northward imf: Evidence from the study of coronal mass ejection and corotating interaction region geoeffectiveness, *Journal of Geophysical Research*, *111*, 2006.

Lyon, J. G., J. A. Fedder, and C. M. Mobarry, The lyon-fedder-mobarry (lfm) global mhd magnetospheric simulation code, *JASTP*, *66*, 1333–1350, 2004.

MacNeice, P., Validation of community models: 2. development of a baseline using the wang-sheeley-arge model, *SpWea*, *7*, 12,002, 2009a.

MacNeice, P., Validation of community models: Identifying events in space weather model timelines, *SpWea*, *7*, 6004, 2009b.

Maezawa, K., Magnetospheric convection induced by the positive and negative z components of the interplanetary magnetic field: Quantitative analysis using polar cap magnetic records, *Journal of Geophysical Research*, *81*, 2289–2303, 1976.

Mewaldt, R. A., and P. C. Liewer, A small interstellar probe to the heliospheric boundary and interstellar space, *Acta Astronautica*, *35*, 267–276, 1995.

Molteni, F., R. Buizza, T. N. Palmer, and T. Petroliagis, the ecmwf ensemble prediction system: Mothodology and validation, *Quarterly Journal of the Royal Meteorological Society*, *122*, 73–119, 2006.

Mozer, J. B., and W. M. Briggs, Skill in real-time solar wind shock forecasts, *JGRA*, *108*, 1262, 2003.

Odstrcil, D., Modeling 3-d solar wind structure, *Adv. Space Res.*, *32*, 497–506, 2003.

Owens, M. J., C. N. Arge, H. E. Spence, and A. Pembroke, An event-based approach to validating solar wind speed predictions: High-speed enhancements in te wang-sheeley-arge model, *JGRA*, *110*, 12,105, 2005.

Page, R. M., *The Origin of Radar*, Anchor Books, 1962.

Parker, E. N., Dynamics of the interplanetary gas and magnetic fields, *Astrophysical Journal*, *128*, 664, 1958.

Pirjola, R., K. Kauristie, H. Lappalainen, A. Viljanen, and A. Pulkkinen, Space weather risk, *Space Weather*, *3*, 2, 2005.

Priest, E., and T. Forbes, *Magnetic Reconnection*, Cambridge University Press, 2000.

Pulkkinen, A., M. Kuznetsova, A. Ridley, J. Raeder, A. Vapirev, D. Weimer, R. S. Weigel, M. Wiltberger, G. Millward, L. Rastatter, M. Hesse, H. J. Singer, and A. Chulaki, Geospace environment modeling 2008-2009 challenge: Ground magnetic field perturbations, *SpWea*, *9*, 2004, 2011.

Raeder, J., Modeling the magnetosphere for northward interplanetary magnetic field: effects of electrical resistivity, *Journal of Geophysical Research*, *104*, 1999.

Raeder, J., *Global Magnetohydrodynamics - A Tutorial*, Space Plasma Simulation edited by: J. Buchner, C. T. Dum, and M. Scholer, Lecture Notes in Physics 615, 2003.

Runov, A., V. A. Sergeev, R. Nakamura, W. Baumjohann, S. Apatenkov, Y. Asano, T. Takada, M. Volwerk, Z. Voros, T. L. Zhang, J.-A. Sauvaud, H. Reme, and A. Balogh, Local structure of the magnetotail current sheet: 2001 cluster observations, *Annales Geophysicae*, *24*, 247–262, 2006.

Sargent, R. G., Verification and validation of simulation models, *In. Proc. 2004 Winter Simulation Conf.*, 2004.

Sharma, A. S., and T. Veeramani, Extreme events and long-range correlations in space weather, *Nonlinear Processes in Geophysics*, *18*, 719–725, 2011.

Shue, J.-H., P. Song, C. T. Russel, J. T. Steinber, J. K. Chao, G. Zastenker, O. L. Vaisberg, S. Kokubun, H. J. Singer, T. R. Detman, and H. Kawano, magnetopause location under extreme solar wind conditions, *Journal of Geophysical Research*, *103*, 691–700, 1998.

Stone, E. C., A. M. Frandsen, R. A. Mewaldt, E. R. Christian, D. Margolies, J. F. Ormes, and F. Snow, The advanced composition explorer, *SSRv*, *86*, 1–22, 1998.

Taktakishvili, A., M. Kuznetsova, P. MacNeice, M. Hesse, L. Rastatter, A. Pulkkinen, A. Chulaki, and D. Ostrcil, Validation of the coronal mass ejection predictions at the earth orbit estimated by enlil heliosphere cone model, *SpSWea*, *7*, 3004, 2009.

Tatrallyay, M., G. Erdos, Z. Nemeth, M. I. Verigin, and S. Vennerstrom, Multispacecraft observations of the terrestrial bow shock and magnetopause during extreme solar wind disturbances, *Annales Geophysicae*, *30*, 1675–1692, 2012.

Thompson, A. W. P., Evaluating space weather forecasts of geomagnetic activity from a user perspective, *Geophysical Research Letters*, *27*, 4049–4052, 2000.

Volk, H. J., and V. N. Zirakashvili, Cosmic ray acceleration by spiral shocks in the galactic wind, *Astronomy and Astrophysics*, *417*, 807–817, 2004.

Weigel, R. S., Solar wind density influence on geomagnetic storm intensity, *Journal of Geophysical Research*, *115*, 2010.

Xie, H., L. Ofman, and G. Lawrence, Cone model for halo cmes: Application to space weather forecasting, *JGRA*, *109*, 3109, 2004.

Curriculum Vitae

Brian Curtis was born in 1985 in Rochester, New York. He graduated from the State University of New York at Oswego with a Bachelor's degree in Meteorology in 2007. He also received a master's degree in Computational Sciences from George Mason University in Fairfax, Virginia in 2010. He was employed for 7 years as a research assistant under the instruction of Dr. Robert Weigel. His research involves the validation of magnetospheric magnetohydrodynamic space weather models. During his time at George Mason University, he worked on scientific outreach through an annual space weather forecasting contest, was a summer research assistant at the space weather prediction center in Boulder, Colorado in 2009, and in the summer of 2013 was a science collaborator at the National Aeronautics and Space Administration Goddard Space Flight Center in Greenbelt, Maryland.

In addition Brian has attended the:

- Geospace Environment Modeling summer conference in Snowmass, CO in 2009.
- Center for Integrated Space weather Modeling summer school in 2008.
- American Meteorological Society annual conference from 2004 to 2007.